Finite Element Modeling of Articular Cartilage

at different length scales

A DISSERTATION
SUBMITTED TO THE FACULTY OF THE GRADUATE SCHOOL
OF THE UNIVERSITY OF MINNESOTA
BY

Sidharth Saktan Chiravarambath

IN PARTIAL FULFILLMENT OF THE REQUIREMENTS
FOR THE DEGREE OF
Doctor of Philosophy

Perry H. Leo, Jack L. Lewis, Advisors

April 2012

Acknowledgements

This study was carried out during the years 2006 – 2012 in the Department of Aerospace Engineering & Mechanics (AEM), University of Minnesota, Twin Cities. Several people have contributed directly or indirectly to this thesis and I wish to express my deepest gratitude to everyone of them. In particular, I wish to mention the following persons.

First and foremost, I wish to thank my advisors, Professor Jack Lewis and Professor Perry Leo. Professor Lewis has been very supportive throughout my career as a graduate student. His words were always kind and motivating, and his passion and zeal, not only for cartilage research, but also in personal life, are inspiring and exemplary. It has been my privilege to know him and work with him throughout my time at the University of Minnesota. I am thankful to Professor Perry Leo for his encouragement, belief in my abilities and guiding me through till the end. His vast knowledge of composite and solid mechanics helped me understand the subject and create better models for representing cartilage. His patience and kindness is much appreciated by all of the students in the AEM department.

I want to express my sincere gratitude to the Examining Committee who reviewed my thesis: Professors Thomas Shield, Ryan Elliott, Perry Leo and Jack Lewis. I value their inputs and greatly appreciate their time and efforts for their important and constructive criticism.

I would also like to thank Narendra Simha and Ravi Namani for their discussions and insights on the macroscale modeling part. I enjoyed those lively conversations very much and had much to learn from them.

Thanks are also due to Professor Russell Fernandes, Orthopedic Surgery at the University of Washington, Seattle, for his support and arrangements during my stay in Seattle. Our conversations about cartilage research, and also on our common roots were very interesting and provided a spiritual release from thesis work.

Many thanks to all of my friends in the AEM department for all the good times

over many years during our group excursions or during badminton games at the Rec center. I also thank other friends at the University outside AEM, old and new, who have supported and inspired me and touched me by sharing their joys and frustrations. I will cherish these friendships in the years to come.

I thank the Minnesota Supercomputing Insitute and its support staff for all the resources and help in efficiently using these resources. I also thank the AEM department staff for enabling my smooth transition back and for their help with administrative tasks related to degree progress.

I am grateful to my parents, Hemlata and Saktan Chiravarambath, my in-laws, Shilpa and Shirish Khandekar, my brother, Kapil Chiravarambath and sister-in-law, Namrata Grampurohit for their constant motivation and support. I want to especially express my love and gratitude to my beloved wife Gauri Khandekar, who has always motivated me to accomplish my goals and sacrificed much in supporting me and yet has always kept a cheerful, enthusiastic and supporting attitude. Without her support, this thesis would not have been possible. Timely distractions and playful interruptions by my son, Om, are also greatly appreciated.

Finally I thank Neela and Vijay Patwardhan for their role in gaining financial support for my early graduate years. Financial support through the Catherine Mills Davis Grant, through various NIH grants and the AEM department is gratefully acknowledged.

Minneapolis, April 2012

Sidharth Chiravarambath

To my beloved wife, for her endless love and support
. . . and to her beautiful gift, my son

Abstract

The composition and structure of articular cartilage (AC) are inhomogeneous within the tissue and vary throughout its depth. Its extracellular matrix can be considered as a fiber-reinforced composite solid consisting of a dense stable network of collagen fibers embedded in a proteoglycan (PG) gel. Several studies have shown that this specialized structure plays a vital role in the mechanical function of AC. In pathological conditions, such as osteoarthritis (OA), degeneration of cartilage due to changes in mechanical properties is observed. Osteoarthritis is the most common cause of disability in the elderly and affects more than 20 million people in the USA alone. The focus of this work is to understand the mechanical response of AC using finite element models using ABAQUS, a commercial FEA package that is widely used in the field of cartilage mechanics. This is done at two different scales - the macroscale and the mesoscale.

At the macroscale, AC is considered as a homogeneous isotropic poroviscoelastic (PVE) material saturated by the interstitial fluid (water). Indentation tests are performed on cartilage from the mouse tibia plateau using two different sized flat-ended conical indenters with flat-end diameters of 15 μm and 170 μm. A finite element (FE) model of the test is developed and the PVE parameters identified by using inverse methods to minimize the errors between FE simulated and test data. Data from the smaller indenter is first used to fit the viscoelastic (VE) parameters, on the basis that for this tip size the gel diffusion time (approximate time constant of the poroelastic (PE) response) is of the order of 0.1 s, so that the PE response is negligible. These parameters are then used to fit the data from the larger indenter for the PE parameters, using the VE parameters extracted from the data from the smaller indenter.

At the mesoscale the inhomogeneities of AC need to be addressed to understand the microstructural behavior of AC. The problem of interest in this part of the work is to understand the mechanical role of interfibrillar cross-links (IFLs), if they exist, suspected in AC and most collagenous tissues. A 3D FE model of AC meso-structure motivated by the parallel fibril geometry of the mid and deep zones of the patella is developed consisting of a PE matrix, unidirectional, bilinear fibrils (different stiffness in tension and compression), and the IFLs. Parametric studies are then performed for the model in simulated compression tests along the fibril direction and the effect of the IFLs and matrix are predicted and compared. Results suggest presence of IFLs would increase the effective modulus in compression. This is due to maintaining organization of the fibrils into a network due to IFLs imparting stability to the network by preventing early bending of fibrils and effectively reducing the Poisson effect. Finally, with a set of literature based parameters, compression tests for AC using the mesomodel show that removing the cross-links results in a significant (43%) drop in the effective compressive modulus, suggesting resolution necessary to experimentally detect the IFLs. At the mesoscale, the IFLs would play the mechanical role of stabilizing the fibril network and enhancing its stiffness.

Table of Contents

List of Tables

List of Figures

Chapter 1

Overview

1.1 Motivation

Cartilage is a soft, dense connective tissue commonly found at the ends of long bones in humans and other animals. Cartilage is composed of specialized cells called *chondrocytes* that are trapped in an extracellular matrix composed mainly of collagen fibers and a ground substance rich in proteoglycan. Cartilage covering the ends of articulating bones in diarthrodial joints, e.g., knee joint, is called articular cartilage (AC), and it is the focus of this thesis. Articular cartilage has a unique structure and composition [by wet weight: $60-80\%$ water, $10-20\%$ collagen (type II), $4-7\%$ aggrecan, less than 5% other macromolecules] [1] that provide the tissue with remarkable mechanical properties that enable it to perform important biomechanical functions such as mechanical shock absorption, minimizing the mechanical stresses in bone during joint loading and reducing friction between the contacting joint surfaces via a lubrication mechanism [2] under a wide range of loading conditions [1].

In its healthy state, AC is able to withstand large loads, especially in freely movable joints [3–5], throughout normal human lifetime [1]. However, during pathological conditions, such as osteoarthritis (OA), cartilage degeneration and disruption coupled with the changes in the properties of the subchondral bone leads to impaired joint motion and pain [6], often requiring joint replacement. Osteoarthritis, a degenerative joint disease, is the most common form of arthritis that afflicts about 12% of the USA. A study of the mechanical properties of articular cartilage and their variation due to tissue degeneration can provide vital insights in the development of OA. This is the major motivation for studying AC and as a result, mechanical properties of AC have been measured frequently to document OA progression in animal models [7].

1.2 Common Methods for characterizing AC

Various techniques are used to measure and predict the mechanical behavior of AC. The mechanical properties have been measured by mechanical tests such as confined compression, e.g., [8–10], unconfined compression, e.g., [11–13], tension, e.g., [14–16], indentation, e.g., [17–19], etc. that are commonly used for material characterization. Indentation has been a preferred test method for measurement of *in situ* biomechanical properties [19–23], primarily because it is non-destructive, offers high sensitivity and spatial resolution. The small tissue volume needed for indentation makes it advantageous over other methods in *in situ* and *in vivo* measurements.

Many studies have also proposed analytical solutions for stresses and strains in AC and for the contact mechanics in joints to predict its behavior under applied load. Many of these solutions are based on the biphasic theory for AC developed by Mow *et al.* [24]. Chapter 3 is a review of this theory and other biphasic models of AC based on it.

Finite element (FE) models are commonly used for stress analysis of AC and to aid in inferring mechanical properties from experimental testing, e.g., [25–33] among many others. Finite element models are continuum based models, usually based on the biphasic theory (as reviewed in Chapter 3). Finite element models can be developed and analyzed in house or by using commercial packages. Several commercial FE codes are available, but the use of ABAQUS (Dassault Systèmes, Providence, RI, USA) is widespread in FE studies of AC. Wu *et al.* [34] first evaluated the commercial FE software ABAQUS for analyzing biphasic soft tissues. They compared solutions obtained using ABAQUS with those obtained using other finite element models and analytical solutions for three numerical tests: an unconfined indentation test, a test with the contact of a spherical cartilage surface with a rigid plate, and an axi-symmetric joint contact test. They concluded that the biphasic cartilage model can be implemented into ABAQUS to analyze practical joint contact problems with biphasic articular cartilage layers. Consequently, ABAQUS is widely used in FE-based studies of AC, and is the FE code of choice for the work presented in this thesis.

1.3 Present work and organization

The objective of this thesis is to understand the mechanical response of AC using FE modeling in ABAQUS at two different scales - the macroscale and the mesoscale. The material is organized into three parts. In Part I, we take a closer look at the unique structure and composition of AC and its observed mechanical behavior in common test geometries. This is done with an aim of understanding cartilage mechanics which can enable selection of appropriate models for FEA.

Part II deals with the macroscopic study of AC. At the macroscale, AC can be treated as a biphasic material saturated with interstitial fluid (water). We first

review commonly used theoretical models used for continuum modeling of AC. Next, a poroviscoelastic continuum FE model is developed using ABAQUS and used in an inverse FE method coupled with data from nanoindentation testing of mouse AC to extract important mechanical properties of AC. This work presents a novel method to separate the fluid flow-independent and flow-dependent processes in AC in the mouse in indentation testing and to extract the poroviscoelastic parameters in this setting.

In Part III, the mesoscale of AC is studied where the inhomogeneities of AC need to be addressed and modeling of micro-constituents becomes important. The interest in this part of the work is to understand the potential mechanical role of the interfibrillar cross-links thought to be in AC and most collagenous tissues. At this scale, AC can be thought of as a composite material consisting of collagen fibrils free to move about in a thick, viscous, gel-like matrix with the addition of specific interfibrillar cross-links. A 3D mesoscale FE model is developed and studied. Two types of fibril interactions are of interest – those due to the extrafibrillar matrix and those due to specific interfibrillar cross-links. The region of interest is an approximate cube with sides 1 μm. The meso-structure model consists of a poroelastic matrix, unidirectional fibrils and the interfibrillar cross-links. Chapters 6 and 7 discuss the mesomodel in detail.

The material is organized as follows.

- Part I - Introduction to Articular Cartilage
  - Chapter 2: In this chapter, the structure and composition of AC and its mechanical behavior is described in brief.
- Part II - Macroscopic Modeling

  - Chapter 3: Chapter 3 and 4 pertain to the macroscopic scale. Chapter 3 is a review of some of the theoretical models developed for the mechanical response of AC at the continuum level.
  - Chapter 4: In this chapter, the FE model developed for the macroscopic scale using ABAQUS is described. The indentation experiments carried out on mouse cartilage and the numerical implementation of inverse FE is also discussed.

- Part III - Mesoscale Modeling
  - Chapter 5: Chapter 5, 6 and 7 denote the part of this work that pertains to mesoscale AC mechanics. Chapter 5 is a review of some of the important fibril reinforced FE models of AC in literature.
  - Chapter 6: In this chapter, the development of the fibril reinforced mesoscale FE model with interfibrillar cross-links is discussed in detail.
  - Chapter 7: This chapter is an extensive parametric study of the meso-model. Several important parameters in the model are studied and the mechanical effect of the interfibrillar cross-links is discussed.

- Part IV: This part is a brief summary of the primary contributions and concludes the thesis.

Part I

Introduction to Articular Cartilage

Chapter 2

Articular Cartilage - Structure, Function and Composition

This chapter provides a brief introduction to the structure and composition of articular cartilage (AC). We shall also discuss some of the observed mechanical behavior of AC under common loading conditions.

Cartilage is a soft, dense connective tissue. Like most connective tissue, cartilage is composed of cells and an extracellular matrix composed mainly of fibers and extrafibrillar matrix. The cells that form cartilage are specialized cells called chondrocytes. The fibers are mostly collagen and are embedded throughout the tissue. The 'solid' phase of cartilage, including fibers, is typically called the extracellular matrix (ECM). The fibers of cartilage form an extensive network within the tissue. Often, the fibrillar network is treated separately and the remaining matrix referred to as the extrafibrillar matrix (EFM). There are no nerves or blood vessels in cartilage, thus when damaged, it does not heal readily. Nutrients are diffused through the ECM.

There are three major types of cartilage found in the body: hyaline cartilage, elastic cartilage and fibrocartilage. These different types of cartilages are distinguished by their structure, elasticity and strength. The biochemical composition and molecular structure of the ECM imparts distinct biomechanical properties to these different types of cartilage depending upon their location in the body and properties required for their function. Hyaline cartilage is smooth, semi-transparent and appears bluish-white in color. It consists of chondrocytes situated far apart in fluid-filled spaces called lacunae and there is an extensive amount of ECM between the cells with a number of collagenous fibers. The most common type of hyaline cartilage is articular cartilage which covers the articulating joint surfaces of long bones and sesamoid bones within synovial joints. Hyaline cartilage is also found in the nasal septum, the sternal end of the rib, and the trachea. Elastic cartilage is similar to hyaline cartilage, but in addition to the collagenous fibers, the ECM is distinguished by the presence of branched elastic fibers, which make this cartilage more flexible than hyaline cartilage. Elastic cartilage is seen in the external ear, in parts of the larynx and the epiglottis. Fibrocartilage has a rough and fibrous appearance owing to thick layers of larger collagen fibers in the ECM. Fibrocartilage is commonly seen between the inter-vertebral discs and the meniscus of the knee.

2.1 Articular Cartilage (AC)

AC is a resilient, load-bearing tissue that forms the articulating surfaces of diarthrodial joints, such as the knee joint and the hip joint. It is the most common form of hyaline cartilage. It is vital for maintaining a normal joint motion due to its remarkable mechanical properties. It provides the articulating surfaces with low friction and wear characteristics required for repetitive gliding motion. AC in freely movable joints can withstand very large loads [3–5]. It also absorbs mechanical shocks to the

joint and helps spread the applied load evenly onto the subchondral bone.

In young individuals, AC in its healthy state appears smooth, glossy and intact. In older individuals and in cases where there is tissue damage due to trauma or pre-clinical diseases states, AC loses this look and appears dull and fibrillated. The major motivation for studying AC and measuring its mechanical properties is injury and disease, particularly the degenerative joint disease osteoarthritis (OA). OA is the most common form of arthritis and the most common cause of disability in the elderly. An estimated 12.1 % of the U.S. population (about 21 million) is affected by OA; 85% of all people will have some degree of OA in one or more joints by the age of 55–65. It is characterized by pain and disability and severe OA often leads to replacement of the joint. In OA, a progressive degeneration of AC is observed along with other indications such as lacerations, fibrillation, formation of deep fissures etc. In advanced OA, AC is often entirely lost at the weight bearing joints [35–37]. Studies of mechanical properties of AC and its variations can provide vital insights and aid in understanding of the development of OA. In the following sections, the microstructure of AC along with its biochemical composition is described, and these aspects of the tissue are related to its mechanical properties.

2.2 AC Structure and Composition

AC can be considered as a multiphasic material with two major phases: a solid phase saturated with a fluid phase. The solid phase consists of chondrocytes, different types of collagen molecules, the negatively charged proteoglycans (PGs) and other proteins in smaller quantities, such as hyaluronan, link protein, biglycan, decorin, fibromodulin, perlican, fibronectin, etc., these components form the ECM [2]. The fluid phase is composed of water and electrolytes. A schematic showing several different components and their hypothesized interactions in AC is shown in Fig. 2.1.

Composition of AC is primarily determined by the ECM because the chondrocytes occupy only a small proportion of the total volume of the tissue. The material properties of AC are dependent on the properties of the ECM. Table 2.1 [2] lists the currently understood components of AC. Although many molecules are not major components in terms of absolute mass of the ECM, they may be present in similar molar amounts as collagen and aggrecan and may serve important biological regulating and/or structural functions.

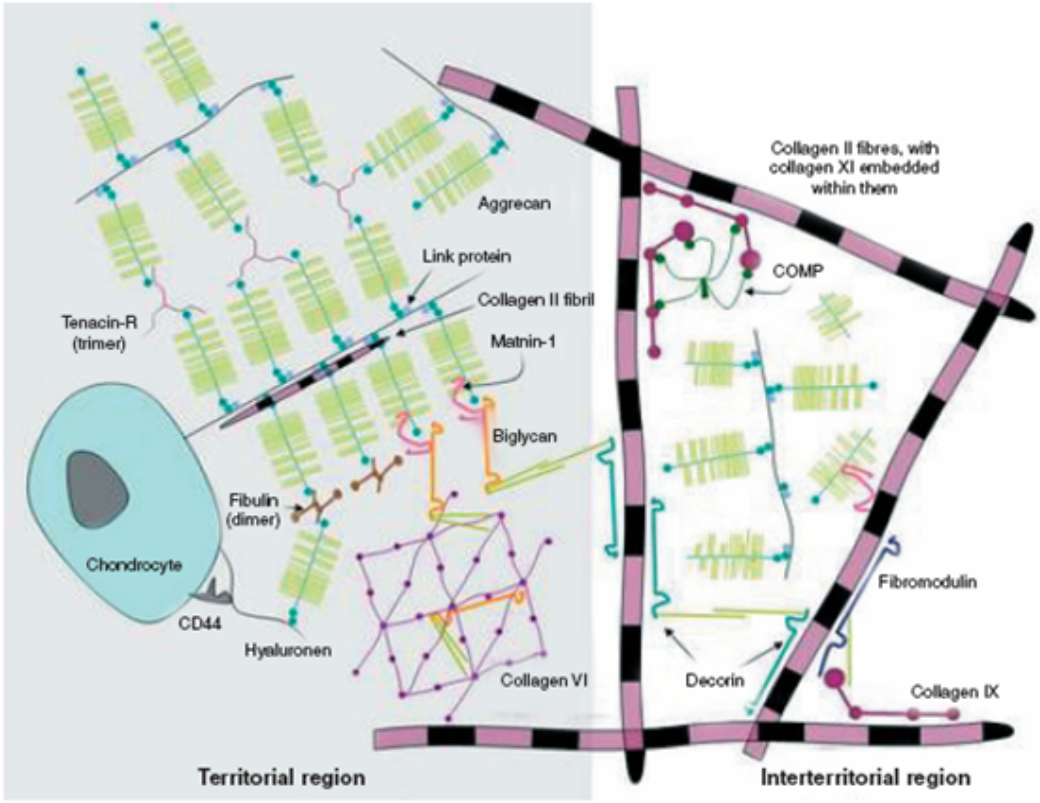

Figure 2.1: A schematic showing several components in articular cartilage from Dudhia (2005) [38] (with permission).

Table 2.1: A Summary of the Components of Articular Cartilage

Component	**Wet Weight**
Quantitatively Major Components	
Water	60–85%
Collagen type II	15–22%
Aggrecan	4–7%
Quantitatively Minor Components (less than 5%)	
Link protein	
Hyaluronan	
Collagen type I	
Collagen type V	
Collagen type VI	
Collagen type IX	
Collagen type XI	
Decorin	
Biglycan	
Fibromodulin	
Perlican	
Thrombospondin	
COMP/TSPS	

2.2.1 Zonal variations in AC

The cell shape and volume, collagen fibril diameter and orientation, PG concentration, and water content of articular cartilage vary throughout its depth, from the articular surface to the subchondral bone. AC can be divided into the following four different layers or zones (as shown in Fig. 2.2):

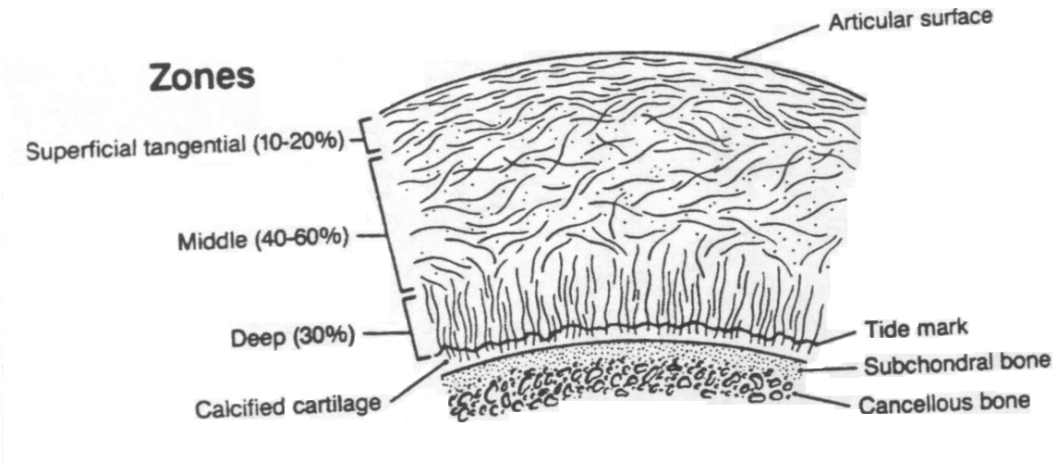

Figure 2.2: Schematic structure of articular cartilage showing zonal variations along the depth, from the articular surface to the subchondral bone (from *Basic Orthopedic Biomechanics* [2]).

Superficial zone

This is the uppermost and the thinnest ($\approx 10-20\%$) zone which forms the gliding surface of the joint [35]. In this zone collagen and water content are highest [39]. PG content is at its lowest level [35] and PGs and collagen appear to be strongly interconnected in this zone, which may assist in resisting shear stresses produced by gliding motion [6]. The collagen fibers are thin and densely packed with the long axis parallel to the articular surface. The chondrocytes appear flattened and are relatively inactive [40]. The aggrecan content is lower in the superficial zone compared to the deeper zones with smaller cell volume and higher cell density [40].

Transitional zone

The transitional zone is about 40–60% of the total AC volume. The chondrocytes have a more rounded appearance and are larger and more active than in the superficial zone [35]. The collagen fibres are larger in diameter and frequently have a more random orientation, although this varies with specific joint. The aggrecan aggregates and PG content are higher in this zone than the superficial zone.

Deep zone

The deep zone has collagen fibres with largest diameters that are organized perpendicular to the joint surface. The chondrocytes are spherical and often arranged in a columnar fashion [35] and their synthetic activity is highest [40, 41]. This zone has the highest concentration of PGs and lowest water content.

Zone of calcified cartilage

This zone separates the cartilage from the subchondral bone and acts as a transition layer between bone and cartilage. Histological staining with hematoxylin and eosin shows a wavy bluish line, called the tide mark, which separates the deep zone from the calcified zone. It is characterized by small cells distributed in a cartilagenous matrix encrusted with crystals of calcium salts and has a low PG content. The collagen fibers from the deep zone, oriented perpendicular to the subchondral bone, cross the tide mark and insert into the calcified zone. This provides a strong anchoring system for the tissue on the subchondral bone [42,43]. Although this zone is calcified to the same extent as the bone, it is less stiff than bone, but, about 10–100 times stiffer than cartilage in compression [44]. Both the tide mark and the junction between the calcified cartilage and subchondral bone are wavy and provide great resistance to shear stresses.

2.2.2 Chondrocytes

Chondrocytes are metabolically active cells responsible for the synthesis and maintenance of articular cartilage. These cells increase the volume of the ECM during skeletal growth and in the mature tissue they are responsible for the maintenance of the ECM [35]. They receive nutrition from the synovial fluid by diffusion and/or convection through the matrix [45, 46]. Chondrocytes respond to a number of environmental stimuli which can influence their synthetic response. These stimuli include physical factors such as stresses, strains, hydrostatic pressure changes, electric current and potentials, etc., and chemical factors such as growth factors, soluble mediators, interleukins, matrix molecules etc. [35].

2.2.3 Water

Water is the most abundant component of normal articular cartilage, making up from 60–85% of the wet weight of the tissue. A small percentage of this water is contained in the intracellular space, about 30% resides within the intrafibrillar space of collagen, and the remainder is contained in the molecular pore space of the ECM. For normal cartilage, it is believed that the proportion of water in the intrafibrillar space appears not to vary with age [47]. Inorganic salts, such as sodium, calcium, chloride and potassium are dissolved in the tissue water. Water content varies throughout cartilage. The amount of water present depends upon several factors [2]: (a) the concentration of the PGs, i.e., fixed charge density (FCD) and the resultant swelling pressure exerted by the negative charge groups on the PGs and the ions dissolved in the interstitial fluid - the Donnan osmotic pressure; (b) the organization of the collagen network; and (c) the strength and stiffness of this network, which surrounds the PG molecules and resists the swelling pressures. During early OA, water content increases significantly which greatly affects the mechanical properties of the tissue.

Most of the water can be extruded from the tissue by applying a pressure gradient across the tissue, or by compressing the solid matrix. There is a very high frictional resistance against this flow through the molecular size pores of the ECM, and thus the permeability of the tissue is low [24]. This frictional resistance and the pressurization of the water within the ECM are the basic mechanisms by which AC derives its ability to support very high joint loads. The frictional drag force is also an important component of the viscoelastic behaviour of AC during mechanical loading.

2.2.4 PGs

PGs are large, complex biomolecules each composed of a central core protein and one or more negatively charged glycosaminoglycan (GAG) chains covalently attached [39]. PGs form about 30–35% of the dry weight of the tissue [35]. PGs are a very diverse class of molecules. In the case of cartilage, a major component of the ECM is the large aggregating PG, aggrecan, which imparts mechanical properties to cartilage to withstand compressive stresses due to joint loading. Loss of aggrecan, or its degradation, results in a loss of compressive stiffness of cartilage.

There are many different types of GAGs as well, however, three major types have been found in cartilage PGs: (1) chondroitin 4/6 sulfate; (2) keratan sulfate; and (3) dermatan sulfate. The chondroitin sulfates are the most prevalent GAGs in AC, accounting for 55% –90% of the total population, depending upon age or presence of OA [35]. All the GAG chains found in AC have repeating carboxyl (COOH) and/or sulfate (SO_4) groups that ionize in solution (COO^- and $SO_3{}^-$)and require positive counterions such as Ca^{2+} and Na^+ to maintain overall electronuetrality. Because the PGs are closely packed together in the tissue, this gives rise to a high negative charge density, quantified as the FCD [39]. Due to the FCD, the cation

concentration inside the tissue is higher than in the surrounding synovial fluid, which causes a pressure differential that results in swelling of the tissue.

2.2.5 Collagens

Collagens are a family of the most abundant proteins in humans and are the major structural molecules of the ECM. They play a critical role in maintaining the structural integrity of various tissues. There are at least 20 different collagen types identified to date with at least 38 genetically different polypeptide chains [2]. In AC, collagens form more than 50% of the dry weight of the tissue [6, 35]. Type II collagen, which represents 90–95% of the total, is the major AC collagen with smaller amounts of types V, VI, IX, X, and XI collagens [48, 49]. Collagen molecules are rod-shaped with a high degree of structural organization. Some types of collagen (e.g., type I, II) assemble to form small fibrils and larger fibers with dimensions that vary through the depth of the cartilage layer [50]. The exquisite architectural arrangement of the collagen structure appears to have been specifically designed to resist tension, but does not offer significant resistance to pressures [2, 51], thus, providing resistance against swelling and tensile strains.

Molecular Cross-Links

There are a large number of minor molecules in the ECM that comprise less than 5% of the dry weight. These include decorin, cartilage-olegometric-matrix-protein (COMP), fibromodulin, biglycan, matrilins 1 and 3, and others (Table 2.1). Some of these are known to be regulatory molecules, but all have been shown to bind to collagen or other matrix molecules non-covalently. For all of them, it has been speculated that they form cross-links between collagen fibrils and effectively reinforce the collagen network. However, this speculation has not been verified and remains one of the major unknowns in cartilage science. It has been hypothesized that

such cross-links or 'glue' molecules exist and that damage to this 'glue' is one of the mechanisms in the OA disease process. Several studies have proposed such molecules and indentified specific binding mechanisms, e.g., type IX collagen by Eyre *et al.* [52, 53], matrilin-3 by Budde *et al.* [54], etc. Eyre [55] suggested from biochemical evidence that type IX collagen may form a covalent bridge between fibrils, increasing network mechanical integrity and providing a restraint for entrapped PG osmotic swelling pressure. Recently, Parsons *et al.* [56] were able to confirm an interaction between type IX collagen and fibronectin that formed an important molecular bridge in AC that could contribute to the matrix integrity of the tissue.

2.3 Mechanical Behavior

The structure and composition of AC varies through the depth of the tissue. As a result, the mechanical properties of AC are anisotropic and non-homogeneous. The collagen network plays a vital role in the mechanical inhomogeneity and anisotropy of AC. The fibrils resist load only in tension and their orientation changes over the height of the tissue. In the superficial zone, they are arranged parallel to the articular surface, giving this layer a high tensile stiffness in the direction parallel to the surface and very low stiffness perpendicular to the surface. The surface fibrils, therefore contribute to the mechanical resistance against surface shear forces. In contrast, the fibrils in the deep zone are oriented perpendicular to the articular surface, thus, providing great resistance against swelling.

From a material point of view, the ECM of cartilage can be seen as a fiber-reinforced composite solid consisting of a dense, stable network of collagen fibres embedded in a viscoelastic gel composed of PG and the minor molecules. Thus, from a mechanical point of view, the most relevant components of AC are the highly organized network of collagen fibers with the intrafibrillar matrix. In this section,

the relation between the composition, structure and the mechanical properties of the tissue are discussed.

2.3.1 Tensile behavior

When cartilage is tested in tension, the collagen fibres and the linked PG molecules get aligned and stretched along the axis of loading. Therefore, the tensile modulus of AC depends on the collagen fibril density, orientation and the amount of cross-linking between the molecules [57]. A non-linear toe region is seen in the stress-strain curve for small deformations, when the tensile stress in the specimen is relatively small, as the collagen fibrils realign rather than stretch. For larger deformations, when the realignment is mostly complete and collagen fibrils are stretched, a larger tensile force is generated due to the increased stiffness contributed by the collagen fibrils. Thus, the tensile stiffness of AC is highly strain-dependent. The PGs also affect the tensile stiffness of AC by generating swelling pressures and prestressing AC.

2.3.2 Compression behavior

When AC is loaded in compression, there is fluid movement within the tissue which results in volumetric changes. Because of these volumetric changes, the FCD in the tissue increases which in turn increases the osmotic pressure. Hence, as the volume of the tissue decreases in compression, the effective stiffness increases. The PGs are mainly responsible for the mechanical behavior shown by AC in compression [58]. The collagen fibril network also contributes to the compressive stiffness of AC by keeping the swelling pressures high in the tissue by preventing swelling.

2.3.3 Time dependent behavior

AC shows highly time dependent behavior. Two distinct mechanisms are responsible for this behavior: (1) the flow-dependent mechanism (poroelasticity), i.e., the frictional drag force as the interstitial fluid flows through the porous solid matrix; and (2) the flow-independent mechanism (viscoelasticity), i.e., the intrinsic time-dependent deformability of the solid matrix. Studies show that both the collagen fibers as well as the PG gel in which they are embedded have flow-independent viscoelasticity [58–60].

Under load, fluid is exuded from the tissue and the volume of the tissue decreases. The movement of the interstitial fluid is governed by the hydraulic permeability of the solid matrix. It is very difficult for the interstitial fluid to escape from the tissue due to the relatively low permeability of the solid matrix [2]. As the fluid flow slows down and eventually stops, i.e., at equilibrium, the entire load is increasingly carried by the solid matrix and the internal swelling pressures generated by the FCD of the PGs. As the load is removed, AC recovers to its initial configuration, due to the elasticity of the solid matrix and also due to the increased osmotic pressure within the tissue due to the removal of the load.

2.3.4 Shear behavior

Under pure shear, and for small strains, the tissue samples do not undergo any volumetric changes (ideally). As a result, no significant pressure gradient or fluid flow should occur through the matrix [58,61,62]. The collagen fibrils mainly account for the shear stiffness shown by the ECM [58]. Through the swelling mechanism, the PGs indirectly contribute to the overall stiffness of the ECM in shear.

It is evident that AC has a complex structure with several components that makes it inhomogeneous and induces depth-dependent and strain-dependent mechanical properties within the tissue [9, 15, 31, 63, 64]. Many of these mechanical properties change markedly at the onset of OA due to disruption of the collagen network, depletion of PGs and increased water content. These changes in structure and composition lead to softening and progressive loss of AC.

The traditional method for identifying which molecules in the matrix determine the cartilage mechanical properties, the structural molecules, has been to test the tissue mechanical property, digest the tissue with an enzyme specific to the molecule in question, and then retest the tissue. A change in properties would indicate that the molecule in question is a structural molecule. Thus, use of collagenases has demonstrated the structural role of collagen. However, there are few enzymes specific to the matrix molecules of interest. Thus, the mechanical role of the minor molecules is unknown.

Part II

Macroscale Modeling of AC

Chapter 3

Theoretical Models for Articular Cartilage behavior

In order to extract mechanical properties of articular cartilage (AC) from experimental indentation data, one needs to adopt a material model and test geometry for AC. There is a long history of cartilage testing and development of consistent continuum models for data reduction. The biphasic models of Mow and coworkers have long been prominent in the field, e.g., [8, 20, 24, 65, 66] . Various other researchers have built upon these models and have been successful in fitting cartilage experimental data [11, 30, 32, 67–74]. This chapter provides a brief overview of the linear biphasic model for (AC) behavior and extensions of this model which include other important features observed in cartilage structure and behavior. A review of computational models for AC by Wilson *et al.* [32] was used as a guidance for the material presented here.

3.1 The Biphasic Model

The biphasic theory for AC, also referred to as the KLM theory, was first proposed by Kuei, Lai, Mow and Armstrong [24]. This theory assumes the tissue to be a homogeneous binary mixture of an incompressible, isotropic, linearly elastic solid and an incompressible, inviscid fluid. These two phases are non-dissipative and the only dissipation comes from the frictional drag of relative motion between the phases. The total stress in the tissue is given by the sum of the solid and fluid stress [8],

$$\boldsymbol{\sigma}^t = \boldsymbol{\sigma}^s + \boldsymbol{\sigma}^f \tag{3.1}$$

where $\boldsymbol{\sigma}^s$ and $\boldsymbol{\sigma}^f$ are the stress in the solid matrix and the interstitial fluid stress respectively. In most biphasic models, the solid matrix is assumed to be linear elastic and isotropic. For linear isotropic elasticity, the stress-strain relation for the solid matrix is

$$\boldsymbol{\sigma}^s = -\alpha p\boldsymbol{I} + \lambda_s e\boldsymbol{I} + 2\mu_s\boldsymbol{\varepsilon} \tag{3.2}$$

where α is the ratio of the solid volume to the fluid volume in the matrix, λ_s and μ_s are the Lamé constants of the elastic solid matrix, e and $\boldsymbol{\varepsilon}$ are the dilatation and the strain tensor of the solid matrix, respectively, and $\boldsymbol{I}$ is the identity tensor. The interstitial fluid stress is

$$\boldsymbol{\sigma}^f = -p\boldsymbol{I} \tag{3.3}$$

Note that if the pressure in the interstitial fluid is zero, for example at equilibrium, then only the linear elastic behavior of the solid matrix is observed.

From the assumption of incompressibility for both the solid phase and the fluid phase, it follows that the solid matrix can only be squeezed into a given spatial control volume if an equal and opposite amount of fluid is squeezed out. This constraint leads to a continuum mixture continuity equation for homogeneous materials given

by

$$\nabla \cdot \vec{v}^f + \alpha \nabla \cdot \vec{v}^s = 0 \tag{3.4}$$

where $\vec{v}^s$ and $\vec{v}^f$ are the solid and fluid velocities, respectively, and $\nabla\cdot$ is the divergence operator. According to Darcy's law the fluid flux is related to the hydrostatic fluid pressure, as

$$\frac{1}{\alpha}(\vec{v}^s - \vec{v}^f) = -k\nabla p \tag{3.5}$$

The left hand side term represents the fluid flow through the surface of the mixture, k is the hydraulic permeability and ∇ is the gradient operator. Thus, the continuity equation becomes

$$\nabla \cdot \vec{v}^s + \nabla \cdot (k\nabla p) = 0 \tag{3.6}$$

This isotropic biphasic model has been used in various studies to analyze confined compression [11, 12, 66], unconfined compression [8, 11, 12], indentation [20, 65], etc. for normal as well as OA cartilage. The material properties of AC are depth-dependent. This depth dependency is included in several biphasic models by using a depth-dependent aggregate modulus or permeability.

The linear biphasic model does include the flow-dependent viscoelasticity of AC (permeability), however important features like strain-dependent permeability, anisotropy due to the collagen network, viscoelasticity of the solid matrix (flow-independent viscoelasticity) and swelling behavior are not included. In the following sections extensions of the linear biphasic model that include one or more of these mechanisms are discussed.

3.2 Strain-dependent permeability

The permeability of AC is dependent on the FCD of the PGs and the pore sizes in the extracellular matrix. When the tissue is deformed, both the FCD and the pore

sizes change, making the permeability of AC strain-dependent. Lai et al. [63] have shown that the strain-dependent permeability can be described by the relation

$$k = k_0 \exp(M e_s) \tag{3.7}$$

where k_0 and M are material constants and e_s is the dilatation of the solid matrix. This can be written in terms of the current void ratio, e (the ratio of the fluid and solid fractions), as

$$k = k_0 \left(\frac{1+e}{1+e_0} \right)^M \tag{3.8}$$

where e_0 is the initial void ratio.

3.3 Swelling

Swelling of cartilage is caused due to two different mechanisms: (1) osmotic swelling, which is due to an excess in ion particles inside the tissue, and (2) chemical expansion, due to repulsion of the closely spaced negatively charged groups of the proteoglycans. A brief description of how these mechanisms are included in different numerical models follows next.

3.3.1 Osmotic swelling

Mechano-electrochemical model

Several mechano-electrochemical models have been developed which include the influence of ion concentration and ion fluxes, and enable a representation of articular cartilage swelling behavior. The triphasic model by Lai *et al.* [75] and quadriphasic model by Huyghe and Janssen [76] included a third monovalent ionic phase for small deformations and generalized for finite deformations, respectively. The total stress is the same as for the biphasic model, but in this case the hydrostatic pressure is

given by

$$p = \mu^f + \Delta\pi \tag{3.9}$$

where μ^f is the electrochemical potential and $\Delta\pi$ the osmotic pressure gradient using the concentrations of mobile ions.

Biphasic swelling model

Wilson *et al.* [77] developed a biphasic swelling model which is a simplification of the full mechano-electrochemical model [75,76] assuming that the ion concentration is always in equilibrium. Only the ion concentrations at equilibrium need to be determined as the osmotic components are assumed to equilibrate instantaneously with the external bath. The fixed charge density (FCD) is expressed as a function of the tissue deformation, the initial FCD and the initial fluid fraction.

3.3.2 Chemical expansion

The additional stress due chemical expansion, T_c, has been proposed of different forms [75,78] by different groups. The simplest form, as proposed by Eisenberg and Grodzinsky [78] is given by

$$T_c = \beta_0 \exp\left(\frac{c}{c_\beta}\right) \tag{3.10}$$

where β_0 and c_β are material constants, and c is the effective NaCl concentration.

3.4 Anisotropy

AC has a complex collagen network and several other components, making it highly anisotropic. It also has different properties in tension and compression. Several models that include the anisotropy of AC in different ways can be seen in the literature. In this section, the important and widely used anisotropic models of AC

are reviewed.

3.4.1 Models with Transverse Isotropy

A transversely isotropic biphasic model (TIBPE) for AC assumes that all fibrils run in the same direction. Hence, AC can be seen as an orthotropic material with one plane of isotropy. The directions in the plane of the fibrils are the longitudinal direction, parallel to the fibrils, and the transverse direction, perpendicular to the fibrils. The stresses in the solid are given by [32]:

$$\begin{bmatrix} \sigma_{11} \\ \sigma_{22} \\ \sigma_{33} \\ \sigma_{12} \\ \sigma_{13} \\ \sigma_{23} \end{bmatrix} = \begin{bmatrix} \frac{1}{E_T} & -\frac{\nu_{TT}}{E_T} & -\frac{\nu_{LT}}{E_L} & 0 & 0 & 0 \\ -\frac{\nu_{TT}}{E_T} & \frac{1}{E_T} & -\frac{\nu_{LT}}{E_L} & 0 & 0 & 0 \\ -\frac{\nu_{TL}}{E_T} & -\frac{\nu_{TL}}{E_T} & \frac{1}{E_L} & 0 & 0 & 0 \\ 0 & 0 & 0 & \frac{1}{G_L} & 0 & 0 \\ 0 & 0 & 0 & 0 & \frac{1}{G_L} & 0 \\ 0 & 0 & 0 & 0 & 0 & \frac{1}{G_T} \end{bmatrix} \begin{bmatrix} \varepsilon_{11} \\ \varepsilon_{22} \\ \varepsilon_{33} \\ \varepsilon_{12} \\ \varepsilon_{13} \\ \varepsilon_{23} \end{bmatrix} \tag{3.11}$$

where E_L and E_T are the longitudinal and the transverse Young's moduli respectively, G_L is the longitudinal shear modulus, and ν_{LT}, ν_{TT} and ν_{TL} are the Poisson's ratios that give the strain in either the longitudinal or the transverse directions for a stretch in the other direction. The transverse shear modulus G_T is given by

$$G_T = \frac{E_T}{2(1+\nu_{TT})} \tag{3.12}$$

Due to the symmetry, note that

$$\frac{\nu_{LT}}{E_L} = \frac{\nu_{TL}}{E_T} \tag{3.13}$$

Thus, there are five independent material parameters, viz., E_L, E_T, ν_{LT}, ν_{TT} and G_L, in addition to the permeability, k.

Such transversely isotropic models were used in various studies. Cohen *et al.* [68] advanced the biphasic model for soft tissues by using a linear transversely isotropic solid phase to explain observed stress relaxation in unconfined compression. Bursać *et al.* [11] investigated the ability of the transversely isotropic model to describe confined and unconfined (compression) stress relaxation behavior of calf cartilage.

3.4.2 Conewise linear elasticity model

Material properties of AC measured from various joints of different species have indicated that the stiffness of cartilage in compression may be one to two orders of magnitude smaller than in tension. This is referred to as the "tension-compression nonlinearity" in cartilage literature. Soltz et al. [72] have proposed a biphasic model employing the continuum-based Conewise Linear Elasticity (CLE) model of Curnier et al. [79] with cubic symmetry to describe the solid phase of the biphasic mixture that can account for this observed tension-compression nonlinearity, while still being linear. In this model, the elastic stress of the biphasic mixture reduces to

$$\boldsymbol{\sigma}^e(\boldsymbol{\varepsilon}) = \lambda_{aa}[\boldsymbol{A}_a : \boldsymbol{\varepsilon}]\mathrm{tr}(\boldsymbol{A}_a\boldsymbol{\varepsilon})\boldsymbol{A}_a + \lambda_{ab}\mathrm{tr}(\boldsymbol{A}_a\boldsymbol{\varepsilon})\boldsymbol{A}_b + \mu_a(\boldsymbol{A}_a\boldsymbol{\varepsilon} + \boldsymbol{\varepsilon}\boldsymbol{A}_a) \tag{3.14}$$

with summations implicit over a and b (a,b = 1,3; $b \neq a$), and $\lambda_{ab} = \lambda_{ba}$ with no sum on λ_{aa}. $\boldsymbol{\varepsilon}$ is the infinitesimal strain tensor and $\boldsymbol{A}_a$ is a texture tensor corresponding to each of the three preferred material directions defined by the unit vector $\boldsymbol{a}_a$ ($\boldsymbol{a}_a \cdot \boldsymbol{a}_a = 1$, no sum), with $\boldsymbol{A}_a = \boldsymbol{a}_a \otimes \boldsymbol{a}_a$ ($\otimes$ denoting the dyadic or outer product of vectors that results in a tensor of order two and rank one). For orthotropic material symmetry, $\boldsymbol{a}_a \cdot \boldsymbol{a}_b = 0$ when $b \neq a$, and the three planes of material symmetry are defined by their unit normal vectors $\boldsymbol{a}_a$. The tension-compression nonlinearity

occurs when the Lamé constant λ_{aa} (no sum) is dependent on the component of normal strain, $\boldsymbol{A}_a : \boldsymbol{\varepsilon}$, along the preferred direction $\boldsymbol{a}_a$:

$$\lambda_{aa}[\boldsymbol{A}_a : \boldsymbol{\varepsilon}] = \begin{cases} \lambda_{-aa}, & \boldsymbol{A}_a : \boldsymbol{\varepsilon} < 0 \\ \lambda_{+aa}, & \boldsymbol{A}_a : \boldsymbol{\varepsilon} > 0 \end{cases} \qquad \text{(no sum)} \tag{3.15}$$

There are eight material properties for this model: λ_{-aa}, λ_{+aa} and μ_a $(a, b = 1, 3;$ $b \neq a$, no sum). Experimental validation of this model would require testing of cartilage samples in tension, compression, and shear with respect to all three planes of symmetry; however due to size limitations on the specimen it is challenging to test articular cartilage in tension along the direction perpendicular to the surface ($\mathbf{a}_3$), in compression parallel and perpendicular to the split lines ($\mathbf{a}_1, \mathbf{a}_2$), or in torsional shear about $\mathbf{a}_1$ and $\mathbf{a}_2$. Therefore, a cubic symmetry is assumed for this model which reduces the number of elastic material constants to four.

In summary, the CLE model has five material parameters: the aggregate modulus in compression and tension, $H_{-A} = \lambda_{-1} + 2\mu$ and $H_{+A} = \lambda_{+1} + 2\mu$ respectively, "off-diagonal" modulus, λ_2, determined from confined compression as a ratio of radial stress to axial strain at equilibrium, shear moduli μ and permeability k. This model was used to analyze both confined and unconfined compression, torsional shear tests and tensile tests for articular cartilage [72, 73].

3.4.3 Fibril-reinforced models

The tension-compression nonlinearity of the solid matrix can also be included by using a fibril-reinforced model. In such models, in addition to the isotropic matrix, the collagen fibril network contributes to the stiffness of the material. So, the solid stress of a fibril-reinforced model is given by the sum of the EFM and the fibril stresses. Chapter 5 gives a review of some of the prevalent fibril-reinforced models used for AC.

There are two types of fibril-reinforced models seen in the literature, spring models and continuum models. In the spring models, springs are placed between the nodes of the elements to represent the fibrils. This means that fibrils can be represented only in the direction of the elements. The solid stress of the fibril-reinforced material is given by the sum of the matrix and fibril stresses [80], as

$$\boldsymbol{\sigma}_E = \boldsymbol{\sigma}_m + \boldsymbol{\sigma}_f \tag{3.16}$$

where σ_m and σ_f are the stresses in the nonfibrillar matrix and the collagen fibrils, respectively. Li *et al.* [81–83] further developed the model by Soulhat *et al.* to include nonlinear features.

In the continuum fibril reinforced models, the fibril orientation is independent of the finite element mesh. This enables a representation of a geometrically realistic network as fibrils can run in any direction. Several continuum models exist [84–89] which relate the macroscopic properties to the tissue microstructure. These models differ in theoretical formulation, homogenization procedure, constitutive laws, etc.

The micro-structural model by Schwartz *et al.* [86] is not based on the biphasic theory. Instead the an idealized model of AC is treated as a fiber-reinforced composite. In the models of Wilson *et al.* [87, 90, 91] the collagen fibril orientation was independent of the mesh, enabling representation of a geometrically realistic collagen network.

$$\boldsymbol{\sigma}_E = \boldsymbol{\sigma}_m + \sum_{i=1}^{\text{tot}\, f} \sigma_{f,i} \vec{v}_{new,i} \otimes \vec{v}_{new,i} \tag{3.17}$$

where $\sigma_{f,i}$ are fibril stresses in the ith fibril and $\vec{v}_{new,i}$ the current fibril direction of the ith fibril, and the sum is $\boldsymbol{\sigma}_f$.

Federico *et al.* [88] used a homogenization procedure for transversely isotropic composites with inclusions [92], and derived a transversely isotropic transversely homogeneous (TITH) model in which every possible fiber direction was taken into account, and that incorporated the continuous variation of the elastic modulus of cartilage as a function of depth.

Garcia *et al.* [89] proposed a biphasic viscohyperelastic fiber-reinforced model for articular cartilage. Articular cartilage was considered as a biphasic material with its solid component formed of two phases. Both solid phases were represented by the viscohyperelastic law described by Garcia and Cortés (2006) [74], but they differed in the hyperelastic function used. The fibers were assumed to resist only in tension.

In the spring-based fibril-reinforced models, the fibrils resist only in tension. The transversely isotropic biphasic model (discussed in 3.4.1) has the same stiffness in compression and tension. Thus, a more accurate representation of the fibril behavior can be used in fibril-reinforced models. Also, introduction of fibers allows inclusion of nonlinear properties of fibers as well as more realistic orientations of fibers. The spring-based models have been used to characterize the role of the collagen network in cartilage time-dependent response. The continuum fibril-reinforced models have been successfully used to describe cartilage response in confined and unconfined compression and indentation.

3.5 Poroviscoelastic models (non-fibril-reinforced)

As discussed before, the transient behavior of articular cartilage is caused by both fluid-flow-dependent and flow-independent viscoelasticity. A biphasic poroviscoelastic model (BPVE), first proposed by Mak *et al.* (1986) [93], accounts for both mechanisms. BPVE models for articular cartilage found in literature consider the solid

matrix to be either viscoelastic in shear [29] or in both shear and bulk deformation [26]. In these models, the solid stress is given by

$$\boldsymbol{\sigma}_E = \lambda e\mathbf{I} + 2\mu \int_0^t G(t-\tau)\frac{\partial \mathbf{e}}{\partial \tau}\,\mathrm{d}\tau \tag{3.18}$$

$$\boldsymbol{\sigma}_E = \lambda \int_0^t G(t-\tau)\frac{\partial e\mathbf{I}}{\partial \tau}\,\mathrm{d}\tau + 2\mu \int_0^t G(t-\tau)\frac{\partial \mathbf{e}}{\partial \tau}\,\mathrm{d}\tau \tag{3.19}$$

respectively, where τ is a relaxation time constant, $\mathbf{e}$ the deviatoric component of the elastic strain tensor and $G(t)$ is the relaxation function. It is common to express $G(t)$ as a series of discrete relaxation functions [29] described as

$$G(t) = 1 + \bar{G}\sum_{i=1}^{n} e^{-\frac{t}{\tau_i}} \tag{3.20}$$

In the BPVE models of Suh *et al.* [26] and DiSilvestro *et al.* [27–29], a three term expansion is assumed for defining $G(t)$. Thus, in addition to the biphasic material parameters in the isotropic case (E, ν and k), which describe the elastic response and the hydraulic permeability of the tissue, the BPVE model adds three more parameters, which are the discrete spectrum magnitude $\bar{G}$, a short term relaxation time constant $\tau_S = \tau_1$ and a long-term relaxation time constant $\tau_L = \tau_3$ ($\tau_2 = \tau_2(\tau_1, \tau_3)$).

The BPVE model has been applied for characterization of the time-dependent response of normal [27–29, 67, 94] and degenerated [67, 94] cartilage in confined and unconfined compression, and indentation.

3.6 Discussion

The complex mechanical behavior of articular cartilage has been primarily modeled using a basic linear biphasic poroelastic model (BPE) of articular cartilage developed by Mow *et al.* [24]. In this model the apparent viscoelasticity of the tissue

is assumed to be solely due to the fluid-flow dependent frictional drag interactions due to interstitial fluid flow through a porous solid matrix. The linear BPE model is able to explain the creep as well as stress relaxation long-term response during confined compression though significant deviation has been observed from the short-term response of the tissue during the early time period (<100 s) after application of load [20]. Furthermore, the utility of this model diminishes when the tissue is subjected to unconfined compression [8, 71] indicating that frictional interactions between the two assumed phases of articular cartilage may be insufficient to completely account for apparent viscoelasticity under loading conditions other than confined compression. Another likely reason for this is that the anisotropy of the tissue, which plays an important role during this test, is not included in this model.

DiSilvestro *et al.* [27] compared the response of the linear BPE model [24], the TIBPE model [68] and the BPVE model [26, 93] in their simultaneous prediction of the reaction force and lateral displacement during unconfined compression. They showed that the TIBPE model was able to account for either the measured lateral displacement or the measured reaction force very well, but could not account for both variables simultaneously. Also, the isotropic CLE model cannot account for lateral displacements and reaction forces simultaneously. Although the CLE and TIBPE models address the tension-compression nonlinearity of the tissue, the likely reason for this was the absence of flow-independent viscoelasticity, which results in the lateral stiffness remaining too high. This was confirmed by the fact that the BPVE model succeeded in simultaneously accounting for both the reaction force as well as the lateral displacement in unconfined compression. Moreover, the BPVE model is able to simultaneously account for experimental data measured from unconfined compression and either indentation or confined compression [29]. Another

study reported that the BPVE model can accurately simulate unconfined compression at varying strain rates [28]. However, not all these tests can be reproduced simultaneously by the BPVE model, probably due to the lack of anisotropy and tension-compression nonlinearity of the tissue.

A combination of the CLE and BPVE models used by Huang *et al.* [73], which included both flow-independent viscoelasticity and tension-compression nonlinearity of the solid matrix, could simultaneously account for the response of articular cartilage during unconfined compression at varying strain rates and its response to dynamic loading. This model produced better predictions of the dynamic modulus of cartilage in unconfined dynamic compression than the CLE and BPVE models, thus emphasizing the role of the intrinsic viscoelasticity and tension-compression nonlinearity of articular cartilage in its load-support mechanism. Fibril-reinforced poroviscoelastic models by Li *et al.* [83] and Wilson *et al.* [32, 87, 91] that include these two features have the advantage of a relating the tissue response to its microstructure.

Kääb *et al.* experimentally studied the deformation of the collagen network during loading using scanning electron microscopy and showed that the characteristics of the deformations differ between superficial fibrils and those at the cartilage-bone interface [95, 96]. Using the BPE model Wilson *et al.* [30] found that superficial damage could only be explained from stress analyses when assuming the cartilage to be anisotropic, but that damage of fibrils at the cartilage-bone interface can only be predicted in an isotropic model. Using a fibril-reinforced poroviscoelastic model, they concluded that the local stresses and strains in articular cartilage are highly influenced by the local morphology of the collagen-fibril network [87]. Hence, it is important to describe the collagen network as realistically as possible. This is better done by the continuum based models of Wilson *et al.* [32, 87, 91], in which

collagen fibrils can have different orientations, than the spring based models of Li *et al.* [81–83]. Garcia and Cortés [89] showed that inclusion of viscous effects in the matrix is consistent with experimental tensile tests, suggesting that intrinsic viscous effects in the matrix of articular cartilage plays an important role in the mechanical response of the tissue.

The swelling behavior of articular cartilage can also be included by combining models with the full mechano-electrochemical model, e.g. [75, 76], or the biphasic swelling model, e.g. [77]. The biphasic swelling model is computationally less expensive and applicable for large deformations.

As more and more features of AC structure and composition are included in the model, the number of unknown parameters to be determined increases, which likely increases the number of mechanical tests to extract the parameters. This puts an emphasis on using the simplest model that is sufficient to obtain the necessary information to answer the question posed. In the next chapter, we look at the development of a continuum model for the indentation of AC and the use of inverse finite element methods to extract model parameters from indentation tests on mouse cartilage.

Chapter 4

Poroviscoelastic properties of mouse cartilage by Inverse Finite Elements and Indentation

4.1 Overview

The content of this chapter is from the following published article [97]:

S. Chiravarambath, N.K. Simha, R. Namani and J.L. Lewis, Poroviscoelastic cartilage properties in the mouse from indentation. J Biomech Eng, 131 (2009), p. 011004 (9 pages).

A method for fitting parameters in a poroviscoelastic (PVE) model of articular cartilage in the mouse is presented. Indentation is performed using two different sized indenters and then these data are fitted using a PVE finite element program and parameter extraction algorithm. Data from a smaller indenter, a 15 μm diameter flat-ended 60° cone, is first used to fit the viscoelastic (VE) parameters, on the

basis that for this tip size the gel diffusion time (approximate time constant of the poroelastic (PE) response) is of the order of 0.1 s, so that the PE response is negligible. These parameters are then used to fit the data from a second 170 μm diameter flat-ended 60° cone for the PE parameters, using the VE parameters extracted from the data from the 15 μm tip. Data from tests on five different mouse tibial plateaus are presented and fitted. Parameter variation studies for the larger indenter show that for this case the VE and PE time responses overlap in time, necessitating the use of both models.

4.2 Background

Mouse models are useful for understanding disease processes in articular cartilage, particularly osteoarthritis, and many mutant and transgenic mouse models are available. As part of this development, there is recent interest in linking the mechanical properties of cartilage in the mouse to basic tissue constituents (e.g., Refs. [33, 98–100]). This presents the challenge of measuring mechanical properties of small volumes of cartilage. Indentation appears to have the potential for providing these properties and Cao *et al.* [33] recently reported a micro-indentation test in the mouse and a biphasic finite element fitting procedure. This was the first reported combination of experimental method and consistent continuum model for indentation of mouse cartilage and represented a considerable advancement over previous methods. However, there is a question if the biphasic model alone is appropriate for this test condition.

There is a long history of cartilage testing and development of continuum models for data reduction. The biphasic model of Mow *et al.* [24] has long been prominent in the field. It was realized that this model could not fit both the short and

long time responses of cartilage loading, leading to the introduction of PVE models [26,27,93], which included both biphasic or PE flow-dependent time dependency and VE flow-independent time dependency. These models agreed much better with the experimental data, but there were too many parameters to fit, resulting in question of uniqueness of the fit parameters. This condition was made more challenging by the fact that the time ranges for the PE and VE processes overlapped in most of the experimental test conditions. Huang *et al.* [73] proposed a method to separate viscous and PE relaxation responses based on the known tension-compression nonlinearity in cartilage, which results in a negligible flow-dependent response for a tensile test of a thin strip of the tissue. Therefore, this test could be used to deduce only the VE parameters, requiring fit of fewer parameters. These could then be used in a PVE model of a different test configuration, with the VE parameters known, to identify the PE parameters from a compression test, in which both flow-dependent and flow-independent responses occur. Unfortunately, this method cannot be used for mouse cartilage, because a tensile test cannot be performed because of the small size of the mouse joint.

In the theoretical analysis of indentation of a biphasic layer by Mak *et al.* [65], it is shown that the stress relaxation for a ramp and hold indentation displacement is controlled by a rate of compression parameter, $R_0 = \kappa H_A / V_0 h$, where κ is permeability, H_A the aggregate modulus, h the layer thickness, and V_0 is the indentation rate. They show that for $R_0 \gg 1$ there is negligible resistance to fluid flow and influence of fluid flow on response. For creep indentation, they show that the time response scales with the factor $T_g = a^2 / H_A \kappa$ where a is the radius of the flat indenter, and that this becomes the approximate time constant of the resistance to fluid flow. The factor T_g is referred to as the characteristic gel diffusion time in all subsequent studies. We propose to use flat-ended conical indenters with flat end

diameters of 15 and 170 μm. For a flat-ended cylinder with an end diameter of 15 μm, and for typical values of H_A, κ, and h, of 3.5 MPa, 0.23×10^{-15}m^4/N-s, and 60 μm, respectively, the time scale factor is approximately 0.07 s. Also for our test conditions of a ramp displacement of 4 μm in 4 s, R_0 is approximately 10^6. Both of these imply that there is negligible fluid flow effect for our indentation tests of mouse cartilage with a 15 μm tip. Therefore, any time dependency of the response must be due to viscoelasticity and this test can be used to fit the VE parameters. For a 170 μm diameter tip, T_g is approximately 8.7 s, which, although still small, is large enough to stimulate a fluid flow effect in the tests. Data from the 170 μm test can be used in a PVE theory to identify the PE parameters, with the VE parameters known from the first fit. Application of this method to cartilage on the mouse tibia is presented in the following sections.

4.3 Methods

Indentation tests were performed on cartilage on the mouse tibia plateau using flat-ended conical tips with flat-end diameters of 15 and 170 μm. A finite element (FE) model of the test was developed and the PVE parameters were identified by using inverse methods to minimize the error between FE simulated and test data. Inverse FE fit for the 15 μm data was used to extract VE parameters and that for the 170 μm data to extract PE parameters. In order to demonstrate the consequences of ignoring the flow-independent viscoelasticity, a simulation was also run for both tips to identify PE parameters using a purely PE model. To verify that the PE response was negligible for the 15 μm tip, simulations were run and the permeability varied.

4.3.1 Experimental Methods

Specimen Preparation

Mouse knee joints from six week old CD-1 female mice were used for testing. These animals had been used in other experiments that did not involve cartilage and any mechanical testing and their knee joints had been removed and frozen at $-20\,^{\circ}\mathrm{C}$ prior to testing. The joint was thawed and dissected under a microscope to isolate and expose the cartilage surface around the femur and tibia. The tibial plateau was then separated with approximately 1 mm of bone under the cartilage. The bottom of the bone was mounted onto a holder using cyanoacrylate cement. The holder could be rotated so that a relatively flat region on the cartilage specimen could be oriented perpendicular to the indenter. The holder was then installed in the test machine specimen tray for indentation. A droplet of phosphate buffered saline (PBS) was maintained on the specimen surface at all times. Tests were performed on five different tibial specimens.

Nano-indentation Tests

A Nanoindenter XP (MTS Inc., Eden Prairie, MN) was used to perform indentation tests. This instrument can measure load and displacement with resolutions of ~ 0.02 mN and ~ 30 nm, respectively. The indenters used for testing were flat-ended conical indenters (cone angle of 60°) with flat-end diameters of 15 μm and 170 μm. The 15 μm tip was diamond, adhered to stainless steel, while the 170 μm tip was stainless steel. The stress relaxation tests were performed on the tibial plateau of mouse at roughly the same locations with both indenters. The test protocol was a preload (indent depth ~ 2 μm) applied and held for ~ 300 s to ensure contact, followed by a ramp load at 1 μm/s to 4 μm and held for ~ 300 s.

After testing with both tips, the tip was changed to a sharp (end radius < 1 μm)

tip and the cartilage thickness measured by penetration tests at approximately the same locations as the indentation tests. The cartilage was indented until the tip hit the underlying bone. The linear region of bone indentation was extrapolated to zero force level and the thickness was set to the corresponding displacement obtained at zero force. In separate tests (not reported here), the thickness measured by this procedure agreed well with thickness measured by histology. The average thickness over all specimens was determined to be ~ 60 μm.

Cartilage Model for Data Reduction

Articular cartilage was modeled as homogeneous isotropic PVE or VE layer. The initial void ratio for the layer was set to 4 based on literature [24, 34] and the permeability was set to be isotropic. Following Suh *et al.* [71], the viscoelastic properties for the solid matrix were assumed isotropic and defined by the relaxation functions for the shear and bulk moduli as

$$K(\tau) = \frac{3E^{\infty}}{1+\nu^{\infty}} \tag{4.1}$$

$$G(\tau) = \frac{E^{\infty}}{2(1+\nu^{\infty})(1-\sum_1^n g_i)}\left[1-\sum_1^n g_i\left(1-e^{-\frac{\tau}{\tau_i}}\right)\right] \tag{4.2}$$

where K and G are the bulk and shear moduli, E^{∞} is equilibrium Young's modulus, ν^{∞} is equilibrium Poisson's ratio, and g_i and τ_i are the viscous relaxations constants and τ denotes the time. The indentation stress relaxation of articular cartilage has a rapid short term response and a slower long term response, which implies that a minimum of two different time constants should define the relaxation. Suh *et al.* [71] observed that $n = 3$ and a uniform decadic (10-base logarithmic) interval of τ_i was efficient and comparable to a continuous spectrum model. In the relaxation response of our mouse cartilage specimens, an initial sharp fall in the force was seen. To account for this, we let g_1 be different from $g_2 = g_3$. Also, the intermediate

relaxation rate, τ_2 was defined as

$$\log\tau_2 = \frac{(\log\tau_1 + \log\tau_3)}{2} \tag{4.3}$$

resulting in four independent VE parameters, g_1, τ_1, g_3 and τ_3. In addition to the four VE parameters, there were three PE parameters: permeability, κ, ν^∞ and E^∞, for a total of seven material parameters for the FE model.

Thus, in this formulation, a PVE model has seven parameters as mentioned above (g_1, τ_1, g_3, τ_3, κ, ν^∞ and E^∞), a VE model has six parameters (g_1, τ_1, g_3, τ_3, ν^∞ and E^∞), and a linear elastic (LE) model has only two parameters (ν^∞ and E^∞).

4.3.2 Numerical Methods

Finite Element Model

Indentation of a PVE material with a rigid flat-ended 60° conical indenter was modeled using the commercial FEA software ABAQUS/Standard v6.5 (Hibbit, Karlsson & Sorensen, Inc., Providence, RI). Articular cartilage was modeled as a layer bonded to a rigid and impermeable substrate being indented by a rigid and impermeable indenter as shown in Fig. 4.1. Due to the symmetry of the problem, an axisymmetric analysis was performed. The radial dimension of the cartilage layer was set to two times the thickness for the 15 μm indenter based on preliminary simulations. This was scaled to $\sim 0.8d$ for the 170 μm indenter, where d is the diameter of the indenter tip. The model was changed to the measured thickness for each specimen. Meshes with 1600 bilinear elements of type CAX4R (non-porous elements for VE only model) and CAX4RP (porous elements for PVE model) were used. A higher node density was used in regions of high stress (near the indenter tip edge). The contact between the indenter and cartilage was defined as a finite sliding contact

with no friction. The boundary conditions were specified by constraining the r and z displacement of the substrate (rigid) and the r displacement along the axis of symmetry. The lateral side of the cartilage layer was unconstrained and the surface traction (pore pressure of fluid and contact pressure on solid) along the sides and the top surfaces was made zero except below the indenter. As a result of these boundary conditions, fluid was free to flow from the sides and the top. The analysis was run as a geometrically nonlinear analysis that allowed for large deformations. The displacement input in the simulations exactly matched the displacement versus the time profile used for the experiments. The resulting force data from FE was fitted to measurements to extract parameters.

Parameter extraction using an Inverse algorithm

An inverse algorithm program was used along with the FE model to extract the PVE parameters. The inverse FE method described here follows the work of Namani [101]. Briefly, the FE indentation model simulates the forward problem and the parameters are extracted by using the SIMPLEX algorithm [102] to maximize the coefficient of determination, R^2, between the experimental and FE predicted data.

As with all multidimensional optimization algorithms, the SIMPLEX algorithm requires starting points, and was given $m+1$ initial starting points or vectors, where m is the number of parameters to be extracted. The initial points were chosen covering a wide range in the parameter space based on estimates of PVE parameters from indentation experiments of DiSilvestro and Suh [27]. The algorithm compared the output from the FE model for each of these starting points to the experimental data and converged to the maximum of the objective function (Eq. (4.4)) with the prescribed convergence criteria, where P_i denotes the experimental indentation force measured at time t_i, while $\bar{P}_i$ is obtained from the FE model at trial parameter

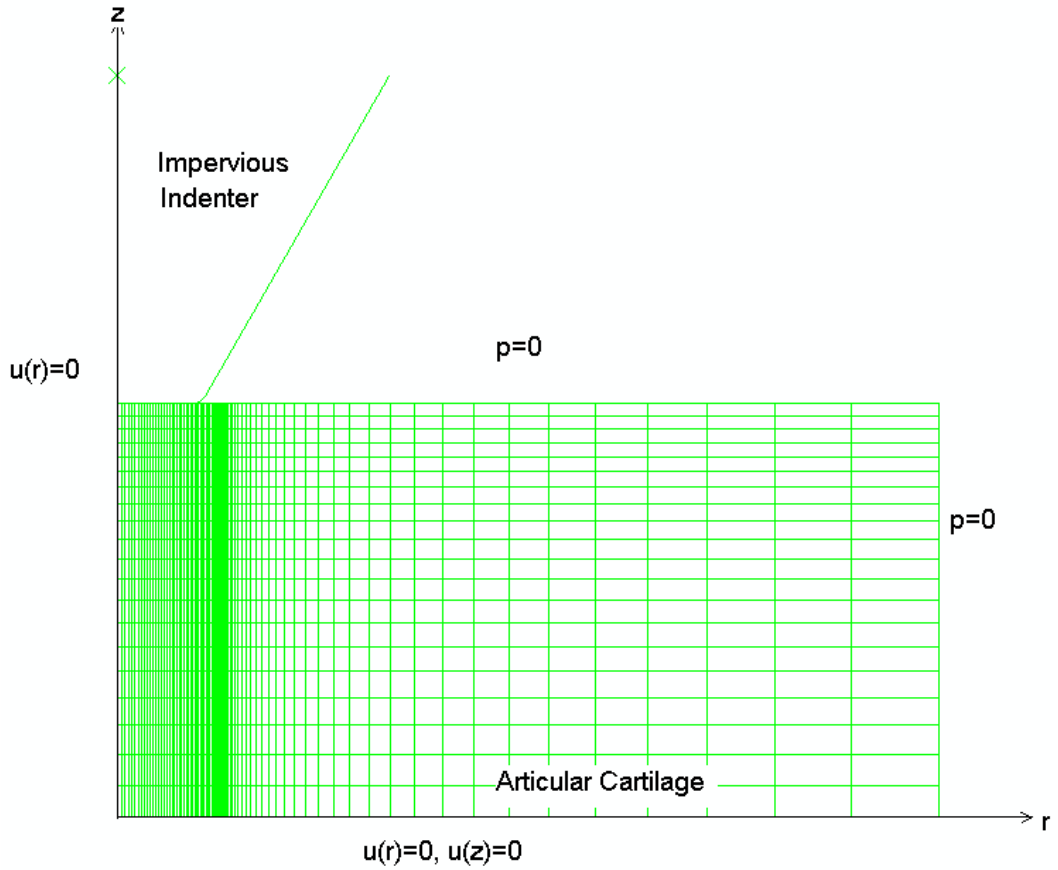

Figure 4.1: FE model for nano-indentation of mouse cartilage using flat-ended conical indenter. The z axis is the axis of symmetry. The top and right surfaces are permeable $p = 0$ and traction free. The displaced of the bottom is fixed. The indenter is impervious. Mesh is denser under the indenter and near the indenter edge.

values:

$$R^2 = 1 - \frac{\sum_1^p (P_i - \bar{P}_i)^2}{\sum_1^p (P_i)^2 - \frac{1}{p}\left(\sum_1^p P_i\right)^2} \tag{4.4}$$

Convergence was said to be reached when a curve-fit of $R^2 \geq 0.9$ was obtained at all $m+1$ points. The program stopped when the number of iterations reached 100 or when corresponding parameters being extracted at the vertices of the polygon were within 1% of their respective means. For one of the tests, the parameters were extracted with three different sets of starting points for both indenters to assess the influence of the choice of the starting points.

Fitting procedure

Step 1 The experimental force-time data from the 15 μm indentation was curve fitted with a purely VE model. Of the six parameters, the value of ν^∞ was fixed to 0.25 and the theoretical equilibrium modulus E_{th}^∞ was evaluated using the expression from the theory of Hayes [103] extended to flat-ended cones by Simha *et al.* [19] given by

$$E_{th}^\infty = \frac{P^\infty \left[1 - (\nu^\infty)^2\right]}{2a\delta^\infty \kappa_{fec}} \tag{4.5}$$

where P^∞ is the force at equilibrium, δ^∞ is the displacement at equilibrium, a is the radius of the indenter flat-end κ_{fec} is the correction factor for flat-ended cones. It was assumed that equilibrium was reached at the end of the hold period and using the data point at the end of relaxation (P_{exp}^∞), the theoretical equilibrium modulus was calculated from Eq. (4.5). This value of E_{th}^∞ was used in the FE model to predict equilibrium force (P_{FE}^∞). It was observed that the equilibrium force measured at the end of the hold, i.e., $P_{\text{FE}}^\infty > P_{\text{exp}}^\infty$. We believe this was due to lack of true equilibrium at the end of the hold period and a radius at the edge of the indenter. Therefore, in the FE model, E^∞ was set to $E^\infty = \alpha E_{\text{th}}^\infty$, where $\alpha = P_{\text{exp}}^\infty / P_{\text{FE}}^\infty$. α was chosen as 0.9 as a consequence of the results from the sensitivity study (explained below).

Step 2 The experimental force-time data from the 170 μm indentation was then curve fitted with a biphasic PVE model. Of the seven parameters, the values of the four VE parameters were fixed to those extracted from Step 1 and the remaining three parameters, κ, ν^∞ and E^∞ were extracted.

To understand the contribution of different physical processes, purely LE, purely PE, purely VE and PVE curves were generated from the final fit parameters and compared with the experimental force versus time data for the 170 μm tip.

Sensitivity Study

$\alpha = 0.9$ was chosen based on a study of the sensitivity of fitted VE parameters for various values of α, as follows. The experimental data from the 15 μm indenter was fitted with values of α ranging from $0.85 - 1.0$. For a range of α, g_1, and τ_1 were the same, so these were kept constant and a second step fit of g_3, τ_3, and E^∞ was performed. This was assumed to give an optimal E^∞. For the same set of experimental data, the standard procedure was employed with $\alpha = 0.9$ to show that the same results were obtained as with this procedure, which was assumed to be more accurate.

PE Fits

Other studies [33] have used a PE model for mouse cartilage. For comparison, the experimental force-time data from both indenters was also curve fitted with a purely PE model. In this case, the three PE parameters (κ, ν^∞ and E^∞) were extracted using our inverse FE algorithm.

Parametric study of permeability

Simulations for a PE model were run for a variation of four orders of magnitude in permeability, ranging from $10^{-17} - 10^{-14}$ m^4/N-s for both, the 15 μm and 170 μm indenters. The force versus time was predicted using the experimental displacement versus time as input. The intention here was to determine the sensitivity of the force response to variation in permeability. If the force was insensitive to permeability, this would imply that there was no flow-dependent time response, supporting the assumption of VE only.

Computational Resources

All FE simulations were run on Linux workstations at the Minnesota Supercomputing Institute (MSI). These workstations had a variety of processors ranging from 3.4 GHz Intel Xeon to quad core AMD 2.4 GHz and each had a memory of at least 4 Gbytes (maximum of 16 Gbytes).

4.4 Results

4.4.1 Experiments

The mouse cartilage showed a typical stress relaxation response from the indentation experiments (Figs. 4.2 and 4.3). The force steadily increased during the ramp loading and showed a characteristic relaxation during the hold period when the displacement was held approximately constant. The force relaxes during the hold period, although the nanoindenter displacement drifts due to the inability of the test machine to maintain a constant displacement for a load change.

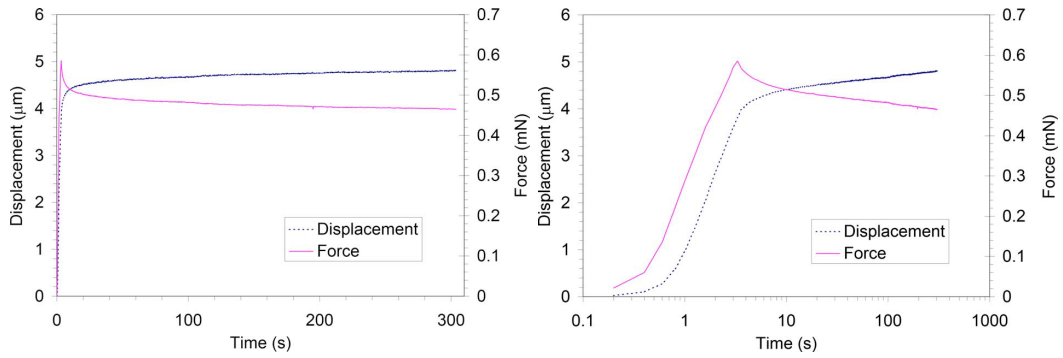

(a) Normal scale (b) Logarithmic time scale

Figure 4.2: Experimental force and displacement curves for the 15 μm indenter in (a) normal and (b) logarithmic time scales.

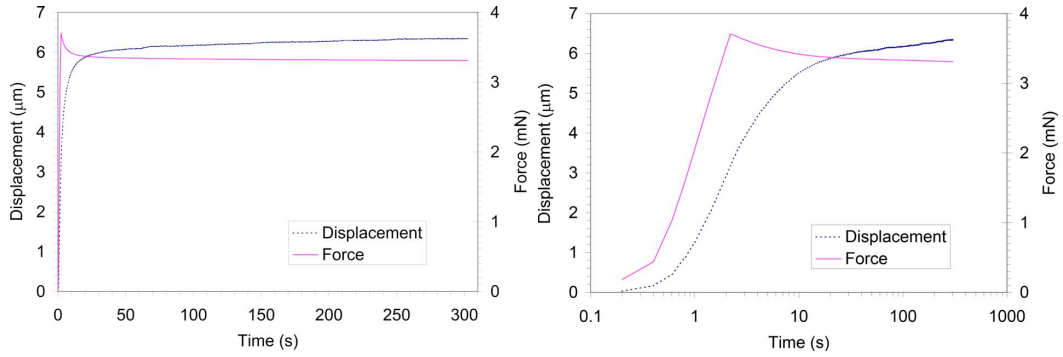

(a) Normal scale (b) Logarithmic time scale

Figure 4.3: Experimental force and displacement curves for the 170 μm indenter in (a) normal and (b) logarithmic time scales.

Table 4.1: Model parameters extracted for mouse cartilage by inverse FE fits to indentation data for the 15 μm and the 170 μm indenters. Values reported are average (s.d.) of all points of the extraction procedure.

(a) VE parameters from 15 μm data: $\nu^\infty = 0.25$, $E^\infty = 0.9E^\infty_{\text{th}}$

Spec. No.	g_1	$g_2 = g_3$	τ_1 (s)	τ_3 (s)	R^2	E^∞ (MPa)
1	0.47 (0.001)	0.08 (0.001)	1.17 (0.002)	150 (01)	0.93	5.45
2	0.59 (0.050)	0.06 (0.007)	1.09 (0.210)	170 (19)	0.94	4.78
3	0.59 (0.002)	0.09 (0.001)	1.49 (0.010)	140 (01)	0.91	2.35
4	0.49 (0.002)	0.09 (0.001)	1.23 (0.010)	140 (01)	0.92	3.83
5	0.38 (0.003)	0.11 (0.001)	0.95 (0.010)	170 (01)	0.92	4.73
Mean	0.53 (0.085)	0.08 (0.017)	1.20 (0.210)	160 (17)	0.93 (0.01)	4.20 (1.2)

(b) PE parameters from 170 μm data and VE parameters from the 15 μm data

Spec. No.	$\kappa \times 10^{-15}$ (m^4/N-s)	ν^∞	E^∞ (MPa)	E^∞_{th} (MPa)	R^2
1	1.90 (0.01)	0.17 (0.001)	0.93 (0.001)	0.99 (0.001)	0.89 (0.001)
2	1.10 (0.04)	0.20 (0.010)	0.83 (0.010)	0.89 (0.010)	0.91 (0.004)
3	6.70 (0.05)	0.20 (0.001)	0.54 (0.000)	0.57 (0.001)	0.91 (0.000)
4	2.10 (0.02)	0.20 (0.002)	1.10 (0.002)	1.10 (0.002)	0.96 (0.000)
5	0.71 (0.01)	0.23 (0.001)	0.41 (0.000)	0.44 (0.000)	0.90 (0.000)
Mean	2.10 (1.90)	0.20 (0.020)	0.77 (0.210)	0.82 (0.220)	0.92 (0.020)

4.4.2 Numerical Results

Parameter Extraction

Table 4.1 gives a summary of all the parameters extracted for all specimens.

Step 1 The mean (s. d.) values for the VE parameters were as follows: $g_1 = 0.53$ (0.085), $\tau_1 = 1.2$ (0.21) s, $g_2 = g_3 = 0.08$ (0.017) and $\tau_3 = 160$ (17) s (Table 4.1a). The curve fit had an average R^2 value of 0.93 (0.01). The force response for the 15 μm indenter with fit parameters for one of the specimens is shown in Fig. 4.4.

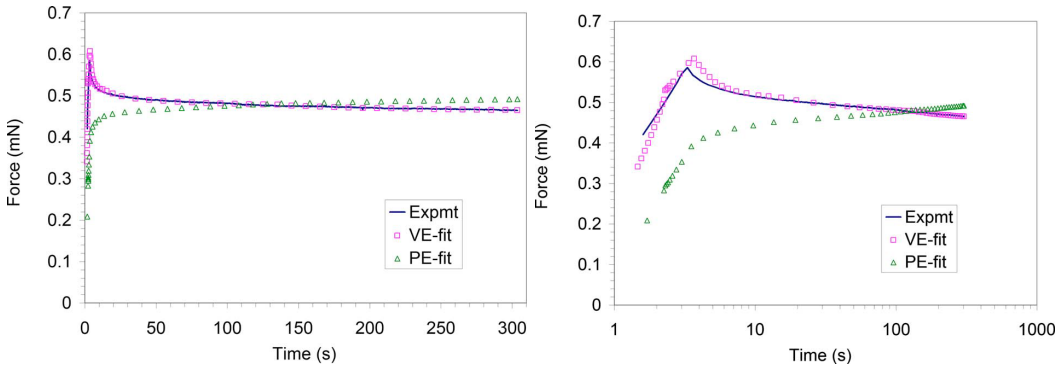

(a) Normal scale (b) Logarithmic scale

Figure 4.4: Experimental and curve fit (VE and PE) force versus time curves for indentation with the 15 μm tip. VE fit is better than a PE fit.

The VE fit to the small indenter data is able to capture the peak force as well as the stress relaxation to the end of the hold period. Also, the VE fit matches the experimental data at short and long time regions.

Step 2 With the VE parameters fixed at the extracted values, a PVE fit to the 170 μm data extracted the following values for the PE parameters: $\kappa = 2.1\ (1.9)\times 10^{-15}$ m4/N-s, $\nu^{\infty} = 0.20\ (0.02)$, and $E^{\infty} = 0.77\ (0.21)$ MPa (Table 4.1b). The curve fit had an average R^2 value of 0.92 (0.01). For comparison, the indentation E^{∞}_{th} is included in Table 4.1b. The force response for the 170 μm indenter with fit parameters for one of the specimens is shown in Fig. 4.5. As with the VE fit for the 15 μm indenter, the PVE fit for the 170 μm indenter data matches both the short time and long time regimes of the experimental data.

For one of the specimens, parameters were extracted with three different sets of starting points for both indenters (Table 4.2). Of the VE parameters extracted, g_1 was in the range $0.53 - 0.69$, g_3 was in the range $0.048 - 0.072$, τ_1 in the range $0.70 - 1.35$ s, and τ_3 in the range $140 - 190$ s. The R^2 of the fit varied from 0.94 to 0.96. Of the PVE parameters extracted, κ was in the range $1.03 - 1.14 \times 10^{-15}$

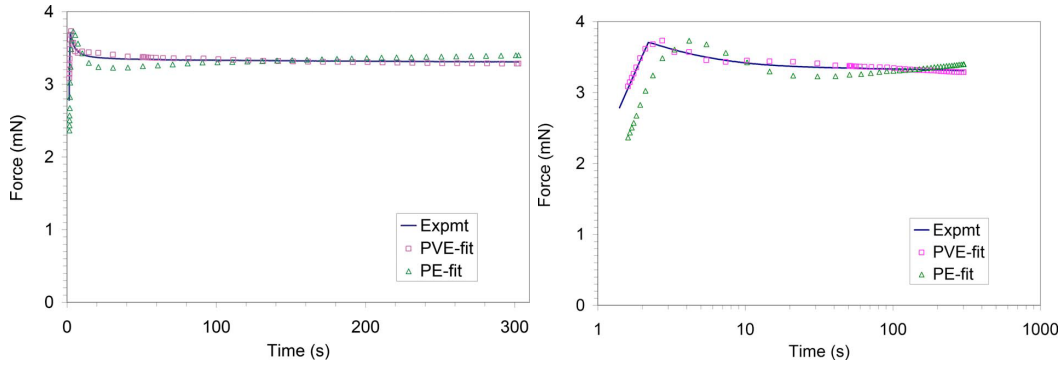

(a) Normal scale (b) Logarithmic scale

Figure 4.5: Experimental and curve fit (PVE and PE) force versus time curves for indentation with the 170 μm tip. PVE fit is better than a PE fit.

m4/N-s, ν^∞ in the range $0.19 - 0.22$, and E^∞ in the range $0.82 - 0.84$ MPa. The R^2 of the fit varied from 0.89 to 0.92. For comparison, the value of E^∞_{th} for each specimen is also included in Table 4.1b. Note that $E^\infty \neq \alpha E^\infty_{\text{th}}$ with $\alpha = 0.9$, because conditions are different from the 15 μm tip.

The choice of $\alpha = 0.9$, $E^\infty = \alpha E^\infty_{th}$, used for extracting the VE parameters, was examined. When α was varied from 0.85 to 1.0 (data from one specimen), it was seen that the coefficient of determination, R^2, was 0.90 or higher only when $\alpha \leq P^\infty_{exp}/P^\infty_{FE} \approx 0.9 - 0.85$ (Table 4.3a, Fig. 4.6). In addition, similar values for g_1 and τ_1 were obtained for $\alpha \approx 0.9 - 0.85$. Therefore, the parameters g_1 and τ_1 were fixed to values $g_1 = 0.478$ and $\tau_1 = 1.20$ s (averaged for the curve fits with $R^2 > 0.90$) and used to extract g_3, τ_3, and E^∞. The average values of the extracted parameters were $g_2 = g_3 = 0.076$ (0.001), $\tau_3 = 125$ (0.39) s, and $E^\infty = 5.52$ (0.002) MPa. The data used for the fits in Table 4.3 was for specimen 1. Comparing the mean data from Table 4.3b with the fit data for specimen 1 in Table 4.1a, in which the normal procedure with $\alpha = 0.9$ was used, shows that the two agree closely. For this specimen, $E^\infty_{th} = 6.05$ MPa, which gave $\alpha = 0.9$. This value of α was used in all subsequent fits of the 15 μm data for the VE parameters.

Table 4.2: Parameters extracted with different initial points.

(a) VE parameters from 15 μm indentation data

	Starting points for inverse FE				Extracted parameters				
Set No.	g_1	$g_2 = g_3$	τ_1 (s)	τ_3 (s)	g_1	$g_2 = g_3$	τ_1 (s)	τ_3 (s)	R^2
1	0.80	0.05	2.0	50	0.53	0.072	1.3	160	0.94
	0.60	0.07	1.5	70	0.53	0.071	1.3	160	0.94
	0.44	0.09	1.1	90	0.54	0.070	1.3	160	0.94
	0.36	0.11	0.9	110	0.53	0.071	1.3	160	0.94
	0.16	0.20	0.4	150	0.54	0.071	1.4	160	0.94
2	0.40	0.08	1.2	75	0.60	0.060	1.1	190	0.94
	0.50	0.10	0.8	110	0.59	0.061	1.1	190	0.94
	0.30	0.06	1.4	100	0.60	0.061	1.1	190	0.94
	0.60	0.12	1.0	130	0.59	0.061	1.1	190	0.94
	0.65	0.07	1.5	85	0.59	0.061	1.1	190	0.94
3	0.40	0.05	0.7	120	0.60	0.064	0.9	140	0.95
	0.70	0.10	1.2	85	0.64	0.056	0.9	150	0.95
	0.55	0.09	1.6	100	0.66	0.056	0.8	150	0.96
	0.60	0.065	0.95	140	0.60	0.065	1.0	140	0.95
	0.30	0.14	1.0	70	0.69	0.048	0.7	150	0.96

(b) PE parameters from 170 μm indentation data

	Starting points for inverse FE			Extracted parameters			
Set No.	$\kappa \times 10^{-15}$ (m^4/N-s)	ν^∞	E^∞ (MPa)	$\kappa \times 10^{-15}$ (m^4/N-s)	ν^∞	E^∞ (MPa)	R^2
1	0.02	0.16	1.00	1.0	0.22	0.82	0.89
	0.20	0.30	9.50	1.0	0.22	0.82	0.89
	2.0	0.12	1.10	1.0	0.22	0.82	0.89
	0.002	0.20	0.80	1.0	0.22	0.82	0.89
2	2.8	0.13	0.74	1.1	0.21	0.83	0.91
	1.4	0.19	0.84	1.1	0.21	0.82	0.91
	0.008	0.35	0.94	1.1	0.21	0.82	0.92
	0.028	0.21	0.56	1.1	0.21	0.82	0.91
3	0.010	0.10	0.94	1.1	0.19	0.84	0.91
	2.4	0.22	1.08	1.1	0.19	0.84	0.91
	0.080	0.15	1.00	1.1	0.19	0.84	0.91
	1.0	0.19	0.84	1.1	0.19	0.84	0.91

Table 4.3: Sensitivity study of E^∞ on the VE parameters extracted from the 15 μm indentation data. For this specimen, $E^\infty_{\text{calc}} = 6.051$ MPa for $\nu^\infty = 0.25$. Values reported are average (s.d.) for all points.

(a) Extracted g_3, τ_3 and E^∞ parameters for various α

α	g_1	$g_2 = g_3$	τ_1 (s)	τ_3 (s)	R^2
1.0	0.45 (0.001)	0.063 (0)	1.1 (0.001)	19 (0.084)	< 0.1
0.95	0.51 (0.002)	0.054 (0.001)	1.3 (0.001)	77 (0.31)	0.71
0.90	0.48 (0.002)	0.079 (0.001)	1.2 (0.004)	160 (0.64)	0.93
0.88	0.48 (0.002)	0.083 (0.001)	1.2 (0.005)	210 (0.86)	0.93
0.85	0.48 (0.002)	0.091 (0.001)	1.2 (0.004)	320 (1.6)	0.93

(b) Extracted VE parameters g_3, τ_3 and E^∞ with $g_1 = 0.478$ and $\tau_1 = 1.196$ s from (a)

	$g_2 = g_3$	τ_3 (s)	E^∞ (MPa)	R^2
1	0.076	120	5.5	0.92
2	0.076	120	5.5	0.92
3	0.076	120	5.5	0.92
4	0.075	120	5.5	0.92
Mean	0.076 (0.001)	120 (0.39)	5.5 (0.002)	0.92 (0.002)

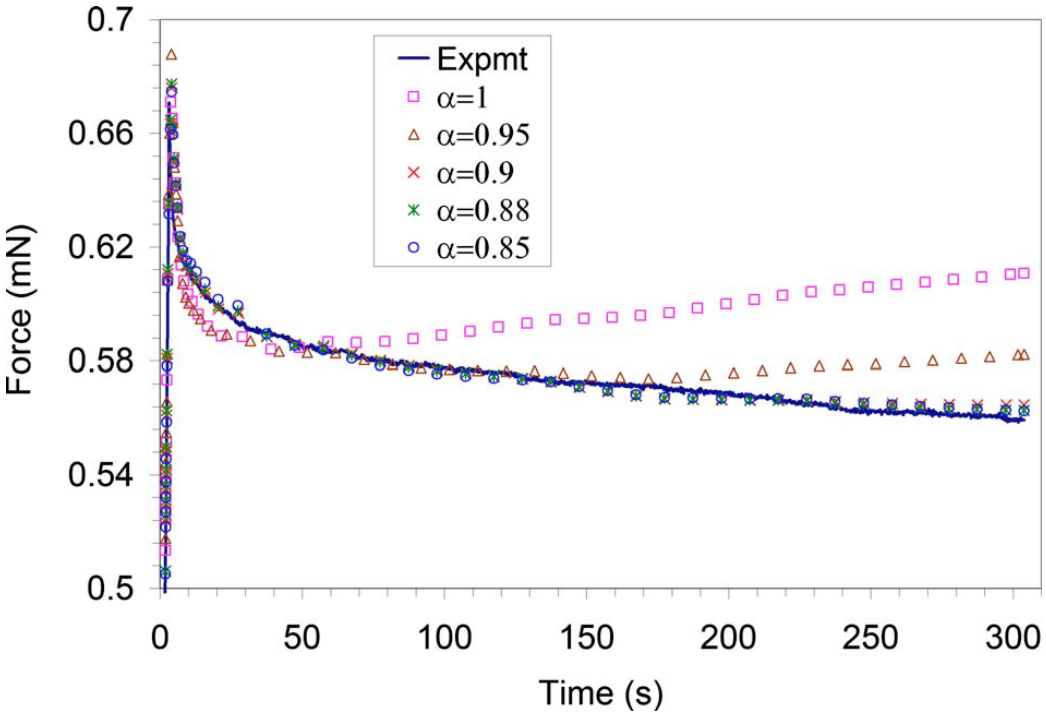

Figure 4.6: Sensitivity study for E^{∞} from the 15 μm indenter.

PE Fits

For the purely PE model, the average values of the extracted parameters were $\kappa = 0.96\ (0.02)\ \times 10^{-15}$ m^4/N-s, $\nu^\infty = 0.193\ (0.002)$ and $E^\infty = 5.3\ (0.01)$ MPa for the 15 μm indenter and $\kappa = 0.39\ (0.003)\ \times 10^{-15}$ m^4/N-s, $\nu^\infty = 0.23\ (0.001)$ and $E^\infty = 0.85\ (0.001)$ MPa, respectively, for the 170 μm indenter. However, these curve-fits were not good with average $R^2 < 0.3$ (Figs. 4.4 and 4.5).

Parametric Study of Permeability

A variation of four orders of magnitude in permeability had no effect on the stress response predicted by the FE model for the 15 μm indenter (Fig. 4.7a). In contrast, there was a distinct change in the stress relaxation predicted by the FE model for the 170 μm indenter (Fig. 4.7b). As the permeability decreased, it took longer for the stress to reach equilibrium.

Figure 4.8 shows the curves simulated for purely LE, purely PE, purely VE, and PVE models using the final extracted parameters for one of the specimens for the 170 μm tip. The LE model was, as expected, able to match neither the short term nor the long term response of the experimental data. This matched the displacement input. With the PE model, there was a significant increase in the short term response relative to the elastic model; however, it was still much below the experimental curve. The response of the PE model beyond $\sim$ 11 s exactly matched that of the LE model, implying that there was no flow-dependent effect after that point. With the VE model, there was a slight increase in the force over the LE solution in the loading period; however, the model could account for the entire response beyond $\sim$ 12 s, implying that the long term time dependency was due to the VE effect, not the PE effect. When the PVE model was used, the peak force increased significantly and the model could account for the short term and the long term response of the

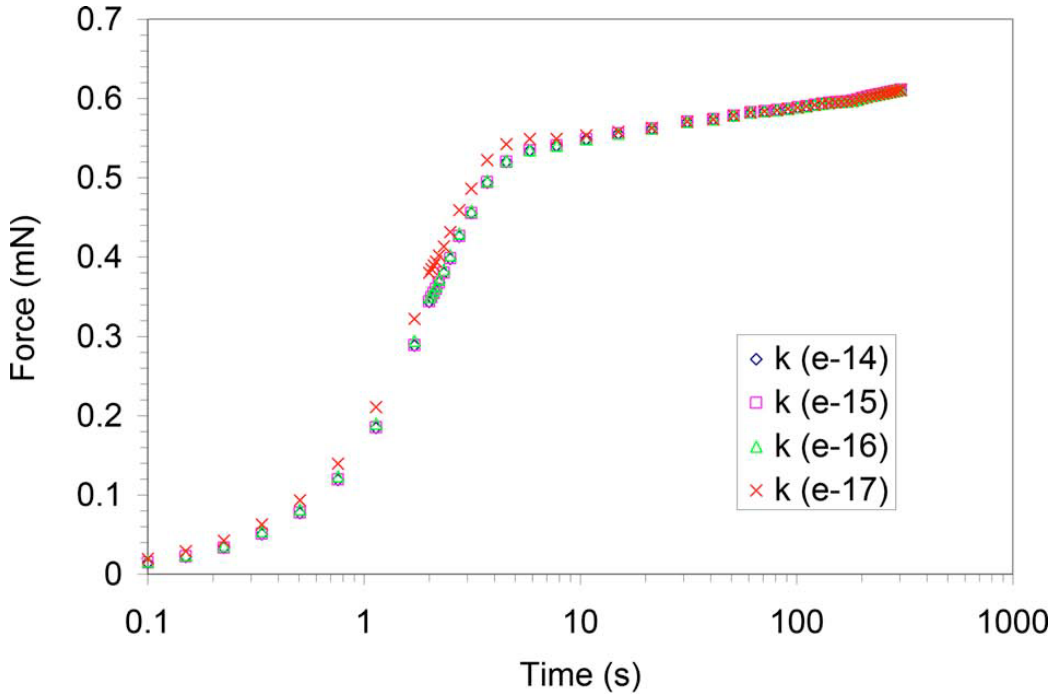

(a) 15 μm tip

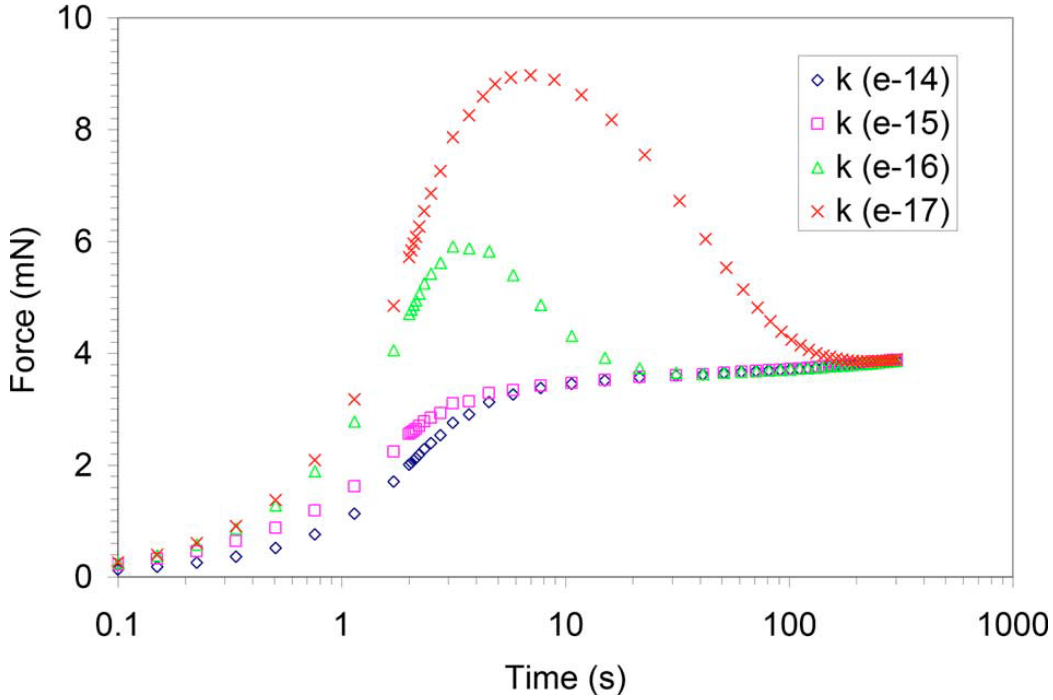

(b) 70 μm tip

Figure 4.7: Effect of varying permeability in the range $10^{-17} - 10^{-14}$ m^4/N-s for the PE model of indentation of mouse cartilage by the 15 μm and 170 μm tips.

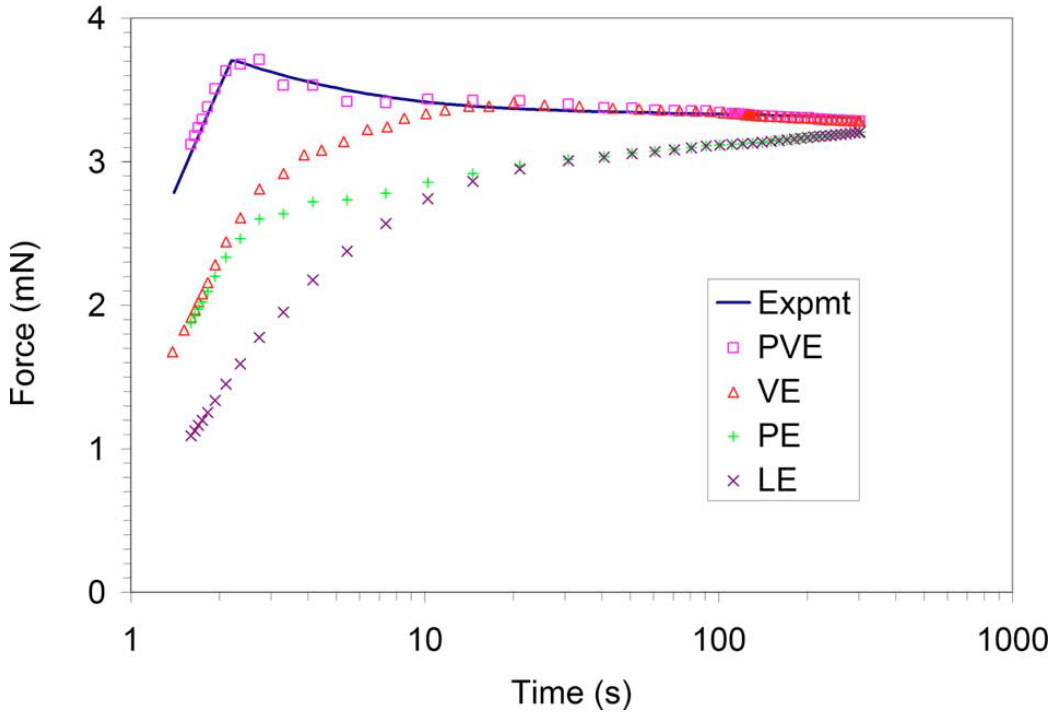

Figure 4.8: Role of various physical processes. Curves are generated using the fit parameters from Table 4.1.

cartilage specimen.

Computation Time

The computation time for the fitting procedure (for both tips) varied from 2.5 h to 5 h depending on the workstation used. The average computation time was ~ 4 h. Code was not parallelized so these times are for single processors.

4.5 Discussion

This study demonstrates a method to separate fluid flow-independent and flow-dependent processes of articular cartilage in indentation testing in the mouse and to extract the PVE parameters of articular cartilage in this setting. Nanoindentation

testing of mouse cartilage was accomplished using two different sized indenters: flat-ended conical indenters with flat-end diameters of 15 μm and 170 μm. The rationale for using two different sized indenters was that for the 15 μm tip the characteristic gel diffusion time, $T_g \approx 0.1$ s, is negligibly small, and hence indentation with this small tip would not probe flow dependent processes for the loading protocol used. This was confirmed by a PE FE model of indentation, which showed that the stress relaxation response was insensitive to permeability changes from $10^{-17} - 10^{-14}$ m^4/N-s when indented with the 15 μm indenter (Fig. 4.7a). This allowed neglecting permeability for this indenter, and indentation data was fit to a VE model with fixed values of the equilibrium elastic parameters, ν^∞ and E^∞.

The 170 μm indenter has a significant $T_g \approx 10$ s and is large enough to probe flow-dependent processes with our test conditions. This was confirmed by the PE model of indentation which showed clearly that the stress relaxation response was sensitive to permeability changes from $10^{-17} - 10^{-14}$ m^4/N-s when indented with a 170 μm indenter. The data from the 170 μm indentation were fitted to a PVE model (flow-dependent parameters) using the values of the flow-independent parameters from Step 1. The fit was good ($R^2 = 0.92$, Fig. 4.5) and the average values of the extracted parameters with the 170 μm tip ($E^\infty = 0.77$ MPa, $\kappa = 2.1 \times 10^{-15}$m^4/N-s and $\nu^\infty = 0.2$) were slightly different but in the same range as found by Cao *et al.* [33] for mouse cartilage (2 MPa, 1.1×10^{-16}m^4/N-s, 0.20 with a 110 μm indenter and using a PE model). The mean value of E^∞ was $\sim 6\%$ less than the theoretical value calculated using the extended theory of Hayes *et al.* [103] (Eq. (4.5)) (mean: 0.82 (0.22) MPa). We believe that this difference reflects both the fact that equilibrium was not reached in our experiments and the effect of a radius at the edge of the flat surface of the indenter, which causes a smaller contact area in the model compared to the modified theory of Hayes *et al.* [103]. These data support

that there is negligible fluid flow effect for the 15 μm tip and small effect for the 170 μm tip. The main cause of time dependency in the indentation with the 15 μm tip in this mouse cartilage is flow-independent viscoelasticity. Both processes are active in the indentation with the 170 μm tip, but the flow-independent viscoelasticity is the dominant process at longer times. Significant force increase due to the fluid flow is gone after approximately 11 s (Fig. 4.8).

The FE model predicted a slightly higher force (P^{∞}_{FE}) than the experimental force at equilibrium (P^{∞}_{exp}) at the end of the hold period with the equilibrium modulus, as given by Eq. (4.5) (E^{∞}_{th}). This meant that for the experiments, true equilibrium would be reached for a value of equilibrium modulus slightly less than E^{∞}_{th}. To determine the sensitivity of the VE parameters to the E^{∞} used in the FE model, the experimental data from the 15 μm indenter were fitted with values of E^{∞} fixed to $85-100\%$ of E^{∞}_{th}, i.e., for values of α between 0.85 and 1.0. The results (Table 4.3) showed that the curve fits had an $R^2 > 0.9$ only for values of α for which $\alpha \leq P^{\infty}_{\text{exp}}/P^{\infty}_{\text{FE}}$ and for these curves, there was only a very slight variation in the parameters g_1 and τ_1. Therefore, the parameters g_1 and τ_1 were fixed at average values for the curve fits with $R^2 > 0.9$, and the parameters g_3, τ_3, and E^{∞} were extracted. The extracted $E^{\infty} = 0.9E^{\infty}_{th}$, justifying the use of $\alpha = 0.9$ in Step 1.

As with any model used to fit experimental data in order to identify model parameter values, there is the concern with uniqueness of fit, and the larger the number of fitting parameters, the greater the concern. In the present case, the primary concern is with the four VE parameters. Note that there are two distinct response regions in the experimental data, a very rapid response with a time constant in seconds and a much longer response with a time constant nearer 100 s. Accordingly, this is reflected in the insensitivity of g_1 and τ_1 to starting point in the fitting routine and to the equilibrium load values. The longer time constant is accordingly insensitive

to the shorter time data but sensitive to the long time data and the equilibrium load values. Thus, although four parameters are fitted from one data set, the region fitted by each of the two time constants is relatively unique, so the question of uniqueness is not so much a concern. However, the use of three different starting points showed that there is still some uncertainty in the fit parameters. A rigorous sensitivity analysis for a particular experiment and fitting process should be done in order to estimate error bounds on predicted parameters.

The values we predicted for our PE parameters in our PVE model were in the range of those reported by Cao *et al.* [33] for indentation of mouse cartilage with a 110 μm flat-ended cylindrical indenter. There were differences, but whether this was due to the assumed model or true material properties of the differing mice is unknown. Our mice were young, one month old; their mice were six months old. However, there are likely significant differences in predicted properties. When we assumed a PE model, the predicted permeability using our data was smaller (0.39×10^{-15} m^4/N-s for PE versus 2.11×10^{-15} m^4/N-s for PVE) and Poissons ratio was slightly larger (0.23 for PE versus 0.20 for PVE) for the PE model. E^{∞} was approximately the same. This agrees with the intuition that decreasing κ should increase fluid flow effect and increasing ν should decrease fluid flow effect. There should be less fluid flow effect in the PVE model, since the viscoelasticity would account for part of the time dependency. Based on our results, it would be expected that the tests of Cao *et al.* [33] would stimulate the VE effect. There would also be a PE response, but be relatively short lived, of the order of 10 s (Fig. 4.7). The longer creep and relaxation would be due to the VE response.

The relative importance of PE and VE effects is a fundamental issue in cartilage testing. As shown from the present work and Huang *et al.* [73], this relative

importance depends on test configuration and loading rates. In conventional millimeter sized test specimens, the PE effect is the longer response, with the VE effect mainly affecting the short term response [27]. For the smaller specimens and tip geometries, however, at our loading rates the PE effect is minimal and the VE effect dominates. It would seem that this relative effect and the necessity of including both effects in a model of cartilage should be checked to justify a particular model, particularly if loading time includes the functional range of the order of 1 s. One of the main uses of fit model parameters is to aid in understanding the microstructural basis of macroscopic mechanical response. It is desired to identify the mechanical function of microscopic processes and molecules. Assuming a PVE model implies that both flow-dependent and flow-independent processes occur in the experimental tissue. The ability to separate these two processes, both experimentally and theoretically, makes the two indenter approach much more useful. The limitation of assuming a solely PE model is that all time dependent processes are assumed to be flow dependent. If this is wrong, as would be the case with our 15 μm indenter, then interpretation of results with respect to microscopic processes would be wrong. The model assumption subsumes an assumption of the underlying physics of the problem.

For extracting the VE parameters from Step 1, we assumed $\nu^\infty = 0.25$, whereas the extracted value from Step 2 was $\nu^\infty = 0.20$. We examined the effect of this difference on the effect of the VE fit and found that g_1, g_3, and τ_1 did not change; τ_3 changed by a factor of 25%, within the range of changing the starting point (Table 4.2).

We noted in exploring the effect of α and ν^∞ that as long as $P^\infty_{\mathrm{FE}} = P^\infty_{\mathrm{exp}}$, the viscoelastic parameters were not sensitive to either ν^∞ or E^∞. However, this meant that in order to satisfy this condition, if we changed E^∞ we would have to change

ν^{∞} to achieve this.

The equilibrium elastic modulus measured by the 15 μm indenter (4.2 MPa) was higher than that measured by the 170 μm indenter (0.77 MPa). This was the case for both the FE model and by the modified analysis of Hayes *et al.* [103] using the experimental data. We have documented this phenomenon in bovine cartilage [19] but do not know the source of the size effect. We speculate that it may be due to the inhomogeneity near the surface and the different volumes probed by different sized tips at fixed indentation depths. In our prior work with bovine cartilage, 5 μm and 90 μm tips did not show a relative size effect, but 5 μm and 190 μm tips did. Thus the observed effect here for mouse cartilage for the 15 μm and 170 μm tips is consistent with the bovine experiments. As with the bovine tests, we speculate that the size effect in the mouse is due to the inhomogeneity near the surface and the different depths probed by the different tips. The different layer thicknesses and dimensions of inhomogeneity between the mouse and the bovine cartilage may account for the effect of the differences in absolute tip size between the mouse and the bovine cartilage. Another possible cause of the difference in equilibrium modulus between the tips is that the 170 μm tip may not have been in complete contact due to the curvature of the surface. From prior work, we have profiles of mouse tibia. We compared these with the 170 μm length and concluded that if the tip were away from the region of smallest radius of curvature, which we tried to achieve, there should be no problem. However, if the tip were at the site of largest curvature, there could be a problem of incomplete contact, which would show up as apparent lower modulus. We went back and examined our data where multiple indents and various locations along the profile were performed and saw no consistent pattern, i.e., no single high modulus at the center and lower modulus away from the center. Also, we used the first step as a preload and the second for fitting the parameters,

so misfit would be minimized. As far as we can tell, we are getting complete contact with the 170 μm tip. Another possible cause is that the second step of the load protocol was used, assuming the starting point of that step as the unloaded state. For the 170 μm tip, this should not be a problem because it behaves as a flat-ended cylinder for approximately 80 μm displacement. For the 15 μm tip, however, the start of the second step could be into the conical contact region, resulting in higher loads and consequent higher apparent elastic modulus. We examined the data used for this effect and the results are inconclusive. This issue should be considered and care taken into account for when using our method with conical tips.

An assumption in our method is that the VE response and associated parameters are the same for the 15 μm indenter as for the 170 μm indenter. This is similar to the assumption of Huang *et al.* [73] who assumed that the VE response of the thin strip in tension and a larger specimen in compression are the same. As with the equilibrium modulus, it is conceivable that the VE response is also different between the two indenters. This will have to be assessed with further studies, but assuming a single VE model for both indenter tips appears a reasonable first step consistent with current knowledge.

Part III

Mesoscale Modeling of AC

Chapter 5

Fibril-reinforced models for articular cartilage

5.1 Overview

In Chapter 2 we briefly discussed the structure and composition of AC and some of its important mechanical properties. Some of the prevalent continuum based models to predict AC mechanical behavior were discussed in Chapter 3. However, AC has a complex structure and is highly anisotropic. It also has different properties in tension and compression. A common method to address this observed tension-compression nonlinearity of AC is by using fibril-reinforced models. This has been introduced earlier in Sec. 3.4.3. In this chapter this discussion is continued and some of the important fibril-reinforced models are reviewed.

5.2 Spring fibril-reinforced models

As discussed in Chapter 3 there are two types of fibril-reinforced models seen in the literature: spring models and continuum models. In the spring models, springs are

placed between the nodes of the elements to represent the fibrils. This means that fibrils can be represented only in the direction of the elements. One of the first spring fibril-reinforced model was by Soulhat *et al.* [80] which formally presents an elastic collagen fibrillar network which resists tension only, reinforcing an isotropic biphasic component representing PGs and water. A linear formulation was proposed and the corresponding analytical solution was found for uniaxial unconfined compression. The solid stress of the fibril-reinforced material is given by the sum of the matrix and fibril stresses [80], as

$$\boldsymbol{\sigma}_E = \boldsymbol{\sigma}_m + \boldsymbol{\sigma}_f \tag{5.1}$$

where $\boldsymbol{\sigma}_m$ and $\boldsymbol{\sigma}_f$ are the stresses in the non-fibrillar matrix and the collagen fibrils, respectively. This model is described by two drained matrix elastic coefficients (E_m and ν_m), an equivalent Young's modulus E_f of the fibril network, and hydraulic permeability, k.

Li *et al.* [81–83] further developed the model by Soulhat *et al.* to include nonlinear features. In their earlier models [81, 82] the stiffness of the collagen fibrils was represented by a linear spring with stiffness E_0, parallel to a nonlinear spring with stiffness $E_1 = E_\varepsilon \varepsilon_f$ as shown in Fig. 5.1a, where ε_f is the strain in the fibril direction. For these models, the fibril stress was thus given by

$$\sigma_f = \begin{cases} (E_0 + E_\varepsilon \varepsilon_f)\, \varepsilon_f & \text{for} \quad \varepsilon_f \geq 0, \\ 0 & \text{for} \quad \varepsilon_f < 0. \end{cases} \tag{5.2}$$

In later models [83] the fibrils were assumed to be viscoelastic which changed the fibril stresses to

$$\sigma_f = \sigma_0(0) + \int_0^t G(t-\tau) E_f(\varepsilon_f) \dot{\varepsilon}_f \, \mathrm{d}\tau, \tag{5.3}$$

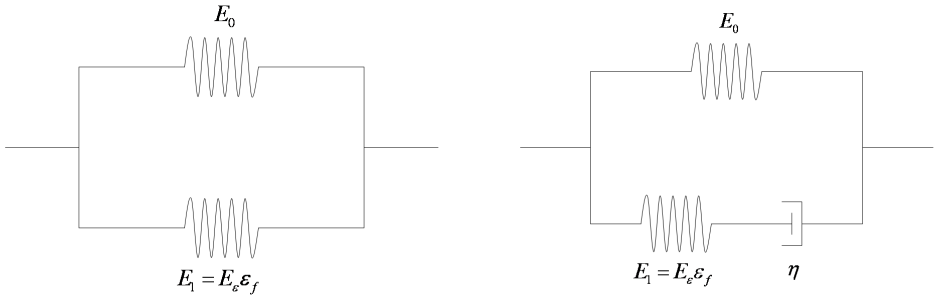

(a) Elastic fibrils (b) Viscoelastic fibrils

Figure 5.1: Schematics for elastic and viscoelastic collagen fibril are shown.

where G(t) is the relaxation function represented by a discrete spectrum approximation as

$$G(t) = 1 + \sum_{M} \mathrm{g_m} \exp(-\frac{t}{\tau_m}), \tag{5.4}$$

where τ_m are the characteristic times for viscoelastic dissipation.

5.3 Continuum fibril-reinforced models

In the continuum fibril reinforced models, the fibril orientation is independent of the finite element mesh. This enables a representation of a geometrically realistic network as fibrils can run in any direction. Several continuum models exist, e.g., [86–89], which include some kind of homogenization technique to evaluate the structural properties of articular cartilage from the microstructure. These models differ in the computation of the stress matrix depending on the assumptions and model formulation.

The micro-structural model by Schwartz *et al.* [86] is based on methods that have been developed for fiber-reinforced composites. In this model, articular cartilage is modeled as a spatial distribution of two components, fibers and matrix. The fibers

simulate the collagen fibril network, the matrix simulates the PG-water gel. The fibers are represented by a bilinear isotropic elastic material which is taken to be stiff in tension and very weak in compression, thus capturing the slender, flexible, cable-like nature of collagen fibers. The stress-strain response of the collagenous component of the microstructure can be characterized by a taut and a slack Young's modulus (E_f^+ and E_f^- respectively) and a constant Poisson's ratio (ν_f) as

$$\boldsymbol{\sigma}_f = \frac{E_f \nu_f}{(1+\nu_f)(1-2\nu_f)} \mathrm{tr}(\boldsymbol{\varepsilon})\mathbf{I} + \frac{E_f}{(1+\nu_f)}\boldsymbol{\varepsilon}, \tag{5.5}$$

where

$$E_f = \begin{cases} E_f^+ & \text{(tension)} \\ E_f^- & \text{(compression)} \end{cases},$$

and $E_f^+ \gg E_f^-$. The matrix is modeled as a linear elastic isotropic material, where

$$\boldsymbol{\sigma}_m = (K_m - \frac{2}{3}\mu_m)\mathrm{tr}(\boldsymbol{\varepsilon})\mathbf{I} + 2\mu_m\boldsymbol{\varepsilon}. \tag{5.6}$$

The values for the material constants are chosen in accordance with available experimental data from literature. Next, a basic structural unit (BSU) of the tissue's microstructure is defined. The BSU is a cylinder of collagen (a fiber) surrounded by an annulus of matrix material as shown in Fig. 5.2. The relative radii of these components are dictated by the collagen fiber diameter and the appropriate volumetric ratio of fiber to matrix (volume fraction). The BSU is assumed to be the basic elastic energy storage unit in the microstructure. The tissue is idealized to be a spatial distribution of such composite cylinders. Due to obvious symmetry along the axis of the fiber, the elastic response of the BSU is transversely isotropic, and so may be characterized by five independent elastic constants: E_{11}, the stiffness of the BSU in uniaxial extension, ν_{12} the lateral contraction (Poisson's) ratio in uniaxial extension, K_{23} the bulk modulus in transverse plain strain, μ_{12} the shear modulus

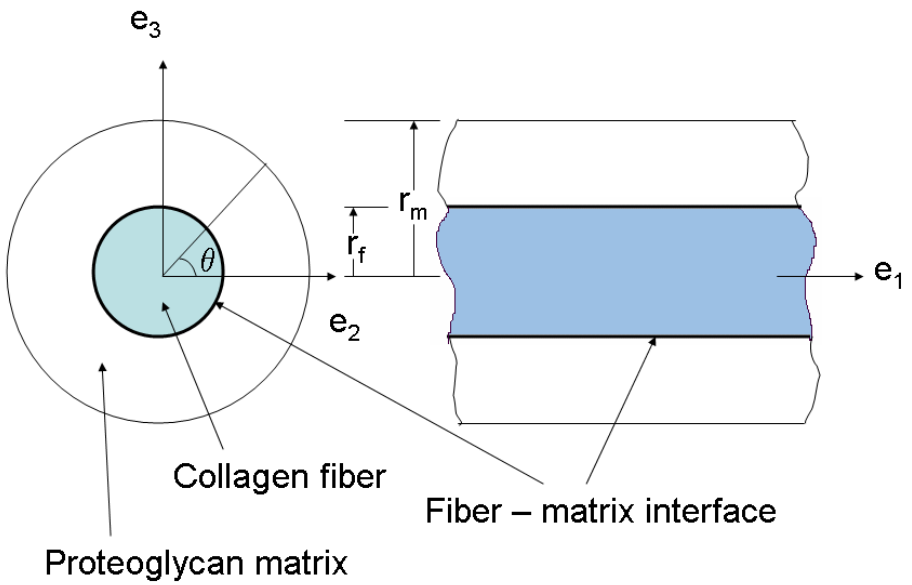

Figure 5.2: The basic structural unit (BSU) of the Schwartz *et al.* model [86]. The inner cylinder represents a type II collagen fiber, the outer annulus represents the hydrated PG aggregate. The two phases are connected by an elastic interface sensitive to shear deformations.

in the longitudinal plane and μ_{23} the shear modulus in the transverse plane. A possibility of an imperfect bond at the boundary of the two phases is also included by imposing that the jump in tangential displacement across the fiber-matrix interface is proportional to the tangential traction on this surface,

$$u_{\mathrm{m}}^{\tan} - u_{\mathrm{f}}^{\tan} = \mathbf{R} t^{\tan}, \tag{5.7}$$

where the variable $\mathbf{R}$ is the interface compliance, $u^{\tan}$ is the tangential component of displacement and $t^{\tan}$ is the shearing component of the traction vector. In the calculation of E_{11}, ν_{12} and K_{23}, the interface condition, Eq. (5.7), does not come into play due to the radial symmetry of the BSU. As a result, the commonly accepted expressions for these constants may be used (Christensen, 1979) [104].

The analysis of the transverse and longitudinal shear moduli is performed explicitly because of the existence of tangential displacements at the fiber-matrix interface. This is done by employing the concept of equivalent homogeneity to get the effective modulus [104]. This assumes that there is a solid cylinder of radius r_{m}, composed of an 'effective homogeneous' material, which is equivalent to the heterogeneous composite, and is subjected to the same boundary conditions as the composite cylinder (BSU). To solve for the effective shear modulus, μ_{12}, of the BSU, the energy stored in the two cylinders is equated. This takes the general form

$$\int_{\mathrm{Cyl}_{\mathrm{r_m}}} \mathbf{C}_{ijkl}^{\mathrm{BSU}} \boldsymbol{\varepsilon}_{kl} \boldsymbol{\varepsilon}_{ij} \,\mathrm{d}v + \oint_{r_f} t^{\tan}(u_{\mathrm{m}}^{\tan} - u_{\mathrm{f}}^{\tan}) \,\mathrm{d}s = \int_{\mathrm{Cyl}_{\mathrm{r_m}}} \mathbf{C}_{ijkl}^{\mathrm{eff}} \boldsymbol{\varepsilon}_{kl} \boldsymbol{\varepsilon}_{ij} \,\mathrm{d}v, \tag{5.8}$$

where $\mathbf{C}^{\mathrm{eff}}$ is the effective stiffness tensor, $\mathrm{Cyl}_{\mathrm{r_m}}$ denotes a cylinder of radius r_{m} and

$$\mathbf{C}^{\mathrm{BSU}} = \begin{cases} \mathbf{C}^{\mathrm{fiber}} & (0 < r < r_f), \\ \mathbf{C}^{\mathrm{matrix}} & (0 < r < r_f) \end{cases} \tag{5.9}$$

To address the distributed nature of the fibrous microstructure of the tissue, and the ability of these fibers to reorganize under deformation, an orientation averaging procedure which relates the properties of the homogenized BSU to the macroscopic constitutive equation at a point is used. Only planar fiber distributions in the global $x-y$ plane are considered. The fiber distribution function $f(\psi)$ is defined to be the density of fibers which are oriented in the $\hat{\mathbf{e}}_\psi$ direction, where

$$\hat{\mathbf{e}}_\psi = \cos\psi\hat{\mathbf{i}} + \sin\psi\hat{\mathbf{j}}$$

Because the fibers are assumed to be straight, $f(\psi) = f(\pi+\psi)$. $f(\psi)$ is normalized by setting

$$\oint_{C_1} f(\psi)\,\mathrm{d}S = \int_0^{2\pi} f(\psi)\,\mathrm{d}\psi = 1.0 \tag{5.10}$$

where C_1 is taken to be the unit circle.

The five effective material constants calculated earlier define the stiffness tensor for a given BSU. Using the fiber density function to account for the distribution of such elements, an effective stiffness for the composite at a point can be calculated by orientation averaging [105]. The effective composite stiffness, $\mathbf{C}^{\text{eff}}_{\text{comp}}$, is defined as the spatial average of directional properties, weighted by the fiber distribution function

$$\mathbf{C}^{\text{eff}}_{\text{comp}} = \int_0^{2\pi} f(\psi)(Q^\psi_{ri}Q^\psi_{sj}C^{\psi_{\text{loc}}}_{rstu}Q^\psi_{tk}Q^\psi_{ul})\,\mathrm{d}\psi, \tag{5.11}$$

where $\mathbf{Q}^\psi$ is the matrix of direction cosines, and $\mathbf{C}^{\text{eff}}_{\text{comp}}$ is the effective composite stiffness tensor in the global coordinate system. A material point subjected to a prescribed deformation, $\boldsymbol{\chi}$, will result in redistribution of fibers such that the image of the distribution function $f(\psi)$ under the deformation is

$$g(\phi) = f(\psi)\frac{\mathrm{d}S}{\mathrm{d}s} \qquad [\psi = \psi(\boldsymbol{\chi}, \phi)]. \tag{5.12}$$

The swelling effect of articular cartilage is included in the model in the form of a initial fiber pre-strain which can be thought of simply as a pre-existing deformation of the fiber, before any external loads or deformations are specified. This pre-stretched equilibrium state is taken to be the reference configuration for subsequent deformation.

This model is able to offer mechanistic explanations for the tensile nonlinearity of AC and the reduction in stiffness due to matrix degradation. It also explains the effect of this degradation on the swelling properties of the tissue. This is one of the few models that addresses the fiber-matrix interaction and suggests its mechanical role to be important in the shear properties of the tissue.

In the models of Wilson *et al.* [87,90,91] the collagen fibril network is modeled as a combination of large primary and smaller secondary collagen fibrils. Bundles of primary fibrils extend perpendicular from the subchondral bone and split up close to the articular surface, in four different fibril directions, into fibrils which curve to a horizontal course, flush with the articular surface. The collagen fibrils are assumed to be viscoelastic and are represented by a linear spring with stiffness E_0, parallel to a nonlinear spring with stiffness E_1 in series with a linear dashpot with damping constant η as shown in Fig. 5.1b. The fibrils are assumed to resist only in tension and the stresses in the viscoelastic fibrils are given by

$$\begin{aligned} &\sigma_f = -\frac{\eta}{2\sqrt{(\sigma_f - E_0\varepsilon_f)E_\varepsilon}}\dot{\sigma}_f + E_0\varepsilon_f + \left(\eta + \frac{\eta E_0}{2\sqrt{(\sigma_f - E_0\varepsilon_f)E_\varepsilon}}\right)\dot{\varepsilon}_f \quad \text{for} \quad \varepsilon_f > 0 \\ &\sigma_f = 0 \qquad\qquad\qquad\qquad\qquad\qquad\qquad\qquad\qquad\qquad\qquad\qquad\quad \text{for} \quad \varepsilon_f \leq 0 \end{aligned} \tag{5.13}$$

The non-fibrillar part of the solid matrix is assumed to be linear elastic, with a Young's modulus E_m and Poisson's ratio ν_m. The permeability, k is assumed to be

strain dependent and given by Eq. (3.8). The solid stress in this model is given by

$$\boldsymbol{\sigma}_E = \boldsymbol{\sigma}_m + \sum_{i=1}^{\text{tot}\, f} \sigma_{f,i} \vec{v}_{new,i} \otimes \vec{v}_{new,i}, \tag{5.14}$$

where $\sigma_{f,i}$ are fibril stresses in the ith fibril and $\vec{v}_{new,i}$ the current fibril direction of the ith fibril, and the sum is $\boldsymbol{\sigma_f}$. The unknown material properties are determined by fitting them to unconfined compression and indentation measurements of DiSilvestro and Suh (2001) [27] simultaneously. Wilson *et al.* later extended their fibril-reinforced poroviscoelastic finite element model [87] with their biphasic swelling model [77] to include the swelling properties due to the FCDs of the PGs [90].

Federico *et al.* [88] used a homogenization procedure for transversely isotropic composites with spheroidal inclusions [92]. They derive a transversely isotropic transversely homogeneous (TITH) model in which every possible fiber direction is taken into account. The model also incorporated the continuous variation of the elastic modulus of cartilage as a function of depth. The solid phase of articular cartilage is seen as a composite material made by three phases: a PG matrix and two inclusion phases represented by the chondrocytes and the collagen fibers. A global reference frame is defined to represent the properties of transverse isotropy and transverse homogeneity and a class of local reference frames is used to represent every single fiber in the fiber phase. In the global reference frame, the volumetric concentration and the arrangement of the inclusion phases (collagen fiber phase and chondrocyte phase) are assumed to vary continuously along the depth direction and remain constant in the transverse plane, parallel to the articular surface and the tide mark. The global elastic tensor of a $(N+1)$-phasic composite, with an isotropic matrix (index 0), $N-1$ spheroidal inclusion phases aligned with the e_1 direction,

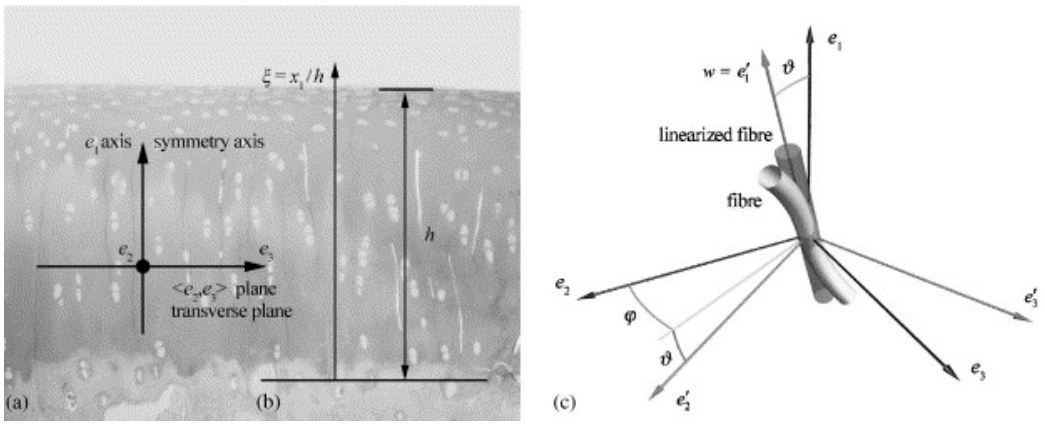

Figure 5.3: Micrograph of chondrocytes in articular cartilage, symmetry axis and transverse plane for the TI model of Federico *et al.* [88] (a), the non-dimensional cartilage depth, ξ (b), and the local reference frame for collagen fibers (c). (figure from [88] based on photomicrograph from Clark *et al.* 2003 [106]).

which is the global symmetry axis (Fig. 5.3), and one inclusion phase (N) with statistical orientation, is given by the following fourth order tensor expression:

$$L = \left[\sum_{r=0}^{N-1} c_r Z_r + \int_{\mathbb{S}^{2+}} \phi c_N Z_N \, \mathrm{d}a\right] \cdot \left[\sum_{r=0}^{N-1} c_r A_r + \int_{\mathbb{S}^{2+}} \phi c_N A_N \, \mathrm{d}a\right]^{-1} \tag{5.15}$$

For each phase r, c_r is the volumetric fraction, $Z_r = L_r A_r$, where L_r is the elasticity tensor and A_r the strain concentration tensor which depends on the aspect ratio of the inclusion:

$$\alpha_r = a_r / b_r \tag{5.16}$$

Here a_r and b_r are the longitudinal and transverse semi-axes, respectively. By adjusting a_r and b_r, different inclusions shapes can be used to represent chondrocytes and fibers. A chondrocyte inclusion is represented as an ellipsoidal inclusion, whereas a rectilinear fiber inclusion is represented as an inclusion for which the aspect ratio, α_r, tends to infinity. The two integrals in Eq. 5.15 are the directional averages of tensors Z_N and A_N over all directions in space (represented by the northern unit hemisphere $\mathbb{S}^{2+}$). Function ϕ is a normalized probability distribution

density function of fiber distribution. Federico *et al.* [107] prove that Eq. (5.15) can be written as:

$$L = \left[\sum_{r=0}^{N-1} c_r Z_r + c_N \bar{Z}_N^{\alpha} H_{\alpha}\right] \cdot \left[\sum_{r=0}^{N-1} c_r A_r + c_N \bar{A}_N^{\alpha} H_{\alpha}\right]^{-1} \tag{5.17}$$

where $\bar{Z}_N^{\alpha}$ and $\bar{A}_N^{\alpha}$ are Walpole's components [108] of tensors Z_N and A_N, with respect to the transversely isotropic tensor basis $B = \{B_{\alpha}\}_{\alpha=1}^{6}$, and tensors H_{α} are the directional averages of the basis tensors B:

$$H_{\alpha} = \int_{\mathbb{S}^{2+}} \phi B_{\alpha} \, \mathrm{d}a. \tag{5.18}$$

The fluid phase is included with the help of depth-dependent permeability, and is assumed to obey Darcy's law.

Garcia *et al.* (2007) [89] proposed a biphasic viscohyperelastic fiber-reinforced model for AC. AC is considered as a biphasic material with its solid component formed of two phases. Both solid phases are represented by the viscohyperelastic law described by Garcia and Cortés (2006) [74], but differ in the hyperelastic function used. The fibers are assumed to resist only in tension. Briefly, the differential form of the viscohyperelastic law [74] is described as:

$$\mathbf{S} + t_1 \dot{\mathbf{S}} = \mathbf{C}^{(\mathbf{SE})} : \mathbf{E} + t_1(1+\beta)\mathbf{C}^{(\mathbf{SE})} : \dot{\mathbf{E}}, \tag{5.19}$$

where $\mathbf{S}$ is the second Piola stress tensor, $\mathbf{E}$ the Lagrange strain tensor, $\mathbf{C}^{\mathbf{SE}}$ the second elasticity tensor [109] and t_1 and β_1 are the model parameters which describe the viscous properties of each solid phase. To describe the deformation at equilibrium, when pore pressure is zero and the viscous effects of the solid phase have disappeared, the following hyperelastic function by Holmes and Mow (1990) [110] is

considered

$$\varphi = \alpha_0 \frac{\exp[\alpha_1(I_1 - 3) + \alpha_2(I_2 - 3)}{I_3^n} - \alpha_0, \tag{5.20}$$

where I_1, I_2 and $I - 3$ are the invariants of the right Green deformation tensor $\mathbf{B}$, and α_0, α_1, α_2 and n are elastic coefficients. For the fibrils the following hyperelastic function proposed by Limbert and Middleton (2004) [111] is considered:

$$\varphi_f = \frac{E_{f0}}{8\gamma}[\exp(\gamma((\lambda^2 - 1)^2) - 1] \tag{5.21}$$

where E_{f0} is the Young's modulus at zero deformation, γ can be used to adjust the form of the stress-strain curve under tension and λ is the stretch ratio. The equilibrium Cauchy stress in the fibers is calculated as

$$\sigma_\alpha = \frac{E_{f0}}{2}\lambda^2(\lambda^2 - 1)\exp(\gamma(\lambda^2 - 1)^2) \tag{5.22}$$

For the fibrils, Eq. 5.19 takes the form

$$\boldsymbol{\sigma_\alpha} + t_1\dot{\boldsymbol{\sigma}}_{\boldsymbol{\alpha}} = f(\lambda) + t_1(1 + \beta)\dot{f}(\lambda) \tag{5.23}$$

where $\dot{\boldsymbol{\sigma}}_{\boldsymbol{\alpha}}$ is the material derivative of the Cauchy stress in the fibers, $f(\lambda)$ is a function of the stretch ratio λ, equal to the right term of Eq. 5.22.

This model was fit to experimental finite-deformation equilibrium curves reported by Huang *et al.* (2005) [10] in human humeral cartilage under unconfined tension and confined compression in directions parallel and perpendicular to the surface, respectively. It was also used to fit reaction force and lateral displacement curves reported by DiSilvestro and Suh (2001) [27] for bovine patella in unconfined tests.

5.4 Discussion

The ECM of AC can be considered as a fiber-reinforced composite solid consisting of a dense stable network of collagen fibers embedded in a nonfibrillar matrix. AC is inhomogeneous and anisotropic: its structure and composition vary throughout its depth. The use of fibril-reinforced models for predicting AC mechanical behavior provides various advantages over non-fibril-reinforced models. Including fibrils addresses the anisotropy of the solid matrix (ECM). Also, in the fibril-reinforced models, the fibrils resist only in tension. This provides a more accurate representation of the fibril behavior in the tissue. Wilson *et al.* [30] have concluded that the local stresses and strains in AC are highly influenced by the local morphology of the collagen fibril network and that to predict cartilage damage and adaptation the specialized collagen fibril network morphology must be considered. Inroduction of fibrils also allows inclusion of nonlinear properties of fibrils as well as more realistic orientations of fibrils. It also helps relate observed mechanical behavior to the microstructure establishing structure-function relationships.

The models reviewed here, and other similar models all aim to relate AC microstructure to its mechanical behavior. The spring-based fibril-reinforced models of AC developed by Soulhat *et al.* and Li *et al.* (e.g., [80–83]) have aided in understanding the role of the collagen network in time-dependent response of AC. Korhonen *et al.* [112] have studied the influence of depleting PGs and degenerating collagen on AC behavior using spring-based fibril-reinforced models. The microstructural model of Schwartz *et al.* [86] offers mechanistic explanations for the tensile nonlinearity of AC and stiffness reduction and its effect on tissue swelling due to matrix degradation. Fibril-reinforced models of Wilson *et al.* [87, 90, 91, 113] have been useful in understanding the depth-dependent compressive equilibrium properties of AC, stresses in the local collagen network and compositional changes during cartilage

damage and adaptation. The TITH fibril-reinforced model developed by Federico *et al.* [88, 92] has been used by Han *et al.* [114] to predict the mechanical behavior of chondrocytes in indentation and unconfined compression. The hyperelastic models of Garcia *et al.* [74, 89] have incorporated nonlinear constitutive behaviors for individual AC components to produce a more realistic simulation and prediction of AC mechanical response.

All of the mathematical models of AC have been designed to deduce macroscopic constitutive relations, with varying degrees of incorporating some details of the microstructure. Consequently, the assumptions of details of the microstructure have been highly idealized. It would not be possible, for example, to include the details of the hypothesized microstructural composition and organization of Fig. 2.1. As such, the microstructure cannot be related to the macroscopic response with any degree of confidence. A goal of this part of the thesis is to evaluate the effects of specific crosslinks between collagen fibrils, as shown schematically in Fig. 2.1. In order to do this, a more realistic simulation of cartilage microstructure is needed. The idea is to develop a mesostructural model of AC matrix that includes IFLs modeled as simple linear springs. In the following chapters, the development and parametric study of such a mesomodel is discussed in detail.

Chapter 6

Mesoscale Model Development

In this chapter, the development of the finite element mesoscale model that includes major AC micro-constituents - collagen fibrils, extrafibrillar proteoglycan matrix and interfibrillar cross-links - is discussed. A modeling strategy is developed that captures the desired mechanical behavior of each model component as well as the overall model in the simplest constitutive model. The modeling details of each individual component are described. This is followed by a procedure to determine the smallest size of the finite element model that gives the same average mechanical properties for a given simulated mechanical test as any larger model. Choice of appropriate boundary conditions will depend on the intended use of the model – as a representative volume element (RVE), or as a specimen in a simulated test.

6.1 Model Components

In this section, the desired mechanical properties of each major component of the model – collagen fibrils, the extrafibrillar matrix (EFM) (mainly PGs) and the interfibrillar cross-links (IFLs) – are discussed. The fibrils are modeled using 3D line elements that share nodes with the EFM elements. This eliminates the need to separately account for fibril-EFM interactions. This is followed by a detailed discussion of how the components are modeled in the commercial FEA software package ABAQUS. All development and analysis of the mesoscale model was carried out using ABAQUS version 6.9-1. Recall from Chapter 1 that ABAQUS is widely used in the field of cartilage research to understand cartilage mechanics and in establishing structure-function relations in cartilage growth, damage and degeneration, especially in the context of osteoarthritis. Also, ABAQUS has an extensive library of structural line elements such as truss, beams and frames that can be used for a range of structural problems.

6.1.1 Collagen Fibrils

The collagen fibrils of soft tissues show a characteristic rope-like structure [115] and behavior, resisting in axial tension while slacking or offering low contribution in axial compression. Along the axial direction, the elastic modulus measured from experiments has been reported in a wide range ($\sim$ 100 MPa - $>$ 1 GPa) depending upon whether the measurement was under in-air or *in vitro* tensile testing [116–118]. The fibrils are slender and buckle easily when compressed [119]. It is the specialized structure of the collagen fibril network - from the level of the tropocollagen molecule to the organization of these molecules into the macroscopic fibrils, fibers and fascicles - that is believed to impart the tissue its mechanical properties. Thus, the desired fibril mechanical properties in the model are: high elastic modulus in the axial

direction and easy bending under axial compression.

The diameter of the collagen fibrils not only varies from tissue to tissue, but also within a tissue. For cartilage, tendon, skin, cornea, etc., the fibril diameter has been reported to be in a wide range of $2 - 1400$ nm [120–126]. Compared to the typical dimension along the axis, i.e., the length of the fibril, which is of the order of several μm, the cross-section dimensions are small and thus slenderness assumptions hold for the fibrils. This suggests using 3-D line elements in ABAQUS, such as beam elements which are based on beam theory – a one-dimensional approximation of a three-dimensional continuum.

There is also the challenge of modeling the bilinear rope-like behavior of the fibrils as correctly as possible. Bozec *et al.* [115] have suggested that modeling collagen fibrils as ropes will provide a more accurate representation of fibril forming collagenous tissues. In this study we have assumed a homogenous rod-shaped structure for the collagen fibrils, and we attempted to capture the rope-like behaviour by using a combination of truss and beam elements with different elastic moduli for modeling the collagen fibrils in ABAQUS.

Each fibril in the model geometry (Sec. 6.3) is modeled using 3D truss elements (T3D2). In ABAQUS, it is possible to set certain elements as non-tensile or non-compressive, so that they do not carry any load in tension or compression respectively. This property was utilized in the current model. The fibril truss elements were set to be non-compressive with their elastic modulus set to the high tensile modulus E_{f}^{+} reported for collagen fibrils from literature. The truss elements, thus, account for almost the entire tensile behavior of the collagen fibrils.

In order to model the very low resistance and easy buckling offered in axial compression, *pseudo-fibrils* were introduced. Each truss fibril element was accompanied by a beam pseudo-fibril element that occupied the same nodes as the truss fibril

element and were modeled as beam elements. This imparted bending ability to the fibrils along with an additional low axial stiffness in tension and compression. The stiffness of these fibril beam elements is set to the low compressive stiffness E_{f}^{-} ($E_{\mathrm{f}}^{+} \gg E_{\mathrm{f}}^{-}$) as used by Schwartz *et al.* [86]. This has the added advantage that the low stiffness translates into low section modulus and consequently low bending stiffness of the fibrils as desired. Linear two node beam elements (B31) in 3D are used for the pseudo-fibrils.

6.1.2 Extrafibrillar Matrix

The EFM is regarded as a highly viscous gel composed mostly of PGs. The PGs (mainly aggrecan) are responsible for the osmotic swelling and the elastic properties of the tissue. The EFM plays a very important mechanical role when cartilage is loaded in compression during which fluid exudation from the tissue and fluid redistribution within the tissue result in time-dependent viscoelastic behaviors accompanied by volumetric changes [24, 127, 128]. These processes contribute greatly to the load distribution in the tissue [24] and recovery of the tissue after removal of load [24, 128, 129]. During interstitial fluid flow high fluid pressures are produced due to the low hydraulic permeability of the matrix. The stresses and strains on the solid matrix phase (including the collagen fibrils) during normal joint loading are reduced as a result of the interstitial fluid flow and the resulting fluid pressurization and energy dissipation. Thus, the low permeability of the tissue is a very important mechanical property. The hydraulic permeability is related to the pore structure in the solid phase, saturation of these pores by water and the PG concentration [24, 39, 123, 127, 130–132].

Different FE models have used different types of elastic constitutive behavior for the EFM. These include different symmetries (isotropy, orthotropy, transverse isotropy, etc.), linear or non-linear or conewise-linear, etc. These have been reviewed

in detail in Chapters 3 and 5. The elastic modulus of the EFM, E_{m}, is very low compared to the tensile modulus of the collagen fibrils. In this study, a linear elastic constitutive behavior is assumed for an isotropic EFM for simplicity.

In our mesomodel, the intrinsic viscoelasticity of the solid phase of the tissue is neglected. It is assumed that the time-dependent behavior is completely explained by the fluid flow-dependent properties. In ABAQUS, the EFM is modeled as a poroelastic material with 3D continuum coupled pore-pressure and stress elements (C3D8RP). For simplicity, the porous skeleton of the matrix material is assumed to be linear elastic and incompressible. It is assumed that the fluid flow through the matrix is fully saturated – the interstitial water completely fills up the pores of the matrix. ABAQUS adopts an effective stress principle to describe the constitutive behavior of the porous medium. For a fully saturated flow, the effective stress principle is written as

$$\boldsymbol{\sigma}^{E} = \boldsymbol{\sigma}^{\mathrm{porous}} + p\boldsymbol{I} \tag{6.1}$$

where $\boldsymbol{\sigma}^{\mathrm{porous}}$ is the stress in the porous material. The porosity of the medium, $\acute{n}$ is the ratio of the volume of voids to the total volume:

$$\acute{n} = \frac{dV_v}{dV} \tag{6.2}$$

The void ratio e, i.e. ratio of fluid to solid can be expressed in terms of the porosity ($\acute{n}$) as

$$e = \frac{\acute{n}}{1 - \acute{n}} \tag{6.3}$$

In ABAQUS, the constitutive behavior for pore fluid flow is governed either by Darcy's law or by Forchheimer's law. Darcy's law is generally applicable to low fluid flow velocities, as is the case in soft tissue models, whereas Forchheimer's law is commonly used for higher flow velocities.

6.1.3 Interfibrillar Cross-links

The exact mechanical nature of the interfibrillar cross-links is unknown. It has been hypothesized that such cross-links exist and it is assumed that these types of cross-links are purely molecular in nature. Several studies have proposed such molecules and specific binding mechanisms have been identified, e.g., type IX collagen by Eyre *et al.* [52, 53], matrilin-3 by Budde *et al.* [54], etc. Recently, Parsons *et al.* [56] were able to confirm an interaction between type IX collagen and fibronectin, a molecule that is one of the many molecules forming the EFM. Another such molecule via which IFLs could be formed is decorin. Liu *et al.* [133] have measured the force required to pull apart a single pair of decorin interactions to be 0.033 N/m. This study is one of the few studies that aids in estimating the stiffness that is associated with cross-links of these types.

In an effort to make this mesomodel as simple as possible, cross-links were modeled as simple linear springs in 3D in ABAQUS. The spring element (SPRINGA) acts between two nodes, with its line of action being the line joining the two nodes. This line of action can rotate in large-displacement analysis. The spring stiffness was estimated from the force-displacement data of the decorin molecules pulling experiment from Liu *et al.* Thus, a simple spring equation as Eq. (6.4) illustrates the simple mechanical behavior of the IFLs considered in this mesomodel:

$$F = -kx \tag{6.4}$$

6.1.4 Pre-stress due to Swelling

Swelling of cartilage arises from two different mechanisms: (1) osmotic swelling, which is due to an excess in ion particles inside the tissue, and (2) chemical expansion, due to repulsion of the closely spaced negatively charged groups of the PGs.

These mechanisms have been discussed in some detail in Sec. 3.3. The swelling pressure as a result of these mechanisms is high enough to keep cartilage "inflated" [134] in initial unloaded equilibrium. Ogston originally proposed the idea that in connective tissues the collagen network resists the osmotic swelling pressure exerted by the PGs [134]. This idea has since been verified by different studies. As a result of the swelling of cartilage, the collagen network is "prestressed" with tensile stresses and compressive stresses in the EFM. Basser *et al.* used an osmotic stress technique to measure the cartilage swelling pressure as a function of the hydration of the tissue [135]. These measurements are used as initial pore pressure in the mesomodel to obtain initial unloaded equilibrium as described below.

Normal cartilage is in equilibrium *in vivo* whereas the FEA always starts without swelling. Hence, the model has to equilibrate to the equilibrium pore pressure prior to any simulated mechanical test. This was done by using a Geostatic Stress Field procedure available in ABAQUS as the first step of FEA. In this step, Abaqus/Standard checks for equilibrium and iterates, if needed, to obtain a stress state that equilibrates the prescribed boundary conditions and loads (ABAQUS Analysis Manual). This stress state, which is a modification of the stress field defined by the initial conditions, is then used as the initial stress field in a subsequent simulated mechanical test.

6.2 Model Parameters

In summary, the matrix is modeled as a porous material that allows the flow of interstitial fluid (water) into and out of the tissue and within the tissue. In the context of the biphasic model, the collagen fibrils, the EFM and the IFL form the solid phase, whereas the poroelasticity of the EFM accounts for the water in the tissue. For the purpose of this mesomodel, viscoelasticity of the solid phase is

Table 6.1: List of parameters in the mesomodel

E_{m}	Elastic Modulus of the extra-fibrillar matrix
E_{f}^{+}	Elastic Modulus of the fibrils in tension
E_{f}^{-}	Elastic Modulus of the fibrils in compression
ν_{m}	Poisson's ratio of the extra-fibrillar matrix
ν_{f}	Poisson's ratio of the fibrils
κ	Permeability of the extra-fibrillar matrix
p	Initial pore pressure in the EFM
D	Fibril Diameter
k_{xz}	Stiffness of in-plane, non-diagonal inter-fibrillar cross-link (XZ plane)
k_{dxz}	Stiffness of in-plane, diagonal inter-fibrillar cross-link (XZ plane)
k_{dxy}	Stiffness of out-of-plane, diagonal inter-fibrillar cross-link (XY plane)
k_{dyz}	Stiffness of out-of-plane, diagonal inter-fibrillar cross-link (YZ plane) (Refer to Fig. (6.3) showing different cross-link orientations)
v_{f}	Fibril volume fraction
d	In-plane inter-fibrillar distance (XZ plane)
d_{v}	Inter-fibrillar distance in the Y direction

neglected. Thus, it is assumed that the time-dependent behavior of the tissue is entirely driven by the permeability of the EFM. A list of the parameters involved in the mesomodel is presented in Table 6.1. In the course of parametric studies only a limited number of important parameters are varied while others are left unchanged. Chapter 7 discusses this in detail.

The dimensions of the cross-link stiffness and the elastic moduli of the extra-fibrillar matrix and fibrils are different and, therefore, cannot be compared directly. Straightforward dimensional considerations allow us to define the equivalent stiffness for the extra-fibrillar matrix and the fibrils to aid in direct comparison to the stiffness of the cross-links. For this purpose simple stiffness relations are used as described below.

The equivalent stiffness k_{m} of the extra-fibrillar matrix along the Y direction is

obtained by the relation

$$k_{\mathrm{m}} = \frac{A_{\mathrm{m}} E_{\mathrm{m}}}{h} \tag{6.5}$$

where A_{m} is the area of the extra-fibrillar matrix element and h the height of the typical model element. A typical model element is described in the model geometry (Sec. 6.3).

Similarly, the equivalent stiffness k_{f}^{+} and k_{f}^{-} of the fibrils in tension and compression respectively are calculated by using

$$k_{\mathrm{f}} = \frac{A_{\mathrm{f}} E_{\mathrm{f}}}{h} \tag{6.6}$$

by substituting the corresponding k_{f} and E_{f} in tension and compression, respectively.

6.3 Model Geometry

The initial geometry selected for the model was a cube of side 1 μm. The length of the side of the cube was changed later in order to determine the optimum size of the model for conducting parametric studies. The initial geometry consisted of an assembly of all the components of the model. It is a network of cross-linked collagen fibrils embedded in an EFM composed of mainly PGs. The center of the cube is located at the origin, so that the cube vertices go from $-a$ to a along X, Y and Z directions ($a = 0.5$).

The collagen fibril network considered in this model is structured. Each fibril is almost vertical (angle made with the Y axis $< 0.1^{o}$) based on observed fibril orientation in the bovine patella. The entire cube can be thought of as an assembly of rectangular columns as shown in Fig. 6.1. Each column is composed of 4 fibrils that form its vertical edges, each fibril shared with the neighboring columns. The space between the fibrils is filled up completely by the EFM. Each column was

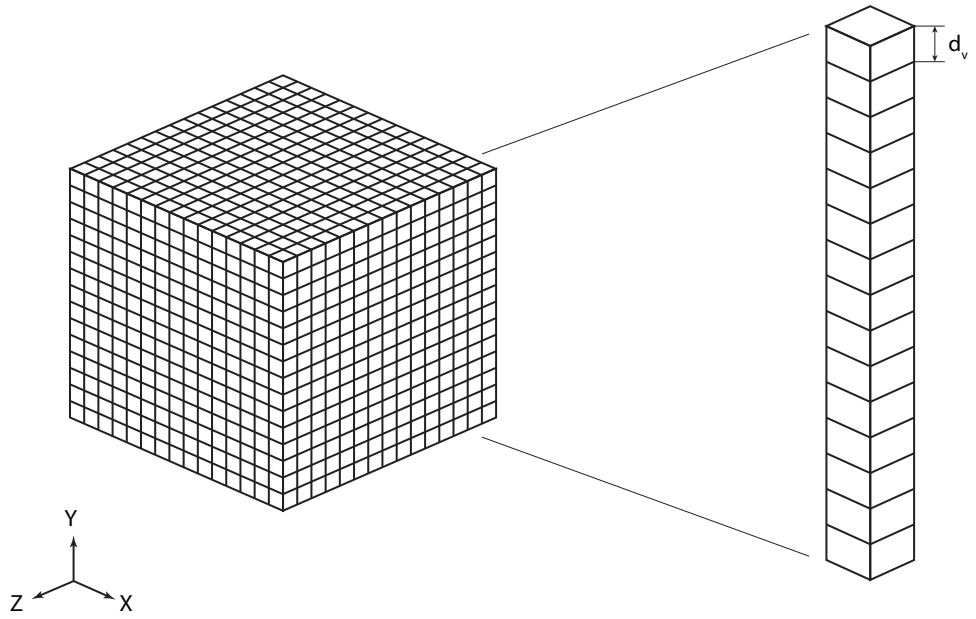

Figure 6.1: A schematic representation of the initial model geometry is shown. The model assembly is an approximate cube of side 1 μm. Crosslinks are not shown. Each edge of the column is a whole-length fibril.

discretized into smaller cubes each of which formed the typical unit cell of the entire assembly. The typical 8-noded cell is a superposition of the fibril and cross-link elements over the extrafibrillar matrix element. Each matrix element shares its nodes with 4 fibril elements that form its Y edges. At each edge, the fibril elements are shared with the neighboring cells. This eliminates the need to model interactions between the fibrils and the EFM. A typical unit cell of the model assembly is shown in Fig. 6.2.

The IFL configuration is also well defined. Each node pair that did not form a fibril element was a candidate for an IFL. For example, in Fig. 6.2, node 2 can have a cross-link with all other nodes except node 1. However, for simplicity, the number of cross-links is kept to a minimum while retaining the stability of the structure. In 2D, the simplest determinate truss configuration which is stable is a triangle. Similarly, in 3D, the simplest determinate truss configuration that is stable is a tetrahedron. The smallest number of tetrahedrons that can triangulate a cube is 5. This is obtained by using the cross-links shown in Fig. 6.2. The cross-links can be divided into three types with reference to the XZ plane (plane perpendicular to the fibril direction): (a) In-plane, non-diagonal cross-links (Fig. 6.3a), (b) In-plane, diagonal cross-links (Fig. 6.3b), (c) Out-of-plane, diagonal cross-links (Fig. 6.3c and d).

The cross-link orientations are identified in Fig. 6.3. During generation of this cross-link configuration, care was taken that neighboring assembly elements did not have a repetition of the same cross-link. Also, all adjacent assembly elements to a particular assembly element had the opposite configuration of diagonal cross-links. The original and opposite cross-link configurations are shown in Fig. 6.4.

The interfibrillar distance, d, is related to the fibril volume fraction, v_{f}, and the fibril diameter, D. This can be understood from looking at the top view of the model assembly as shown in Fig. 6.5. The model assembly is made up of typical

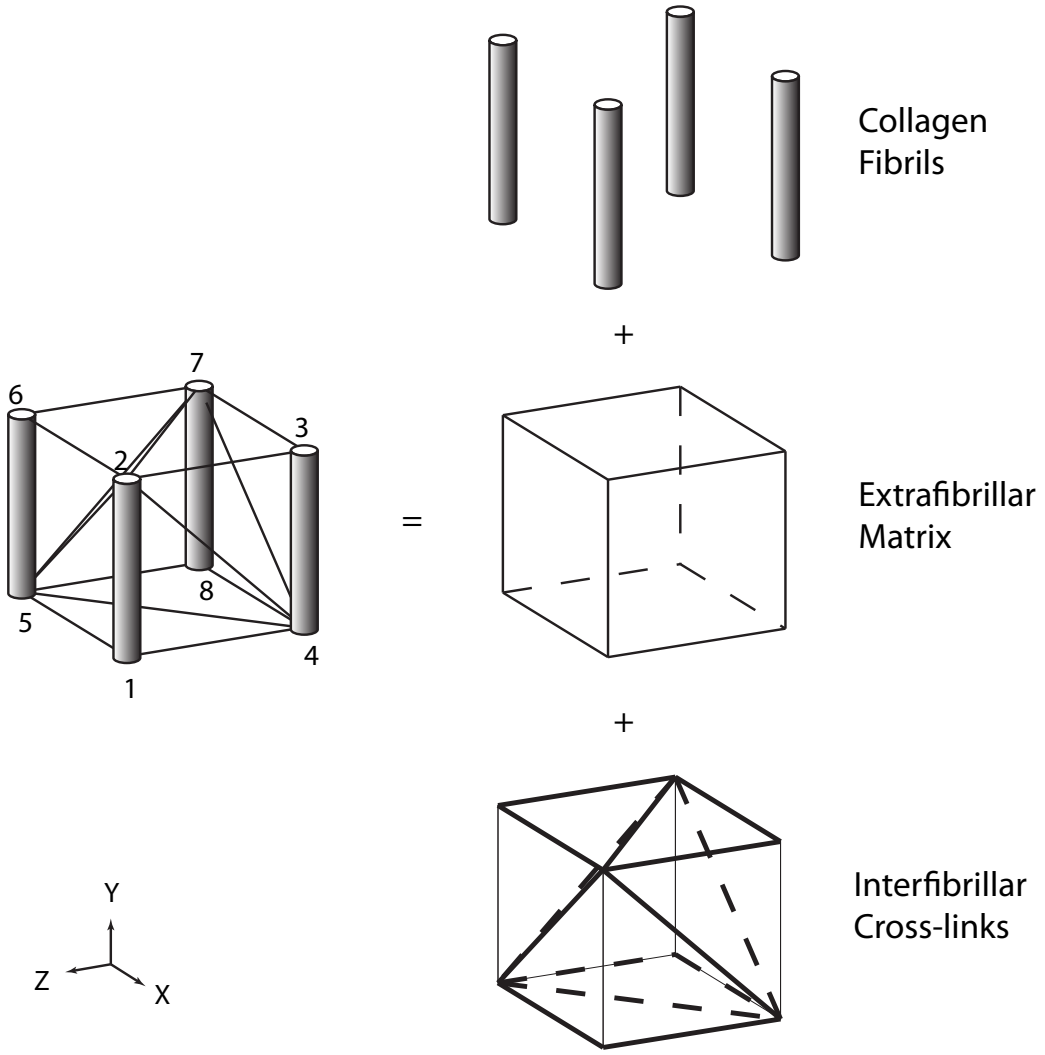

Figure 6.2: A typical unit cell of the mesomodel assembly is a superposition of the collagen fibril and IFL elements over the EFM element. All these elements share the 8 nodes. Node numbering scheme is consistent with ABAQUS. Fibrils at the edges are shared with the neighboring cells.

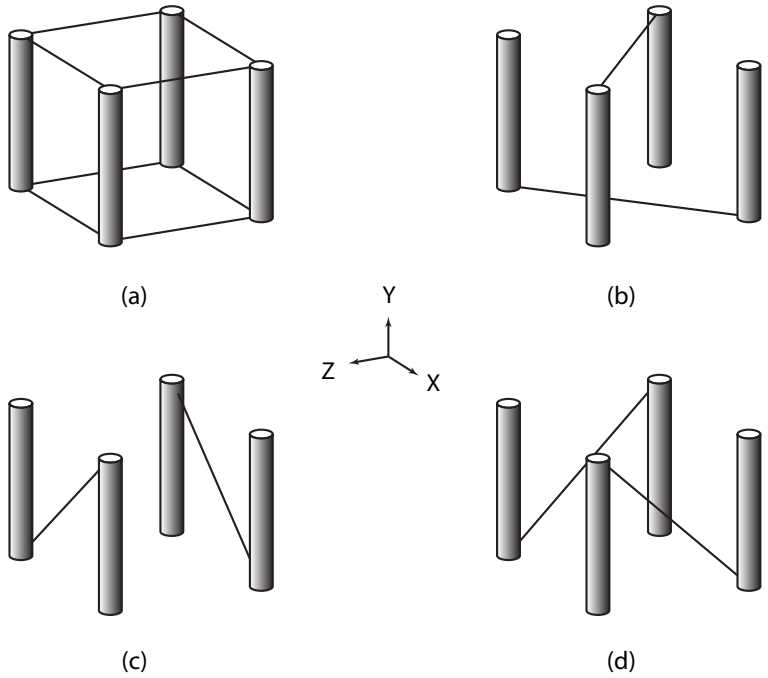

Figure 6.3: Different orientations of the IFLs in a typical assembly element with reference to the plane perpendicular to the fibril direction (XZ). (a) In-plane, non-diagonal (XZ). (b) In-plane, diagonal (DXZ). (c) (DXY) and (d)(DYZ) show the out-of-plane diagonal cross-links.

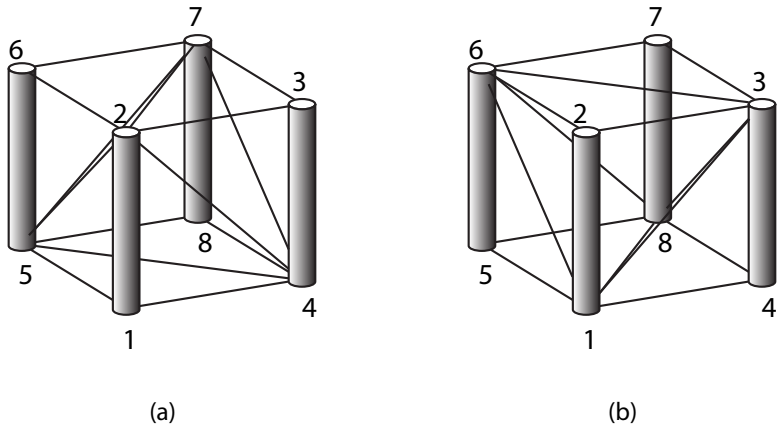

Figure 6.4: Opposite cross-link configurations of adjacent cells. If a typical assembly cell was of the configuration as shown in (a), all the assembly cells adjacent to it had the configuration shown in (b).

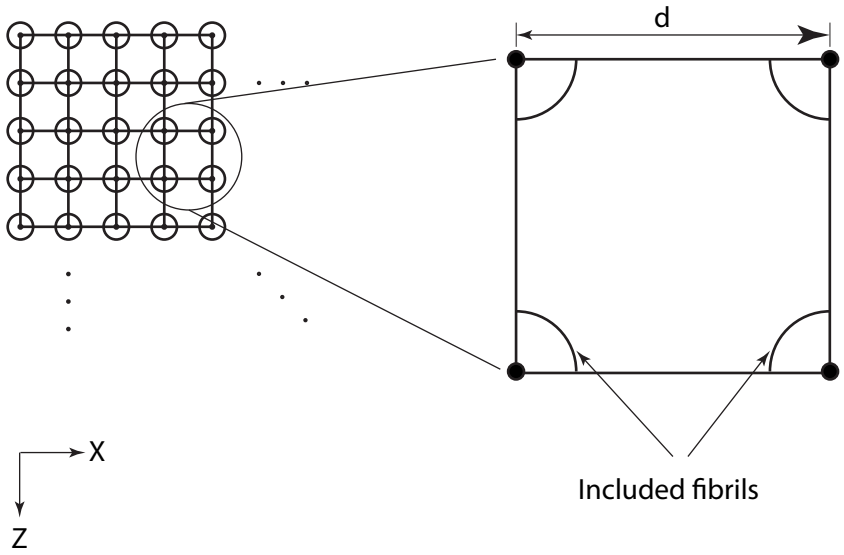

Figure 6.5: A schematic showing the top view of the initial model assembly. Considering only the included area, each typical assembly cell includes 1 fibril element. The interfibrillar distance, d, is thus related to the volume fraction of fibrils, v_{f}, and the fibril diameter, D.

elements which are the same size and dimensions. The total volume of the model is therefore easily calculated to be

$$V = vn_{el} \tag{6.7}$$

The number of typical cells, n_{el}, is always a known quantity. The volume of a typical cell, v is calculated from its dimensions as

$$v = a_c h \tag{6.8}$$

where a_c is the area of cross-section and h is the height of the typical cell. It is easily observed that no matter what the height of the typical cell, the cell volume is partitioned according to the areas between the fibrils and the matrix. If only the

internal included area is considered (which is normally the case for a unit cell), it is further observed that every typical cell includes exactly one fibril element volume. Or in other words, there is exactly one fibril per column of the model. Also, because all the typical cells are approximately the same size and dimensions, the fibril volume fraction in the model is approximately equal to the fibril volume fraction in a single typical cell. Thus, the fibril volume fraction is calculated as

$$v_{\mathrm{f}} = \frac{a_f}{a_c} = \frac{\pi D^2}{4d^2} \tag{6.9}$$

The interfibrillar distance is equal in the X and Z directions and is initially set equal to the fibril element length. Each fibril element is discretized along its length so that the distance between two successive nodes along a fibril, d_{v}, is approximately 67 nm, the typical D-period observed in collagen.

6.3.1 Geometry generation

The model geometry is generated using a program written in the commercial software MATLAB. The terminology used is discussed briefly here. The fibril volume fraction, v_{f}, and the fibril diameter, D, are set constant and the inter-fibrillar distance, d, is calculated using Eq. (6.9). A term 'order of the model', n, is introduced which sets the number of fibrils in the model. For a model of order n, the number of columns is n^2 and the number of fibrils is $(n+1)^2$. This is illustrated in Figs. 6.5 and 6.6. For the purpose of determining the base model, the height of the model is maintained at 1 μm. Once a suitable minimum number of fibrils needed is determined, the height of the model is adjusted so as to obtain a cube model geometry. The base model and the procedure used to determine it is described in Sec. 6.5.

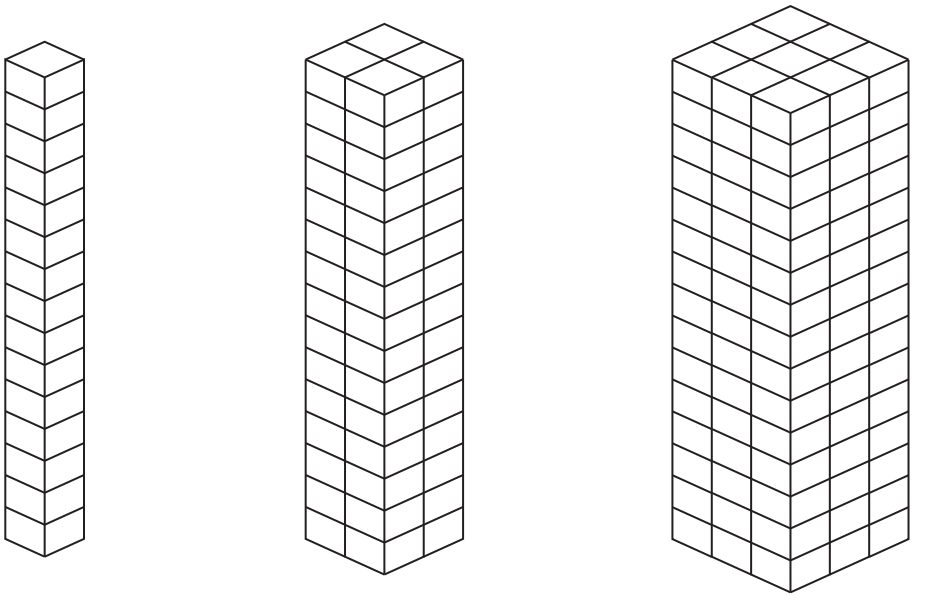

Figure 6.6: Generated model geometry for $n = (1, 2, 3)$. As n increases, the aspect ratio of the assembly changes and starts approaching 1.

6.4 Calculation of Effective Properties

The average stress theorem and the average strain theorem are used to calculate the average stresses and average strains in the model. The effective material properties are then calculated based on the corresponding average stress and average strain.

6.4.1 Average Stress Theorem

The volume-average theory or the average stress theorem [136] is used to determine the average stress on the RVE. This theorem states that in case of absence of body forces, for a given uniform external load on an RVE the volume average of the forces within the RVE is identical to the given force on the boundary. ABAQUS reports the Cauchy stress tensor S_{ij} at all the integration points in the model. Thus, the averaged stress is given by

$$\langle \sigma_{ij} \rangle \equiv \frac{1}{V} \int_V S_{ij} \mathrm{d}V \tag{6.10}$$

where V is the volume of the RVE. The gradient of the directional vector x can be written as

$$(\nabla \mathbf{x}) = x_{i,j} = \delta_{ij} \tag{6.11}$$

where δ_{ij} is the Kronecker delta. The stress tensor is thus given by

$$S_{ij} = S_{kj}\delta_{ik} = S_{kj}x_{i,k} \tag{6.12}$$

At equilibrium, i.e., $S_{kj,k} = 0$, the divergence theorem gives

$$\langle \sigma_{ij} \rangle = \frac{1}{V} \int_V S_{kj}x_{i,k} \mathrm{d}V = \frac{1}{V} \int_V (S_{kj}x_i)_{,k} \mathrm{d}V - \frac{1}{V} \int_V S_{kj,k}x_i \mathrm{d}V \tag{6.13}$$

$$\langle \sigma_{ij} \rangle = \frac{1}{V} \int_{\partial V} n_k S_{kj} x_i \mathrm{d}S \tag{6.14}$$

where $n_k S_{kj}$ is the traction, t_j, exerted on the boundaries of the RVE. Therefore,

$$\langle \sigma_{ij} \rangle = \frac{1}{V} \int_{\partial V} x_i t_j \mathrm{d}S \tag{6.15}$$

Eq. (6.15) is given in discrete form by [137]

$$\langle \sigma_{ij} \rangle = \frac{1}{V} \sum_{boundary nodes} x_i F_j \Delta S \tag{6.16}$$

where x_i is the i-component of the position of the boundary node and F_j is the force developed on the boundary node in the j-direction.

6.4.2 Average Strain Theorem

The average strain theorem states that for an exterior homogeneous displacement given on the entire boundary of the RVE, the volume average of the strain is the constant strain applied at the surface as given by Eq. (6.17). The reader is referred to Loehnert [136] for details.

$$\langle \varepsilon_{ij} \rangle = \varepsilon^0_{ij} \tag{6.17}$$

where ε^0_{ij} is the constant strain applied at the surface.

6.4.3 Effective Material Property

The effective material property is calculated only in the *main direction of stresses* relative to the displacement used on the model. A specific displacement is applied to the model to calculate a specific material property. For example, when applying a compressive displacement in the Y-direction, i.e., along the fibril axial direction, then then effective compressive modulus is calculated from the volume average stress

and strain tensors in the direction of the perturbation,

$$E_{yy}^{eff} = \frac{\langle \sigma_{yy} \rangle}{\langle \varepsilon_{yy} \rangle} \tag{6.18}$$

The other components of the stress tensor are neglected in this case. This procedure is valid only if a uniaxial stress state is achieved from the perturbation on the model. The choice of boundary conditions is, thus, important. The 3D homogeneous boundary conditions and 3D periodic boundary conditions retain such a uniaxial stress state in the model.

6.5 Base Model

In order to conduct the parametric studies on the mesomodel, some preliminaries need to be considered. These include determining the optimum size (number of fibrils) of the model, discussing which boundary conditions are appropriate for parametric studies and finalizing the simulated mechanical tests for the parametric studies. This section discusses these baseline choices.

6.5.1 Optimum size

To reduce the computation time, it is desirable to have the smallest size of the model that can give consistent results. As a result of the method of model generation, the size of the typical element is constant for a given combination of v_f and D. Thus, the size of the model is governed by the number of fibrils desired. The optimum size of the model is determined using the procedure described below. Simulations of unconfined compression along the Y direction for the mesomodel were carried out for various values of cross-link stiffness k. All the cross-links, i.e., in-plane as well as out-of-plane, were active and had the same stiffness, k. The pore pressure was set to zero during this entire procedure. Table 6.2 lists values used for the parameters

Table 6.2: Values of model parameters used for obtaining base model

E_{m}	30 Pa ($k_{\mathrm{m}} \sim 10^{-8}$mN/$\mu$m)
E_{f}^{+}	150 MPa
E_{f}^{-}	0.1 MPa ($k_{\mathrm{f}}^{-} \sim 10^{-3}$mN/$\mu$m)
ν_{m}	0.5
ν_{f}	0.5
κ	2×10^{-15} m^4/N-s
D	50 nm
$k_{\mathrm{xz}} = k_{\mathrm{dxz}} = k_{\mathrm{dxy}} = k_{\mathrm{dyz}}$	k
v_{f}	0.4
$d = d_{\mathrm{v}}$	~ 67 nm

during this procedure.

Figure 6.7 shows a schematic representation of the unconfined compression simulation setup. These simulations were carried out for $n = 13$ or 196 fibrils. This value of n generates a model that has an aspect ratio of 0.98 for the geometry parameter values as in Table 6.2, closest to the desired value 1 of the cube. For these simulations, all the nodes on the top surface were prescribed a 5% displacement in the negative Y direction and the Y displacement of all the nodes on the bottom face was fixed to zero such that free Poisson effect could be obtained along the X and Z directions.

During preliminary studies for small number of fibrils (4, 9, 16, i.e., for small n), it was observed that for small values of k ($k/k_{\mathrm{m}} < 10^{-4}$), there was an excessive 'hour-glass' distortion of the matrix elements caused by random bending of the fibrils. This effect gradually disappeared and the fibrils deformed together more and more as a unit with increasing k. Thus, the lowest value of k for which there was a reasonable deformation of matrix elements (no hour-glass effect) was obtained and fixed for the next step. This value was found to be of the same order of k_{f}^{-}, i.e., $k/k_{\mathrm{f}}^{-} \approx 1 \approx k_{\mathrm{m}} \times 10^{5}$. The stiffness k was held constant at this value and the order

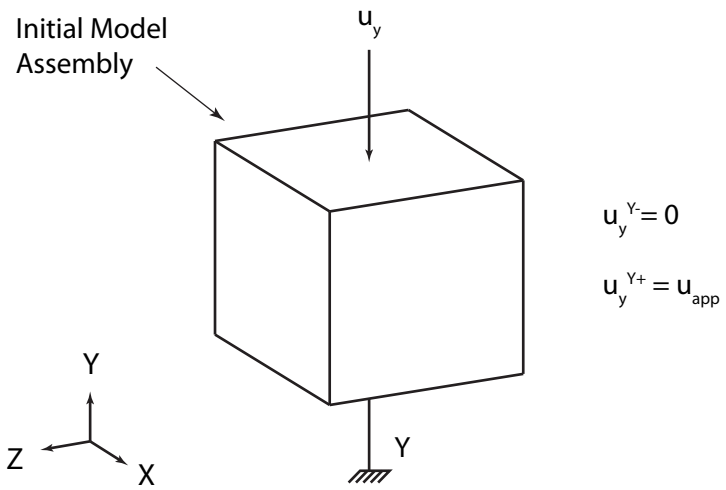

Figure 6.7: A schematic showing the setup of the unconfined compression simulations on the initial model assembly geometry.

of the model was increased from 1 to 13 and simulated unconfined compression tests were carried out. Note that for each different value of n, the aspect ratio (ratio of assembly width to assembly height) of the model assembly was different because the height remained constant while the width increased with n (refer to Fig. 6.6)). Thus, the aspect ratio of the assembly increased with increasing n and approached 1 as the assembly approached the shape of a cube. For each n, the effective modulus in compression was calculated as explained in Sec. 6.4 and compared. The goal was to determine the smallest number of fibrils that gives the same effective modulus with addition of more fibrils.

Figure 6.8 summarizes the results of these simulations. For small values of n the effective modulus in compression, E_{yy}^{eff}, decreases steeply with increasing number of fibrils. But, as more and more fibrils are added, the reduction in E_{yy}^{eff} decreases and starts to plateau. It is clearly seen that after 100 fibrils ($n = 9$), E_{yy}^{eff} hardly shows any variation. To err on the side of caution, the optimum size of the model is chosen as $n = 10$ or 121 fibrils. This choice of n results in a model with unequal width and

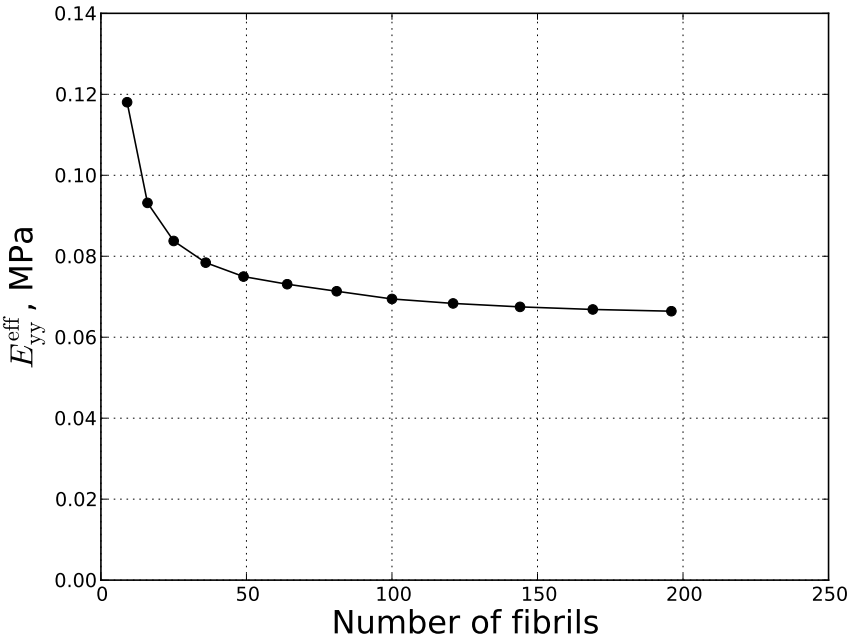

Figure 6.8: Plot showing sensitivity of E_{yy}^{eff} calculated for unconfined compression to the number of fibrils used in the mesomodel. For less than 50 fibrils, E_{yy}^{eff} decreases rapidly with increasing number of fibrils. However, for more than 50 fibrils, the decrease in E_{yy}^{eff} starts to plateau as number of fibrils increase.

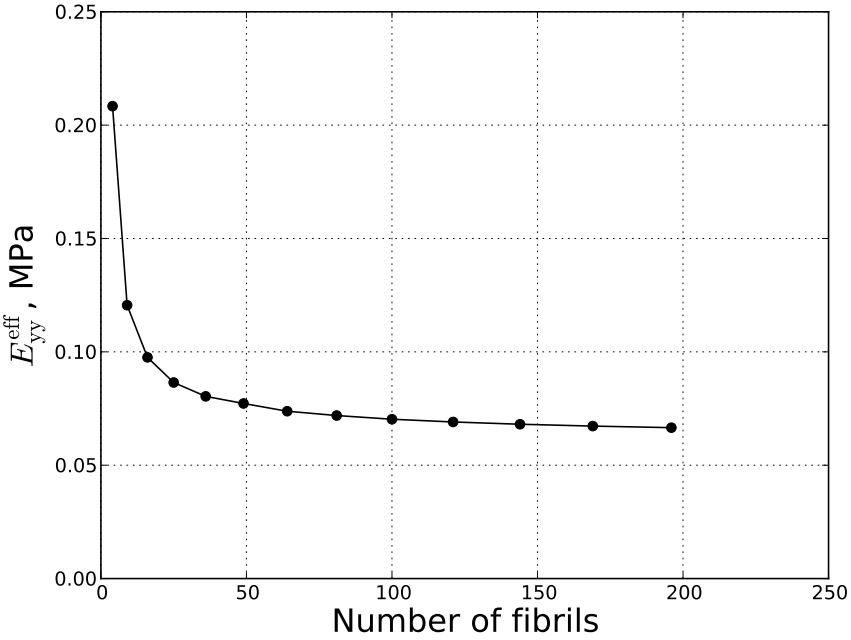

Figure 6.9: Plot showing sensitivity of E_{yy}^{eff} calculated for unconfined compression to the number of fibrils used in the mesomodel with a cube geometry. The variation in E_{yy}^{eff} has a similar trend as Fig. (6.8)

height. To maintain the aspect ratio close to 1, the height of the fibrils is reduced to the width of the model with 121 fibrils.

To check if the variation of E_{yy}^{eff} observed above was not due to the changing aspect ratios, another set of simulations of unconfined compression along the Y direction were carried out for the same fixed value of k and for n ranging from 1 to 13. However, this time, the model aspect ratio was maintained for each n to 1, i.e., the model assembly was maintained as a cube. Thus, the mesomodel was simply an assembly of n^3 typical elements. In this study, as n changed, the aspect ratio remained constant, but the height of the fibrils increased with increasing n. Fig. 6.9 shows the results of the simulations for these set of simulations with constant aspect ratio of the model assembly. A similar variation of E_{yy}^{eff} with number of fibrils is seen. This plot confirms our choice of 100 fibrils or more. Thus, the choice of a

cube model with 121 fibrils is selected as the optimum size for the model.

6.5.2 Boundary Conditions

Generally numerical simulations are conducted owing to complexity of analytical models. However, it is often unnecessary and inefficient to simulate an entire system. Therefore, a region of interest is chosen for numerical simulation and the physical processes outside the region are included by the choice of appropriate boundary conditions. With different boundary conditions one may obtain totally different results from numerical simulations. Also, improper boundary conditions may reflect or introduce non-physical phenomena on the region of interest.

When dealing with numerical simulations of a microstructure the boundary conditions reflect the role played by the microstructure in the macroscopic behavior. Two types of boundary conditions are usually considered: periodic boundary conditions and homogenous boundary conditions.

Periodic Boundary Conditions

The microstructure of interest is often a RVE of the macrostructure, i.e., the macrostructure can be thought of as an assembly of periodically-repeated cells that the microstructure represents, thus homogenizing the heterogenous material. In such cases, periodic boundary conditions are appropriate. As the periodic array of the repeated RVEs forms a continuous physical body, it follows that the following conditions be satisfied at the boundaries of neighboring cells: the displacements need to be continuous, i.e., adjacent cells cannot penetrate or separate after deformation, and the distributions of traction need to be the same on opposite boundaries.

Figure 6.10 adapted from van der Sluis *et al.* [138] shows a periodically deformed unit cell under uniaxial tensile conditions in 2D. The periodic boundary conditions for this case are:

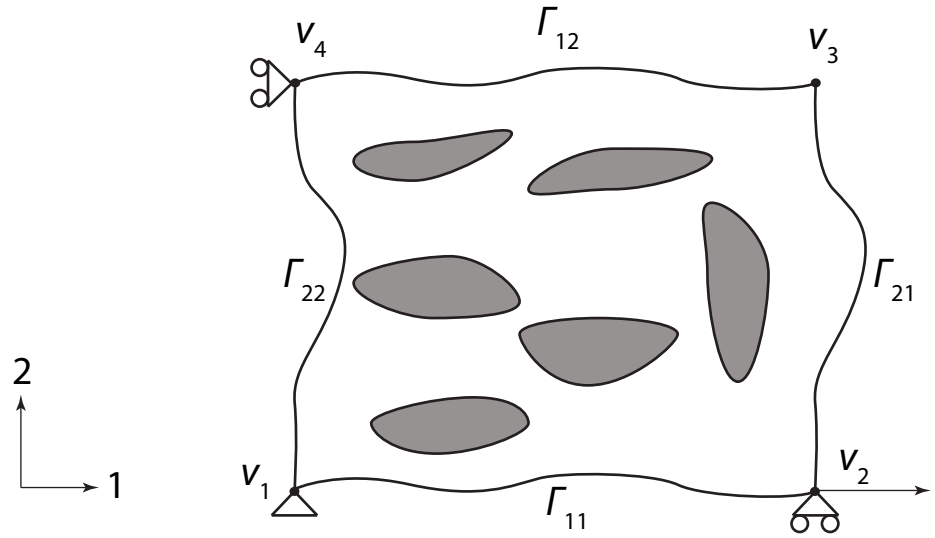

Figure 6.10: Periodically deformed unit cell with boundaries Γ_{IJ} and vertices v_i.

$$\begin{aligned} \mathrm{u}_{12} - \mathrm{u}_{v_4} &= \mathrm{u}_{11} - \mathrm{u}_{v_1} \\ \mathrm{u}_{22} - \mathrm{u}_{v_1} &= \mathrm{u}_{21} - \mathrm{u}_{v_2} \\ \mathrm{u}_{v_3} - \mathrm{u}_{v_2} &= \mathrm{u}_{v_4} - \mathrm{u}_{v_1} \end{aligned}$$

The implementation of 3D periodic boundary conditions is quite complex. Also, in the context of soft tissues, the mesostructure that the mesomodel represents cannot be considered as an RVE due to the spatial and structural variation in the composition of soft tissues. Thus, periodic boundary conditions are not appropriate for this study. Homogeneous boundary conditions are used instead.

Homogenous Boundary Conditions

The choice of homogeneous boundary conditions implies that the RVE with its micro-constituent can be considered as a material specimen. That is we are simulating a very small specimen from some part of the macrostructure which is closely approximated by the RVE. Not only is the use of homogeneous boundary conditions

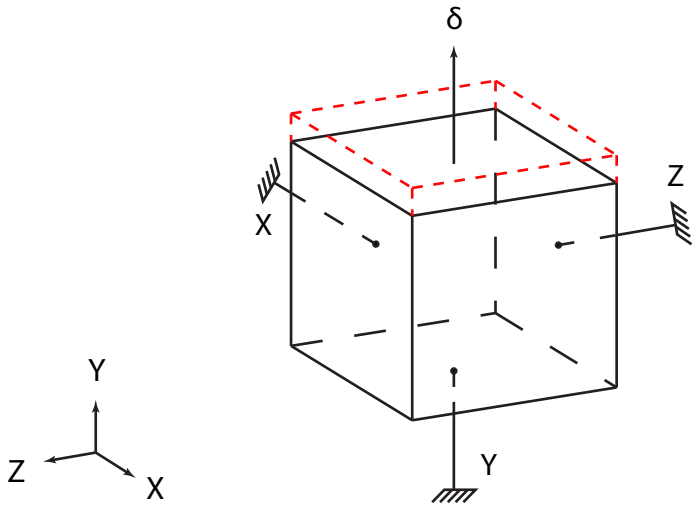

Figure 6.11: A schematic showing the setup for the simulated uniaxial perturbation tests for the mesomodel. Displacement δ is positive for tension and negative for compression.

appropriate, but, also they are much easier to implement, are less time consuming and require less computational effort than the periodic boundary conditions.

The homogeneous boundary conditions are obtained from Aboudi [139]. Three adjacent faces (X-, Y- and Z-) are chosen as the planes of symmetry. Certain degrees of freedom on the these symmetry faces are restrained. The other three faces are set free of constraints and the desired displacement applied depending upon the simulated test (uniaxial compression along the fibril direction Y+).

The displacements chosen represent the main mode of loading in different tissues. Uniaxial compression is used to study articular cartilage, as that is the prevalent loading mode in articular cartilage. Similarly uniaxial tension is used to study tendons.

Figure 6.11 shows this procedure for simulated uniaxial tests. The symmetry faces were constrained such that no displacements occurred normal to the faces. Any

points on these faces are free to slide along the planes in which they lie. All other (non-symmetrical) faces are free of any displacement constraints and are traction free. The uniaxial tests of compression (for articular cartilage) and tension (for tendon) along the fibril direction (Y) were then carried out. Compression tests were conducted at a strain rate of $0.2\%/sec$ while tension tests were performed at $1\%/sec$.

Chapter 7

Parametric Study

This chapter details the parametric study undertaken to assess the sensitivity of the mesomodel to various parameters involved. Unless otherwise stated, the parametric variations were carried out for simulated uniaxial compression tests along the fibril direction. This was done as compression tests are most relevant to articular cartilage.

We first consider variations of cross-link stiffness and geometry. We then consider variations of different material parameters. For the latter variations, all simulations were performed for two different configurations of interfibrillar cross-links (IFLs). The results show how the presence of cross-links affects the effective modulus in compression.

Table 7.1: Parameter base values used for parametric study.

E_{m}	0.5	MPa
E_{f}^{+}	150	MPa
E_{f}^{-}	2	MPa
ν_{m}	0.5	
κ	2.1×10^{-15}	m^4/N-s
p	0.0395	MPa
D	40	nm
k	0.0033	N/m
v_{f}	0.256	
d	70	nm
d_{v}	70	nm

7.1 Base values for parameters

The base values of the model parameters for the parametric study are listed in Table 7.1. Unless otherwise stated, the model parameters were set to these values. The choices for these base values are based on literature values and discussed in Chapter 6. Typical deformed and undeformed configurations of the mesomodel and the undeformed fibril orientations in simulated compression tests are shown in Fig. 7.1.

7.2 Effect of Cross-link stiffness, k

The focus of the mesomodel is to assess the mechanical effect of the IFLs and their contribution to the overall stiffness of the tissue. As discussed earlier, the exact mechanical nature of these cross-links is not known. However, some information on their potential stiffness is available. Following Liu *et al.* [133] and using Eq. (6.4), the cross-link stiffness, k, is calculated to be 0.033 N/m. Redaelli *et al.* [140], through a molecular mechanics approach, obtained stiffness values of 2.7×10^{-8} N/m at low strains and 3.1×10^{-2} N/m at high strains for tension in the

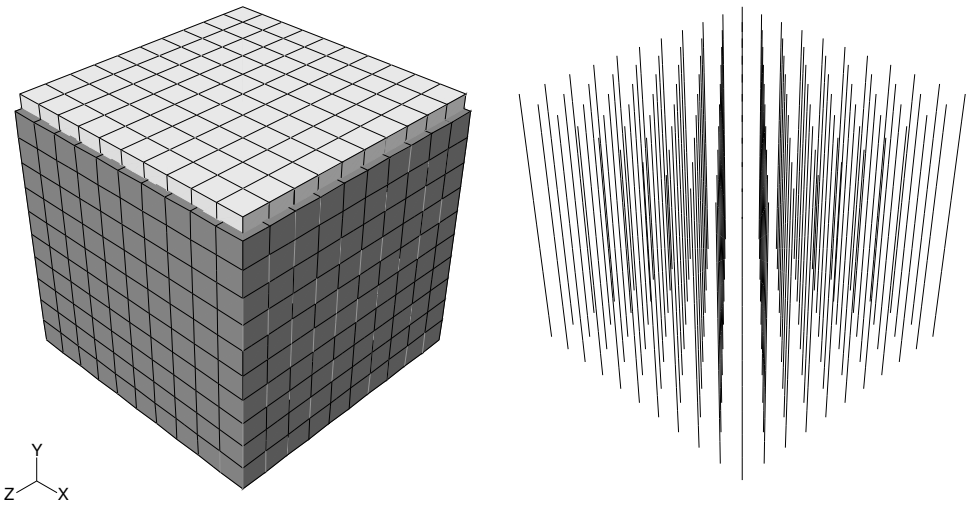

Figure 7.1: Typical configurations of the mesomodel in a simulated compression test. *Left*: Deformed configuration (grey) at 5% strain superimposed over the undeformed (white) configuration. *Right*: Undeformed fibril orientations are shown.

glycosaminoglycans (chondroitin-6-sulphate) bound to decorin in tendon. Using these values as a reference, k was varied over several orders of magnitude. For each cross-link configuration studied, all active links were assumed to have the same cross-link stiffness, k. Different cross-link orientations are shown in Fig. 6.3. In simulations assessing the effect of cross-link stiffness k, all cross-links were active. In preliminary simulations, it was observed that simulation runtimes with k of the order of 10^{-2} (Liu *et al.* and Redaelli *et al.* for large strains) were of long duration ($\sim$ 24 hrs for 3% strain). In the interest of faster simulations, the values of k used were: no cross-links (or $k = 0$), $3.5 \times [10^{-6}, 10^{-5}, 10^{-4}, 10^{-3}]$ N/m. Although, the stiffness values reported in the literature (order of 10^{-2}) have not been used, we believe that this range of k is sufficient to study the qualitative effect of the IFLs on the model. All other parameters had the same values as in the base model (Sec. 7.1), except the value of κ used was 2×10^{-16} m^4/N-s.

In order to understand the interactions between the three components of the

mesomodel and to assess their relative contributions to E_{yy}^{eff}, the following three model compositions were studied:

- With all components included: fibrils, EFM and IFLs
- With the EFM removed, i.e., with fibrils and IFLs
- With the fibrils removed, i.e., with EFM and IFLs

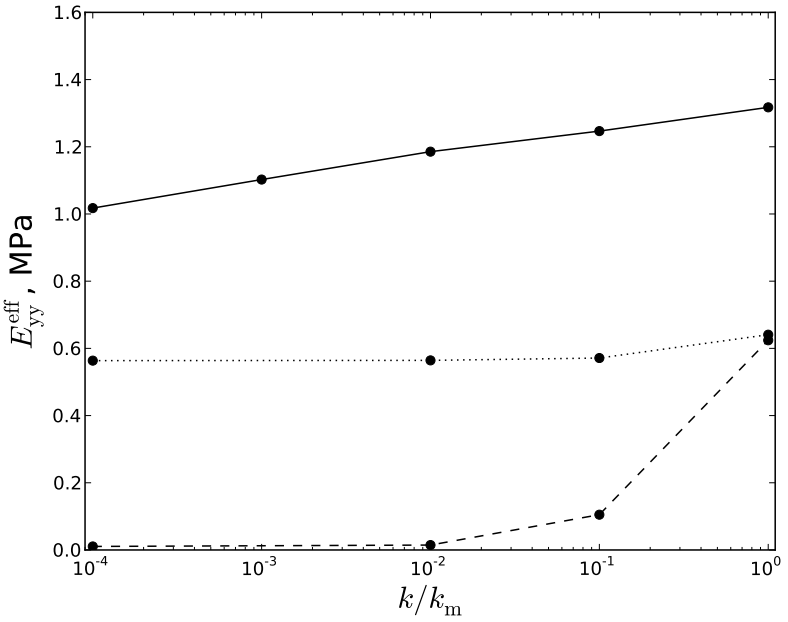

Figure 7.2: Effect of cross-link stiffness, k on E_{yy}^{eff}. All cross-links were active and had the same stiffness, k. Mesomodel with all components (–), EFM removed (- -), fibrils removed (. . .).

Recall from Sec. 6.2, k_m is the equivalent matrix stiffness with the same dimensions as k. The value $k_m = 3.5 \times 10^{-3}$ N/m for $E_m = 0.5$ MPa was used in the base model in the parametric study.

Figure 7.2 (solid line) shows effect of varying the cross-link stiffness for the mesomodel which included all components. The effective modulus in compression,

E_{yy}^{eff}, increases with increasing cross-link stiffness. The value of E_{yy}^{eff} reported for $k/k_m = 10^{-4}$ corresponds to the value obtained when cross-links were removed ($k = 0$). The value of E_{yy}^{eff} obtained for $k = k_m$ was $\sim$ 32% higher than that obtained with all cross-links removed.

Figure 7.2 (dashed line) shows the effect of varying cross-link stiffness on the effective modulus, E_{yy}^{eff}, with the EFM elements removed. When both the cross-links and the EFM elements were removed (only fibrils in the mesomodel), the effective modulus $E_{yy}^{eff} = 0.01$ MPa, is negligible when compared to $E_{yy}^{eff} = 1.32$ MPa calculated for $k = k_m$ with all components included. When only the EFM elements were removed, $E_{yy}^{eff} = 0.63$ MPa was 47% of the value calculated for the mesomodel with all components.

Figure 7.2 (dotted line) shows the effect of varying the cross-link stiffness on E_{yy}^{eff} with the fibrils removed from the mesomodel. Without cross-links and fibrils (only EFM in the mesomodel) the effective modulus $E_{yy}^{eff} = 0.56$ MPa, was $\sim$ 43% of $E_{yy}^{eff} = 1.32$ MPa calculated for $k = k_m$ with all components included. When only the fibrils were removed, $E_{yy}^{eff} = 0.64$ MPa was $\sim$ 49% the value calculated for the mesomodel with all components.

For the configuration with all model components included, the strain at which the first instance of bending of fibrils seen, ε_{yy}^{bend}, is reported in Table 7.2 and shown in Fig. 7.3. This observation was carried out manually, by looking at the deformed fibril configuration every 0.2% strain. It was observed that as k was increased, the first bending consistently occurred at higher strains and with $k = k_m$ no bending of fibrils was seen at 5% strain.

Table 7.2: Effect of varying cross-link stiffness on the effective modulus with all components included is shown.

k/k_{m}	$E_{\mathrm{yy}}^{\mathrm{eff}}$ (MPa)	$\varepsilon_{\mathrm{yy}}^{\mathrm{bend}}$ (%)
0	1.017	1.2
10^{-3}	1.102	2.0
10^{-2}	1.185	2.6
10^{-1}	1.247	4.4
10^{-0}	1.317	> 5

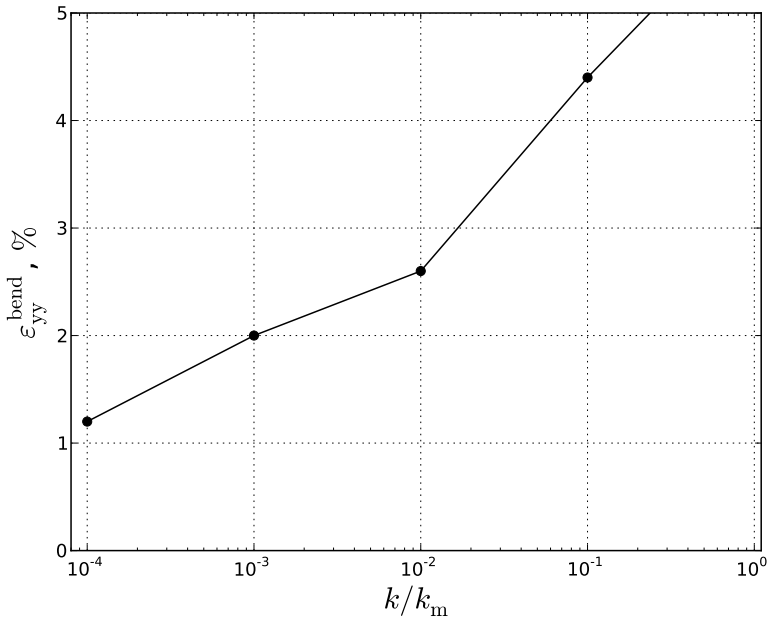

Figure 7.3: Effect of cross-link stiffness, k on $\varepsilon_{\mathrm{yy}}^{\mathrm{bend}}$ when all components were included in the mesomodel. All cross-links were active and had stiffness k.

Fig. (7.4) shows the effects of removing the EFM on the fibril configuration in the mesomodel at 3% strain with different values of k. When the cross-links were absent (top left) each fibril deformed individually, independent of the neighboring fibrils, resulting in markedly different fibril orientations. Bending of fibrils was also observed. Introduction of cross-links produced a more coordinated overall fibril orientation and deformation. For $k/k_{\mathrm{m}} = 0.01$ (top right), the fibrils showed co-ordinated deformation accompanied with bending, i.e., all fibrils were deforming similarly. For $k/k_{\mathrm{m}} = 1$ (bottom left), this effect was enhanced with reduced bending, while for $k/k_{\mathrm{m}} = 10$ (bottom right), no bending was observed.

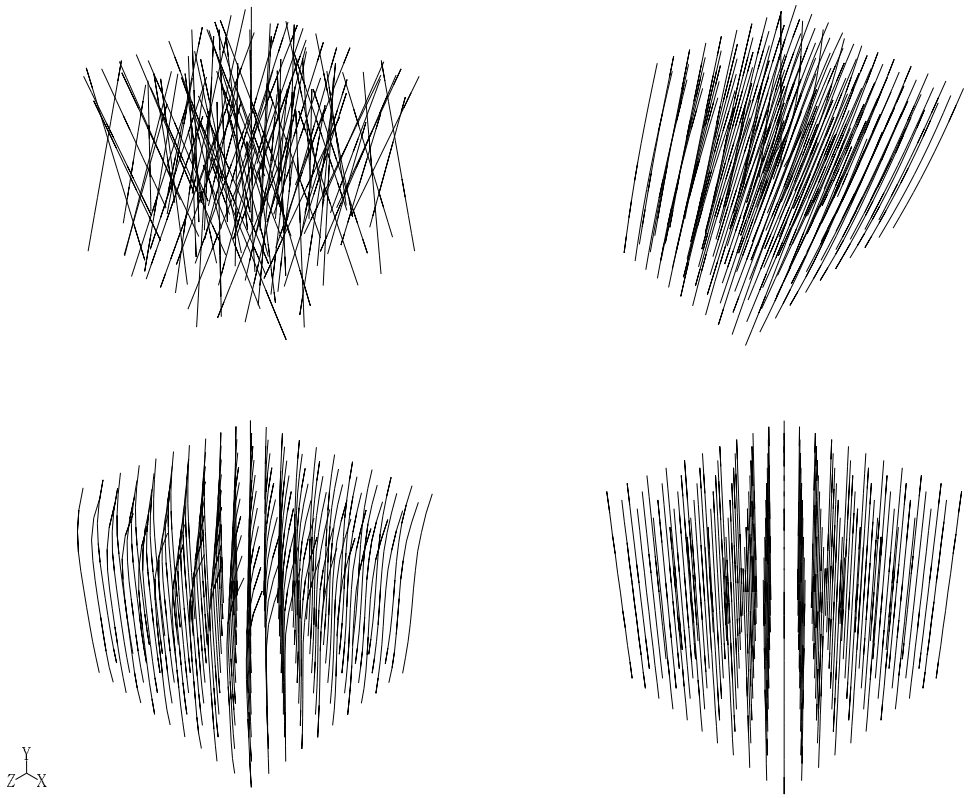

Figure 7.4: Effect of removing the EFM elements on the fibril configuration at 3% strain. All cross-links were active when cross-links included in the mesomodel. *Top left*: cross-links removed (only fibrils in the mesomodel), *top right*: $k/k_{\mathrm{m}} = 0.01$, *bottom left*: $k/k_{\mathrm{m}} = 1$, and *bottom right*: $k/k_{\mathrm{m}} = 10$.

Presence of IFLs increases the effective modulus in compression

These results clearly demonstrate that the inclusion of interfibrillar cross-links in the mesomodel increases the effective modulus in compression along the fibril direction. The percentage increase in the effective modulus due to presence of cross-links is directly related to the value of k used in the model.

Comparing the effective modulus for the different compositions with and without cross-links included is quite informative. Here we look at the different compositions for $k = k_{\mathrm{m}}$ and for $k = 0$ (i.e., with cross-links removed). With all components included in the model, the effective modulus of the mesomodel was 32% higher when cross-links are present. When the fibrils were removed from the model, presence of cross-links resulted in $E_{\mathrm{yy}}^{\mathrm{eff}}$ to be only $\sim$ 14% higher than with the cross-links removed. When the EFM is removed, this difference is dramatically increased. The fibrils by themselves provided neglible resistance to compression. But, in the presence of cross-links there was a $\sim$ 60 fold increase in the effective compressive stiffness of the mesomodel. This suggests that the presence of cross-links has a greater influence on the fibrils than on the EFM, likely due to increased stability of fibrils in the presence of cross-links.

IFLs organize and stabilize the fibrillar network

When the matrix was removed, and the cross-link stiffness varied, the deformation of the fibril network at the same strain level (3%) was markedly different as seen in Fig. 7.4. When all the IFLs were removed, each fibril deformed independent of the neighboring fibrils. With introduction of IFLs, for lower values of k/k_{m}, a more co-ordinated deformation accompanied by bending of fibrils was seen. Groups of fibrils deformed together, although there were differences in the fibril configurations among different groups. The cross-links connect individual fibrils with their neighboring fibrils, thus forming a fibrillar network that deforms in unison. At $k = k_{\mathrm{m}}$,

the deformed configuration of the fibril network was much more organized with almost all fibrils deforming together with reduced bending. At $k = 10k_{\mathrm{m}}$ (same order as reported by Liu *et al.* al [133]), no bending was observed with all fibrils in the mesomodel deforming together. This suggests that the IFLs may perform the important function of organizing the fibrillar network and imparting some stability to the network. In the presence of the IFLs, the fibrils can support compressive loads for larger strains before bending. Thus, the presence of cross-links contributes greatly to the ability of the fibrillar network to withstand compression.

The cross-links are not the only component that can organize and stabilize the fibrillar network. The EFM also seems to play a part in performing these functions. This is inferred by comparing the fibril configurations for two results at $k = k_{\mathrm{m}}$: first with only the EFM removed, and the second with all components included. In the absence of the EFM, the deformed fibril configuration showed bending in fibrils at 3% strain (refer to Fig. 7.4 bottom left). However, when the EFM was present, there was no bending seen in any fibrils in the model with strain at 5%. When the cross-links were removed from the model, in the absence of EFM, the fibrils deform independently, bending individually right from the beginning of application of compressive strain. When the EFM was present, the first bending in the fibrils determined visually was not before the strain reached $\sim 1.2\%$. From this we can conclude that the EFM assists the IFLs in organizing and providing stability to the fibrils.

Relative contributions of model components to $E_{\mathrm{yy}}^{\mathrm{eff}}$

Fig. 7.5 shows comparison of the effective modulus, $E_{\mathrm{yy}}^{\mathrm{eff}}$, for various compositions of the mesomodel. Results are shown for cross-link stiffness $k = k_{\mathrm{m}}$ for all cross-links, when cross-links were included. With all components, the effective modulus was 1.32 MPa. With cross-links and the EFM elements removed, $E_{\mathrm{yy}}^{\mathrm{eff}} = 0.01$ MPa.

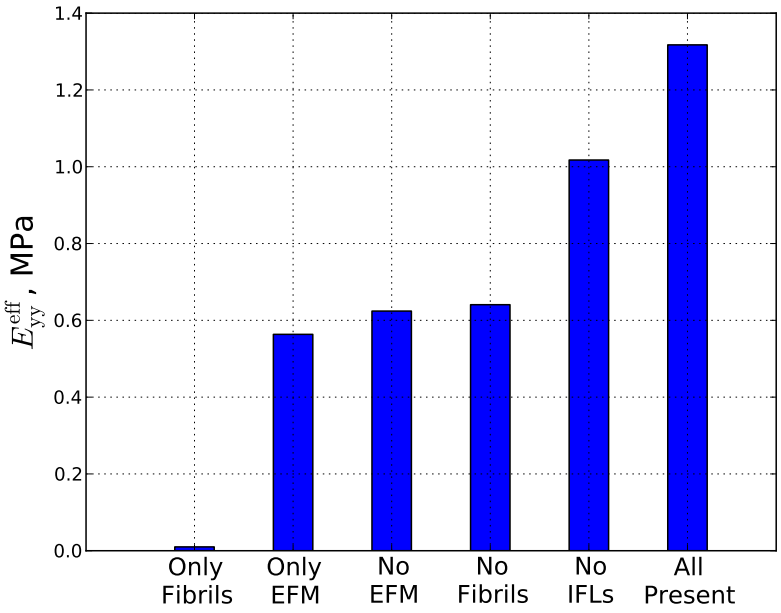

Figure 7.5: Comparison of E_{yy}^{eff} for different mesomodel compositions at $\varepsilon = 5\%$.

With addition of cross-links, E_{yy}^{eff} increased 60 times to 0.62 MPa. Thus, along with the IFLs, the fibrillar network contributed almost 47% of the effective modulus with all components. Addition of the EFM to the cross-linked fibril network, more than doubled E_{yy}^{eff} to 1.32 MPa. Thus, the total stiffness seems to be due to the combined fibril/cross-link network and the EFM. With the IFLs removed, the fibrils and the EFM together resulted in $E_{yy}^{eff} = 1.01$ MPa which is a 100 fold increase compared to the model with only fibrils. This demonstrates that the EFM is responsible for supporting the bulk of the compressive loads in the model. However, it must also be noted that the increased load carrying capacity is also partly due to the stabilization of the fibrils by the EFM and the fibrils carrying load without bending. The fibril elements, by themselves, carry negligible compressive load, but together with the EFM, the stiffness of the model increases immensely. The presence of cross-links enables organization of the fibrils into a network and, with assistance from the

EFM, stabilizing and resisting bending of the fibrils, thus, further increasing the load carrying capacity.

7.3 Effect of cross-link geometry

There are a number of different ways to assign the extent of interfibrillar cross-linking in this mesomodel. We have chosen the simplest configuration of cross-links that divides each typical element in 5 tetrahedra. However, to assess the role played by different types of cross-links (as described in Chapter 6 Sec. 6.3), E_{yy}^{eff} was calculated for the different cross-link geometries as shown in Table 7.3. For this study, κ was set to 2×10^{-15} m^4/N-s and k was set to 5×10^{-3} N/m. All other parameters had the same values as the base model described in Sec. 7.1.

Table 7.3: Different cross-link geometries studied. Refer to Sec. 6.3 for model geometry and Fig. 6.3 for different cross-link orientations.

Geometry	Active Cross-links	k_{xz}	k_{dxz}	k_{dxy}	k_{dyz}
1	None	0	0	0	0
2	All	k	k	k	k
3	Non-diagonal XZ	k	0	0	0
4	All diagonal	0	k	k	k
5	Diagonal XZ	0	k	0	0
6	Diagonal YZ	0	0	0	k
7	Horizontal (all XZ)	k	k	0	0

Fig. 7.6 shows effect of varying the cross-link geometry on E_{yy}^{eff}. These results are summarized in Table 7.4. The extreme values of the effective modulus were found for cross-links geometries in which no cross-links (smallest value) or all cross-links (largest value) were active. With all cross-links active, E_{yy}^{eff} was 40% higher than that calculated for no cross-links. Including any one of the different cross-link geometries increased the effective modulus by at least 8%. For geometry 3, in which only the

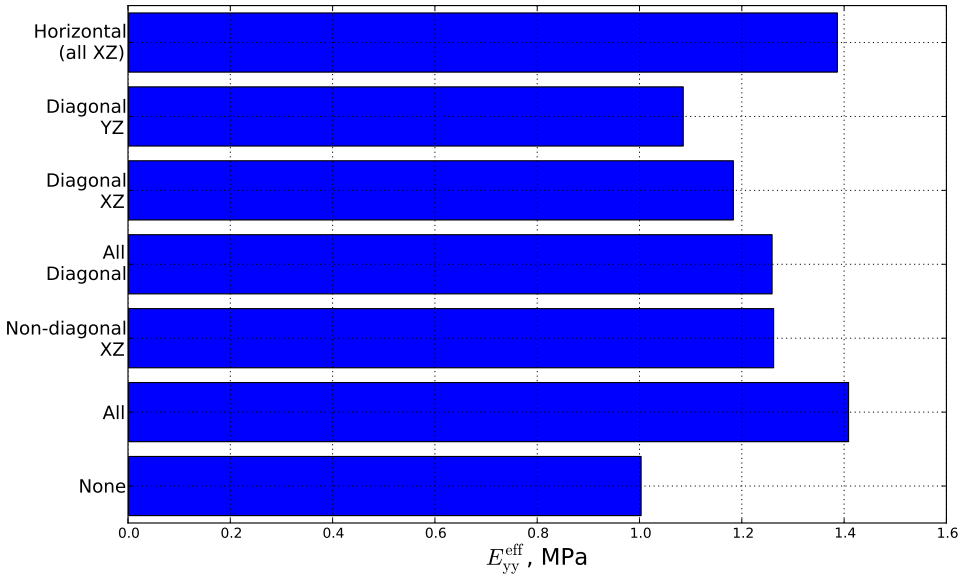

Figure 7.6: Effect of cross-link geometry on E_{yy}^{eff}. Labels indicate cross-links that were active in a simulation. All other cross-links were set to $k \sim 0$.

Table 7.4: Effect of cross-link geometry on the effective modulus in compression

Geometry	Active Cross-links	E_{yy}^{eff}, MPa
1	None	1.003
2	All	1.408
3	Non-diagonal XZ	1.262
4	All diagonal	1.259
5	Diagonal XZ	1.183
6	Diagonal YZ	1.085
7	Horizontal (all XZ)	1.387

in-plane non-diagonal cross-links were active ($k = k_{xz}$), the effective modulus was 26% higher than that without any cross-links. For geometry 4, in which only the diagonal cross-links were active ($k = k_{dxz}$), E_{yy}^{eff} was also 26% higher. For geometry 5, in which only the diagonal XZ cross-links were active, E_{yy}^{eff} was 18% higher. The vertical diagonal cross-links (XY and YZ) resulted in E_{yy}^{eff} that was only 8% higher. When only the horizontal cross-links (cross-links in the XZ plane) were active, E_{yy}^{eff} was calculated to be very close to that calculated when all the cross-links were active (within 2%).

Cross-link geometry influences the effective modulus

From Sec. 7.2 we have seen that the presence of IFLs has a reinforcing effect on the effective modulus, E_{yy}^{eff}. The results from this study reaffirm that result and more importantly demonstrate the geometry of the cross-links used in the mesomodel also influences E_{yy}^{eff}.

The simulated test being performed in this study is compression along the fibril direction (Y). It is expected that the types of cross-links that have a vertical component (DXY, DYZ) will be better able to support the compressive loads by providing stability to the fibrils. The expectation is, therefore, that E_{yy}^{eff} for configurations that include these types of cross-links should be higher than when they are inactive. The result for cross-links of type DXY is not reported as it is expected to be same as that for DYZ due to symmetry. Contrary to our expectation, including cross-links type DYZ resulted in the smallest increase in E_{yy}^{eff} of all the different cross-link geometries. A geometry with only the non-diagonal XZ cross-links resulted in a 26% higher value of E_{yy}^{eff}, while a geometry with all the 'in-plane' cross-links (labeled Horizontal in Fig. 7.6) resulted in a value of E_{yy}^{eff} that was within 2% of that reported for a geometry with all cross-links active.

In order to explain the higher values of E_{yy}^{eff} for geometries with any or all of the

in-plane cross-links vs. those with the 'vertical' cross-links, the fibril configuration at various states of strains was visually inspected for all geometry simulations. The strain at which first fibril bending occurred, ε_{yy}^{bend}, was $\sim 1.8\%$ for cross-link geometry DYZ, while there was no bending of fibrils observed at all for the geometry with in-plane cross-links. This suggests that the geometry of in-plane cross-links is able to provide better support to resist bending, needed for the fibrillar network to carry compressive load. At the same time, it should also be noted that as the EFM deforms in compression, it undergoes the Poisson effect. The geometry of in-plane cross-links, when all active, tends to most resist this lateral expansion of the EFM compared to other geometries, thus, contributing to a higher effective stiffness of the mesomodel.

7.4 Material Parameters

Clearly, the geometry of cross-links used influences the effective modulus in compression. Recognizing this, all studies that followed were performed for two different configurations of the mesomodel. The first configuration had *all* cross-links active and set to the same value k, while in the second configuration cross-links were removed. This was done in order to assess the effect of presence or absence of cross-links with a given parametric variation.

7.4.1 Effect of Fibril Compressive stiffness, E_f^-

The mesomodel had collagen fibrils that have different moduli in tension and compression. In compression along the fibril direction, the fibril compressive modulus plays the dominant role and the value of E_f^- used in the mesomodel will likely play a role in the calculated value of the effective modulus. To assess the effect of E_f^- on the mesomodel, its value was varied in a range found in the literature and used

by other investigators in their FE models of cartilage. The values used varied from $0.2 - 10$ MPa.

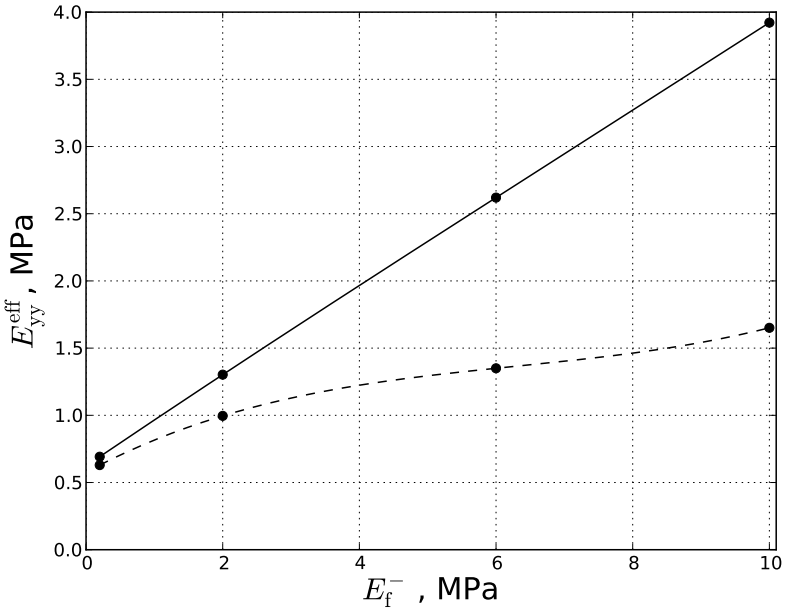

Figure 7.7: Effect of E_f^- on E_{yy}^{eff} in compression at 5% strain. —: With all cross-links active and set to $k = k_m$. - - -: With no cross-links.

Figure 7.7 shows effect of varying the fibril compressive modulus E_f^- on E_{yy}^{eff} for the two configurations–with and without cross-links as described previously. For both configurations, E_{yy}^{eff} increased with increasing E_f^-, however, the difference in the values of E_{yy}^{eff} between the two configurations was much larger at higher values of E_f^- than at lower values. At $E_f^- = 0.2$ MPa, E_{yy}^{eff} calculated for configuration 1 was 9.8% higher than that for configuration 2, while at $E_f^- = 10$ MPa, it was higher by 137.5%.

IFLs enhance the fibril compressive stiffness

From these results it can be seen that the value of calculated E_{yy}^{eff} is sensitive to the fibril compressive modulus, E_f^-, used in the model. Increase in E_f^- results in an increase in E_{yy}^{eff}. This is not only true with the cross-links present, but also when they are removed from the model. The presence of cross-links results in a linear relationship between E_f^- and E_{yy}^{eff}. The result is also consistent with the role of cross-links discussed earlier. The non-linear relationship when cross-links are removed could be explained by bending of fibrils in the absence of cross-links. Also, without cross-links, the rise in E_{yy}^{eff} is considerably less as E_f^- is increased. This suggests that the presence of cross-links results in an amplifying effect on the compressive modulus of the fibrillar network and the extent of amplification depends on the value of E_f^- used.

7.4.2 Effect of EFM modulus, E_m

The EFM plays a vital role in supporting the tissue mainly in compression and shear. The value of the EFM modulus selected in the mesomodel will therefore influence the calculated effective modulus. To assess this influence, the value of E_m was varied in a range of $0.05 - 0.8$ MPa. These values were based on values reported in literature in experiments as well as those used in similar FE models of soft tissue.

Fig. 7.8 shows effect of varying the EFM modulus E_m on E_{yy}^{eff} with all cross-links active and set to the same value $k = 1 \times 10^{-3}$ N/m. For the four values of E_m studied–0.05, 0.1, 0.5 and 0.8 MPa – the corresponding values of k_m were 0.02, 0.01, 2×10^{-3} and 1.25×10^{-3} N/m. The effective modulus followed the EFM modulus, i.e., E_{yy}^{eff} increased with increasing E_m.

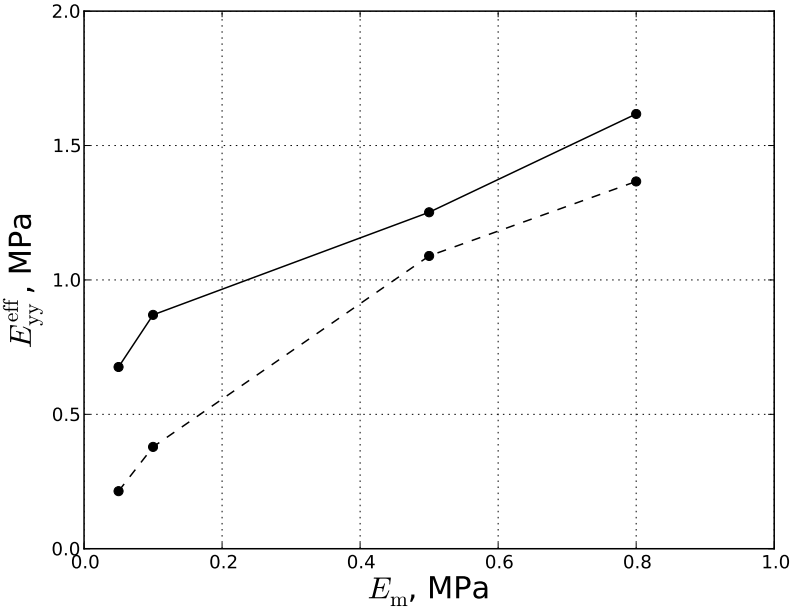

Figure 7.8: Effect of E_m on E_{yy}^{eff} in compression at 5% strain. —: With all cross-links active and set to $k = 1 \times 10^{-3}$ N/m. - - -: With no cross-links.

The effect of varying the EFM modulus was as expected. By increasing E_m, E_{yy}^{eff} increased. The non-linearity of the curves is quite bewildering, but, could be attributed to bending of fibrils at different strains for different values of E_m. A visual inspection of the deformed fibril configuration for simulations for this study showed that the strain at which the first bending of fibrils occurred, ε_{yy}^{bend}, gradually increased as E_m increased. This was true for simulations with or without cross-links. Post bending the load support mechanism could be quite complex and likely non-linear. Thus, although all components in the mesomodel are linear elastic, fibrils in the fibrillar network bending at different strains corresponding to different values of E_m could be the source of non-linearity.

7.4.3 Effect of EFM Poisson's ratio, ν_{m}

The Poisson's ratio is another mechanical property of the EFM that is likely to directly affect the overall modulus. It will also likely play an important role in the poroelastic response of the tissue. The Poisson's ratio was varied in the range $0.2 - 0.5$. The mesomodel showed excessive distortion in the EFM elements as the EFM was made more compressible (decreasing ν_{m}). This effect was not observed when the initial pore pressure was removed. Thus, for the purpose of this study, the initial pore pressure, p, was set to zero.

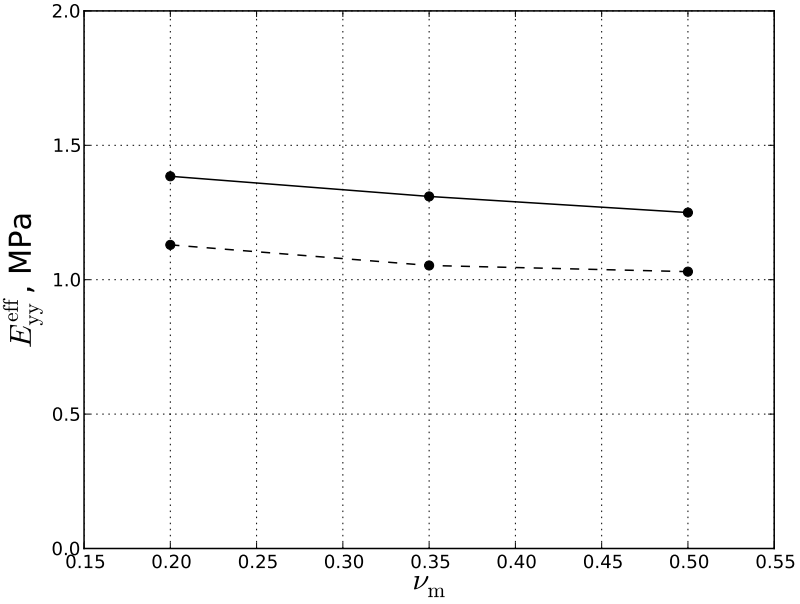

Figure 7.9: Effect of ν_{m} on E_{yy}^{eff} in compression at 5% strain and initial value of $p = 0$. —: With all cross-links active and set to $k = 1 \times 10^{-3}$. - - -: With no cross-links.

Fig. 7.9 shows effect of varying the EFM Poisson's ratio, ν_{m}, on E_{yy}^{eff} for the two configurations of cross-link geometry. Increasing ν_{m} resulted in a decrease in E_{yy}^{eff}. The value $E_{yy}^{eff} = 1.38$ at $\nu_{\mathrm{m}} = 0.2$ was $\sim 10\%$ higher than $E_{yy}^{eff} = 1.25$ at $\nu_{\mathrm{m}} = 0.5$

for the model with cross-links included. When cross-links were removed, $E^{\text{eff}}_{\text{yy}} = 1.13$ at $\nu_{\text{m}} = 0.2$ was also $\sim 10\%$ higher than $E^{\text{eff}}_{\text{yy}} = 1.03$ at $\nu_{\text{m}} = 0.5$.

7.4.4 Initial Pore Pressure, p

The initial pore pressure sets up the initial stresses in various components of the tissue mesomodel – tension in the fibrils and compression in the EFM. Its role on the effective modulus was assessed by varying p in the range $0.04 - 4$ MPa based on values reported by Basser *et al.* [135] and Chahine *et al.* [15] for articular cartilage.

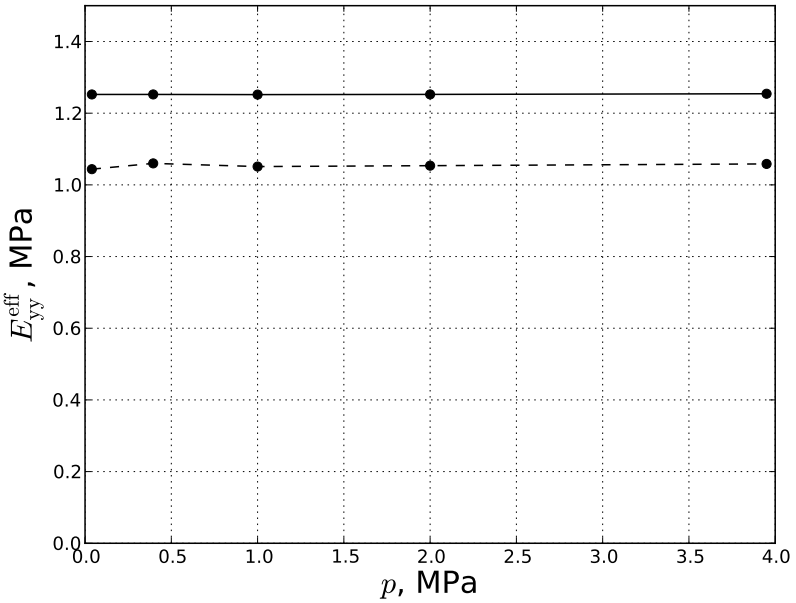

Figure 7.10: Effect of initial p on $E^{\text{eff}}_{\text{yy}}$ in compression at 5% strain. —: With all cross-links active and set to $k = 1 \times 10^{-3}$ N/m. - - -: With no cross-links.

Figure 7.10 shows effect of varying the initial pore pressure, p, on $E^{\text{eff}}_{\text{yy}}$ for the two configurations. Change in p had a negligible change ($< 1\%$) in the calculated effective modulus with or without cross-links.

The initial pore pressure did not have any effect on the effective modulus in compression likely due to the incompressibility of the matrix. When the EFM was made more compressible by decreasing ν_{m}, it resulted in excessive deformation in the EFM in our simulations. Therefore the variation of the initial pore pressure at values of ν_{m} other than 0.5 could not be tested.

For all studies in which initial pore pressure was applied and the model allowed to equilibrate the fibrillar network was in tension while there were compressive stresses in the EFM. However, the stresses in the fibrils were very low ($\sim 10 - 50$ Pa) compared to the elastic moduli of the components which were of the order of MPa. As a consequence of the large tensile modulus of the fibrils, E_{f}^{+}, the tensile strain produced in the fibrils was negligibly small ($\sim 10^{-8}$). These values are low enough to be in the error tolerance region of ABAQUS. To verify that these values were realistic, E_{f}^{+} was reduced to be equal to E_{m} ($\sim$ 1000 times less). For this low value of E_{f}^{+}, the tensile strains in the fibrils were three orders larger ($\sim 10^{-5}$) but still very small. Also, once the initial pore pressure had been applied, there was negligible ($< 1\%$) increase in the pore pressure in the mesomodel with the applied strain (5%). Parametric study of initial pore pressure indicates that it does not have any significant effect on the effective modulus in compression of this mesomodel. A closer look at the mechanism of pore pressure and the pre-stress it produces in the model components is required. This is discussed in the following section.

7.4.5 Mechanism of Pre-stress due to initial pore pressure

As discussed in the previous section, the goal for this study is to understand the effect pre-stress in the mesomodel–induced due to the initial pore pressure–has on the model response in compression. Understanding the mechanism by which the pre-stress is overcome will aid in determining the role of the initial pore pressure in

this model in carrying compressive load.

In the previous section, we discussed the very low tensile strains produced in the fibrils post application of the initial pre-stress due to their high tensile modulus. To facilitate larger strains, the fibril tensile modulus, E_f^+, was reduced by 10 times to 15 MPa for this study. Study of previous simulations revealed that the pre-stress had been completely overcome within the first 0.1% of applied strain. Therefore, a compressive strain of 0.1% was applied at the same rate (0.2%/s) post equilibrium after application of p.

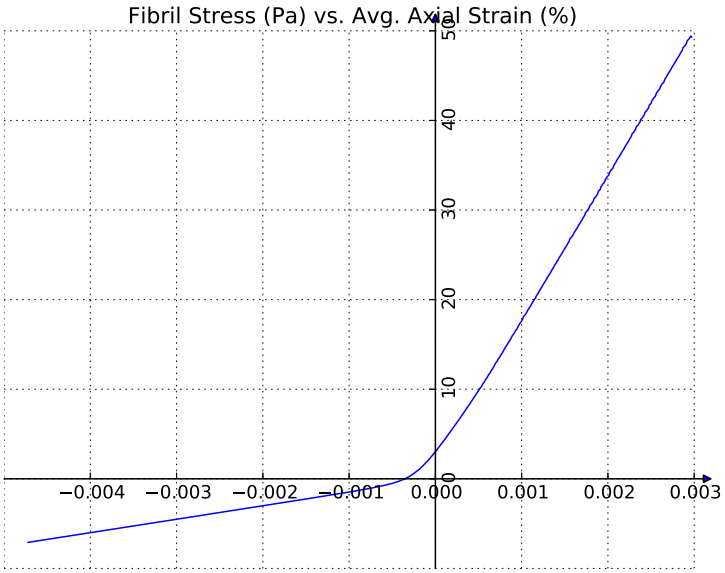

Figure 7.11: Fibril Stress vs. Axial Strain (%) in the pre-stress zone in compression. The pre-stress is overcome at a negligibly small compressive strain.

Figure 7.11 shows the variation of the fibril stress with the average axial strain for this study. In this plot, stresses and strains shown are positive. Recall that each fibril assembly is a combination of a truss element and a beam element. The

fibril stress shown is the total net fibril stress, which equals the stress in the fibril truss element plus the stress in the fibril beam element, summed over all fibril assemblies. Equilibrium at the initial pore pressure resulted in an average tensile strain of $\sim 0.003\%$ and an average tensile pre-stress of ~ 50 Pa in the fibrils. As compression was applied, the pre-stress linearly reduced until it was overcome. The strain in the fibrils at this point was $\sim 0.0004\%$. Beyond this point, compressive stresses increased linearly with strain as expected, but, the slope of the curve reduced by almost 90%.

The axial tensile stress and strain in the fibril elements, as a result of equilibration with the initial pore pressure, depend on the fibril tensile modulus, E_{f}^{+}, used in the simulation. Reducing E_{f}^{+} by 90% of that used in the base model produced tensile stresses of the order of Pa and strains of the order of $10^{-5}\%$, which are negligibly small compared to the order of stresses and strains that occur in most tissues. If a realistic fibril tensile modulus were used these values will be even lower.

As compression proceeded post initial equilibrium, the tensile pre-stress in the fibrils decreased linearly and eventually reached zero. The strain at which the pre-stress was overcome was not zero. The initial pore pressure, through the pre-stress mechanism, enabled the fibrillar network to withstand a small compressive strain. It resulted in a shift of the stress-strain curve to the left, albeit by a very small amount.

Beyond the pre-stress the stress-strain curve is linear, but, with a much smaller slope as compared to the part of the curve where pre-stress prevailed. This can be explained as follows. In the pre-stress zone where the fibril stress is tensile, much of the load is carried by the fibrils on account of their very high tensile modulus, $E_{\mathrm{f}}^{+} = 15$ MPa in this simulation. Consequently, the slope of the curve is larger in

this region of the plot. As the pre-stress is overcome, and compressive stresses set in, much of the load is now supported by the EFM. From Sec. 7.2 we have seen that the fibrils by themselves carry negligible compressive loads. Due to its very low elastic modulus, $E_{\mathrm{m}} = 0.5$ MPa in this simulation, the EFM offers far less resistance in compression than that of the fibrillar network in tension. Once the pre-stress is overcome in the fibrils, the overall stiffness reduces dramatically, and therefore a flatter response is seen in the plot for this zone.

The results from the parametric study of initial pore pressure showed that it did not influence the effective modulus in compression. The results from this study show that the initial pore pressure resulted in a negligibly small tensile stress in the fibrillar network that was overcome instantaneously in compression. Until a pressure equal to the prestress is applied, fibrils create pseudo-pressure. During this pressure range, the stiffness of the body is dictated by the fibril stiffness. Hence, prestress causes high stiffness for small stiffness. One can expect that removing the initial pore pressure from this mesomodel ($p = 0$) will not change, for practical purposes, the results from these parametric studies or the conclusions drawn from those results.

7.4.6 Effect of EFM Permeability, κ

The permeability of the EFM, κ, is one of the poroelastic parameters that may influence the effective elastic modulus. The effect of κ on $E_{\mathrm{yy}}^{\mathrm{eff}}$ was studied by varying κ over a range of two orders of magnitude. The values chosen were: $2 \times [10^{-14}, 10^{-15}, 10^{-16}]$ m^4/N-s, based on the commonly reported range of 10^{-14}–10^{-16} m^4/N-s by various investigators. Recall that the loading is carried out at a rate of 0.2% strain/sec.

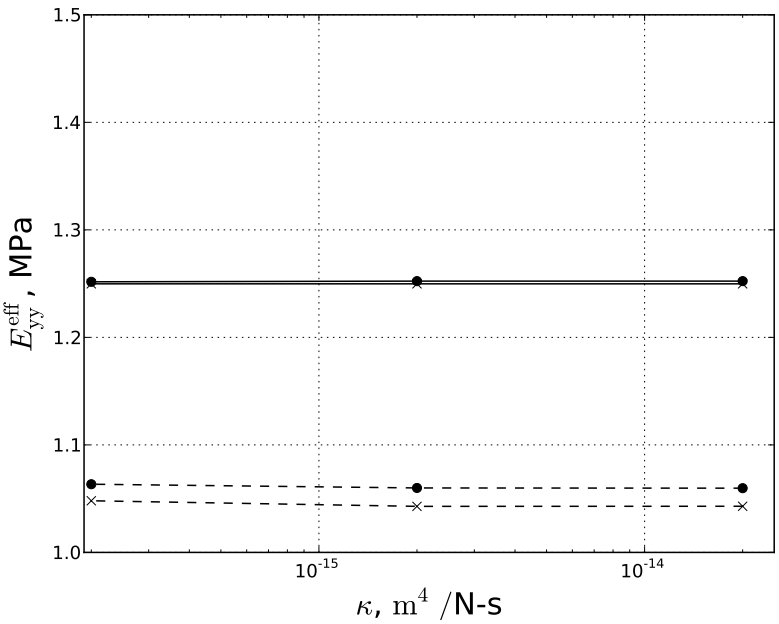

Figure 7.12: Effect of κ on E_{yy}^{eff} in compression at 5% strain at the rate of 0.2% strain/sec. Variation at different p holding $\nu_m = 0.5$. Circle: $p = 0.4$, cross: $p = 0$. —: With all cross-links active and set to $k = 3.5 \times 10^{-3}$. - - -: With no cross-links.

From Secs. 7.4.4 and 7.4.5, we have seen that the initial pore pressure does not affect E_{yy}^{eff} and will likely not affect the influence of other model parameters on E_{yy}^{eff}. The parametric study on κ was, therefore, carried out in two parts. In the first part of the study (Fig. 7.12), ν_m was held constant at 0.5 and κ was varied for $p = 0.4$ MPa (circles) and $p = 0$ MPa (crosses).

The permeability of the EFM had no effect on the effective modulus at these values of ν_m and p. When cross-links were included (solid lines), the two curves for different values of p overlap exactly. When cross-links were removed (dashed lines), E_{yy}^{eff} was slightly higher ($\sim 1.5\%$) at $p = 0.4$ MPa than at $p = 0$.

The variation in permeability of the EFM can influence the effective modulus in two ways: (1) affecting the pore fluid flow, and (2) affecting the deformation of the solid material that forms the skeleton of the EFM. In this study, however, with $\nu_m = 0.5$, the material is incompressible. In all our simulations, there was negligible change in the pore pressure at 5% compression from the initial pore pressure. This indicates that the fluid exudation during compression was not enough to cause any significant change in the pore pressure. Also, for this model, the characteristic gel diffusion time in confined compression can be used and is calculated to be $T_g = \sim 10^{-3}$, which implies that the flow effect is over in a very short time. These observations lead us to believe that lowering ν_m may result in some effect on the effective modulus by varying κ.

In the second part of the study (Fig. 7.13), the initial pore pressure was held constant at $p = 0$ and κ was varied for the same values as above for $\nu_m = 0.5$ (crosses) and $\nu_m = 0.2$ (squares).

When cross-links were included, κ had no effect on E_{yy}^{eff}. In the absence of cross-links, κ had no effect on E_{yy}^{eff} at $\nu_m = 0.5$ (crosses). However, at $\nu_m = 0.2$, increasing κ by two orders of magnitude resulted in a $\sim 4\%$ increase in the corresponding value

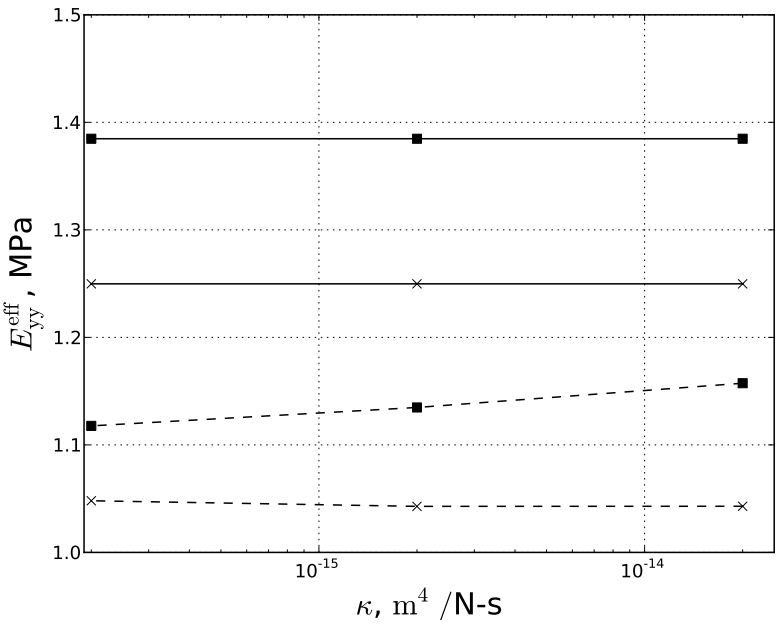

Figure 7.13: Effect of κ on E_{yy}^{eff} in compression at 5% strain at 0.2% strain/sec. Variation at different ν_m holding $p = 0$. Cross: $\nu_m = 0.5$, square: $\nu_m = 0.2$. —: With all cross-links active and set to $k = 3.5 \times 10^{-3}$. - - -: With no cross-links.

of E_{yy}^{eff}.

These results are quite confounding and indicate that κ had an effect on E_{yy}^{eff} only when there were no cross-links, the EFM was compressible and initial pore pressure was zero. In this case E_{yy}^{eff} increased with increase in κ. With a higher κ, the fluid inside the model can flow out readily and result in higher E_{yy}^{eff} as a consequence of solid-solid interaction of the EFM skeleton material. Even at this configuration, the increase in E_{yy}^{eff} due to increase in κ was only about 4% and may not be significant. Results from Sec. 7.2 show that with addition of cross-links, no matter what the geometry, for sufficiently high k (compared to k_m), E_{yy}^{eff} increased at least by 8%. In those simulations, however, the initial pore pressure was non-zero and ν_m was 0.5. Intuitively, it is expected that addition of cross-links to the configuration under consideration ($\nu_m = 0.2$, $p = 0$, no cross-links) should produce a similar trend as without cross-links. However, the results show adding cross-links did not affect E_{yy}^{eff} with increasing κ. The matrix, which is compressible in this study, along with the cross-links is likely affecting the model in some unexpected way, so that the end result is no change in E_{yy}^{eff}. A closer look at the permeability of the matrix is needed to understand such mechanisms.

7.4.7 Fibril volume fraction, v_f

The fibril volume fraction, v_f, is related to the fibril diameter, D, and the interfibrillar distance, d, through Eq. (6.9). Thus, the effect of v_f on the effective modulus was assessed by performing two studies in which either of D or d was held constant while the other was varied so that the v_f was equal to 0.1, 0.256 and 0.4. The fibril volume fraction varies from the surface zone to the deep zone and is generally reported in this range.

Fibril diameter, D

In the first study, v_f was varied by varying the fibril diameter while holding the interfibrillar distance constant. The constant value of $d = 70$ nm was used and values of D corresponding to the above mentioned values of v_f were 25, 40 and 50 nm.

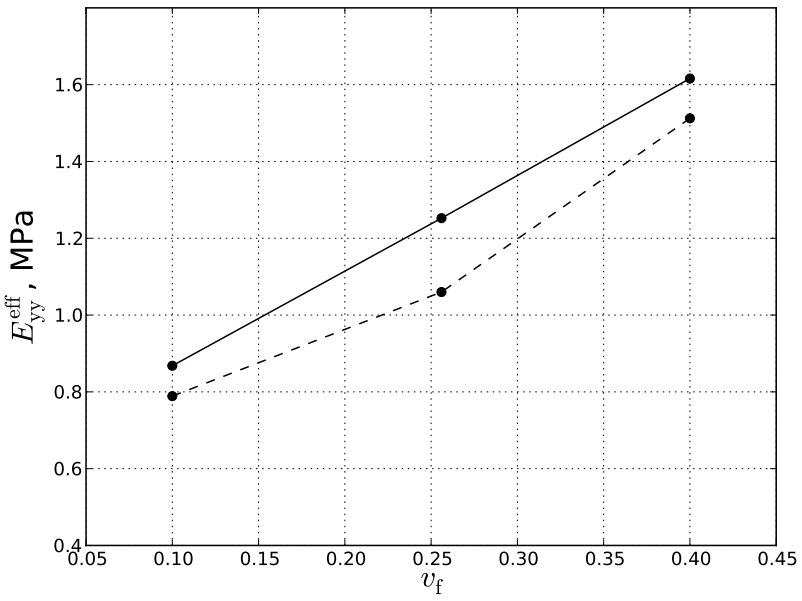

Figure 7.14: Effect of varying v_f on E_{yy}^{eff} in compression at 5% strain by varying the fibril diameter D and holding the interfibrillar distance d. —: With all cross-links active and set to $k = 1 \times 10^{-3}$. - - -: With no cross-links.

Fig. 7.14 shows effect of varying the fibril volume fraction, v_f, on E_{yy}^{eff} for the two configurations achieved by varying the fibril diameter, D, while maintaining the interfibrillar distance, d, constant. The effective modulus followed the fibril diameter, i.e., E_{yy}^{eff} increased with increase in D and decreased when D was decreased. A 37.5% reduction in D ($D = 25$ nm, $v_f = 0.1$) from the base value ($D = 40$ nm, $v_f = 0.256$) resulted in a 30% decrease in E_{yy}^{eff} whereas a 20% increase in D ($D = 50$

nm, $v_f = 0.4$) resulted in a 29% increase in E_{yy}^{eff}.

In this mesomodel, as v_f is directly proportional to D, increasing D increased v_f thereby increasing E_{yy}^{eff}, and decreasing D decreased v_f consequently reducing E_{yy}^{eff}. This trend should not, and does not, depend upon inclusion or exclusion of cross-links. These results are in agreement with the general composites theory that the effective modulus of an unidirectional fiber-reinforced composite material along the fibril direction increases by increasing the volume fraction of the fibers.

Interfibrillar distance, d

In the second part of the study, the fibril diameter was held constant and v_f was varied by changing the interfibrillar distance. $D = 40$ was held constant while values of d used were 56, 70 and 112 nm corresponding to the v_f values stated above.

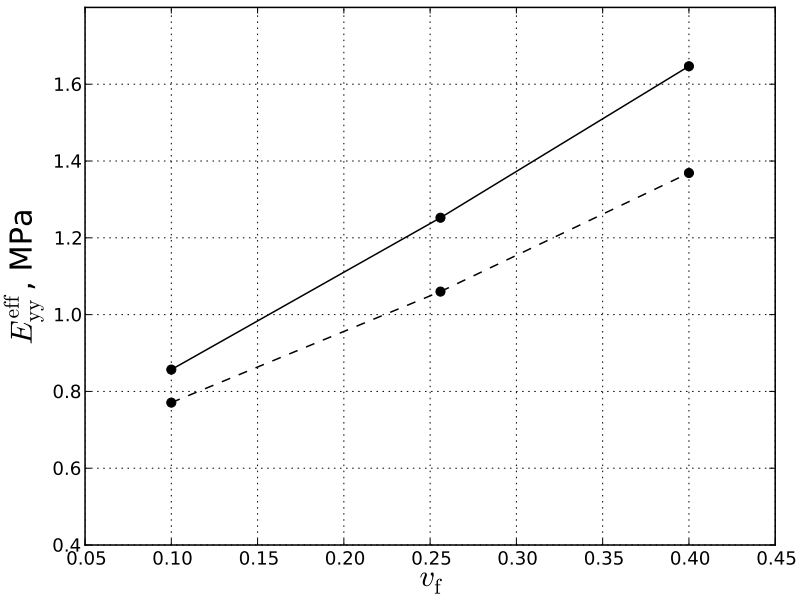

Figure 7.15: Effect of varying v_f on E_{yy}^{eff} in compression at 5% strain by varying the interfibrillar distance d and holding the fibril diameter D. —: With all cross-links active and set to $k = 1 \times 10^{-3}$. - - -: With no cross-links.

Fig. 7.15 shows effect of varying the fibril volume fraction, v_{f}, on $E_{\mathrm{yy}}^{\mathrm{eff}}$ for the two configurations achieved by varying the interfibrillar distance, d, while maintaining the fibril diameter, D, constant. The effective modulus was inversely related to the interfibrillar distance, i.e., $E_{\mathrm{yy}}^{\mathrm{eff}}$ increased with decrease in d and decreased when d was increased. A 20% reduction in d ($d = 0.056$, $v_{\mathrm{f}} = 0.4$) from the base value (0.07 nm, $v_{\mathrm{f}} = 0.256$) resulted in a 29% increase in $E_{\mathrm{yy}}^{\mathrm{eff}}$ whereas a 60% increase in d resulted in a 27% increase in $E_{\mathrm{yy}}^{\mathrm{eff}}$.

These results are quite as expected, since v_{f} is inversely proportional to d. Thus, increasing d moves the fibrils further apart consequently reducing v_{f}, while decreasing d implies fibrils are closer together, thereby increasing v_{f}. The effects of changing d on $E_{\mathrm{yy}}^{\mathrm{eff}}$ are also in agreement with the general composites theory.

7.5 Application to Articular Cartilage

In this section, application of the mesomodel to articular cartilage is discussed. The goal of this study was to assess the effect of removing the cross-links on the effective modulus, $E_{\mathrm{yy}}^{\mathrm{eff}}$, assuming reasonable values for AC for model parameters for the simulated compression test. Most of the values used in the parametric study above were already in their respective ranges reported in literature, except for the cross-link stiffness, k and the Poisson's ratio of the EFM, ν_{m}. For this 'best-guess' parameter simulation, $k = 0.033$ N/m (obtained from Liu *et al.* [133]) and $\nu_{\mathrm{m}} = 0.2$ (obtained from Chapter 4) were used. The cross-link geometry used consisted of all cross-links with the same stiffness, k. Also, from Secs. 7.4.4 and 7.4.5, we have seen that the initial pore pressure, p, does not affect in any way to the value of $E_{\mathrm{yy}}^{\mathrm{eff}}$. The initial pore pressure was, therefore, set to $p = 0$ for this study. Table 7.5 lists the values of the parameters used in this 'best-guess' study.

Table 7.5: Values used for mesomodel parameters for simulating compression test along Y direction of articular cartilage.

E_{m}	0.5	MPa
E_{f}^{+}	150	MPa
E_{f}^{-}	2	MPa
ν_{m}	0.2	
κ	2.1×10^{-15}	m^4/N-s
D	40	nm
k	0.033	N/m
v_{f}	0.256	
d	70	nm
d_{v}	70	nm

At 5% strain, with all cross-links included, the effective modulus for the model was $E_{\mathrm{yy}}^{\mathrm{eff}} = 2$ MPa. When the cross-links were removed, $E_{\mathrm{yy}}^{\mathrm{eff}}$ reduced to 1.13 MPa. Thus, with reasonable values for parameter models, removing the cross-links reduced the effective modulus by 43%.

It is important to note that these results are for simulations at the mesoscale. A multi-scale model is needed to relate these results from the mesoscale to the macroscopic scale, the scale at which general tissue biomechanical experiments are designed. If this is achieved, studies can be designed to utilize a combination of biomechanical testing and biochemistry experiments that alter the interfibrillar cross-linking in articular cartilage. Mechanical properties, similar to the effective modulus in this study, can be tested before and after the biochemistry is altered and such studies can then use results from the current study as benchmark to assess if there are any effects on the interfibrillar cross-links within the tissue.

7.6 Summary and Conclusions

- IFLs in articular cartilage have an important role in its mechanical response. Presence of IFLs increases the effective modulus in compression at the mesoscale (Fig. 7.2). The higher the value of the cross-link stiffness the later is the first occurrence of bending in fibrils (Fig. 7.3). This suggests that *IFLs help increase the effective modulus by preventing bending of the fibrils and thereby increasing their load carrying capacity.*

- From Figs. 7.2 and 7.5 the following observations were made. The fibrils carry negligible compressive loads by themselves due to bending. But in the presence of IFLs, the fibrils were able to carry 60 times more. The EFM on the other hand, carried approximately 43% of the load carried when all components were present. In presence of cross-links the effective modulus increased by only 14%. This suggests that *presence of IFLs affects both the EFM as well as the fibrils, however, their effect is much larger on the fibrils compared to the EFM.*

- Inspection of deformed fibril configuration at the same strain level for different values of cross-link stiffness revealed that as the cross-link stiffness increased from zero to the stiffness value reported in the literature, the deformed fibril configuration changed from a haphazard, uncoordinated deformation accompanied with fibril bending to a coherent, organized deformation without fibril bending (Fig. 7.4). This demonstrates that *the presence of IFLs helps organize the fibrils into a network and imparts some stability to the network by preventing fibril bending.* With all components included in the mesomodel, first occurrence of fibril bending was observed at higher strains when the EFM was included. The same effect was observed when the cross-links were removed.

This suggests that *the EFM also contributes to fibril organization and stability*. Presence of IFLs results in a larger difference in fibril organization and stability than the presence of the EFM suggesting that the IFLs are more responsible in performing these functions than the EFM.

- The effective modulus in compression is sensitive to the cross-link geometry used in the mesomodel (Fig. 7.6). A manual inspection of the deformed fibril configuration for various cross-link geometries revealed that the effective modulus was higher for those geometries in which organized fibril bending was observed at higher strains. The cross-link geometry with all cross-links in a plane perpendicular to the fibril direction came very close to producing the same effective modulus as a geometry with all cross-links. It should also be noted that this 'in-plane' geometry most resists the EFM Poisson effect. From this we can conclude that *the geometry which most prevents fibril bending and resisting the matrix Poisson effect will likely result in a higher effective modulus.*

- The effective modulus in compression is also sensitive to the fibril compressive stiffness (Fig. 7.7). An increase in the fibril compressive modulus resulted in an increase in effective modulus. The effect was more pronounced when cross-links were included in the model at larger values of the fibril compressive modulus. This leads to the conclusion that *the value of the fibril compressive modulus used in the mesomodel is critical as the presence of IFLs enhances the compressive modulus of the fibrillar network and this enhancement is highly sensitive to the value of the fibril compressive modulus.*

- The effective modulus in compression is also sensitive to the EFM modulus used (Fig. 7.8). As expected, effective modulus increases with increasing EFM

modulus. At lower values of the EFM modulus, first occurrence of fibril bending was observed at lower strains. Post-bending the load support mechanism is quite complex and likely non-linear. This is likely the source of non-linearity observed in the relationship between the effective modulus and the EFM modulus.

- The initial pore pressure did not have any effect on the effective modulus (Fig. 7.10). Using values from literature for the initial pore pressure produced the desired effect of tension in the fibrillar network and compression in the EFM at initial equilibrium. However, the stresses and strains produced were several orders of magnitude smaller than the corresponding elastic moduli of the components and the typical dimensions of the mesomodel. This was a consequence of the very large tensile modulus of the fibrils. Reducing the fibril tensile modulus produced larger stresses and strains, albeit still orders of magnitude lower than the stiffness of the model components.

- The fibril volume fraction directly affects the effective modulus and is in agreement with the general composites theory. Changes in the fibril diameter are mirrored in the effective modulus – increasing/decreasing the fibril diameter results in a corresponding higher/lower effective modulus. Changing the interfibrillar distance produces an opposite effect on the effective modulus, i.e., increasing/decreasing the interfibrillar distance results in a corresponding lower/higher effective modulus.

Application of the mesomodel to articular cartilage by choosing reasonable values for model parameters obtained from literature showed that removing the cross-links resulted in a 43% drop in the effective modulus. Thus, at the mesoscale, the cross-links seem to play a mechanical role in supporting the compressive loads in the articular cartilage.

Part IV

Summary and Outlook

Summary and Outlook

In this thesis, the primary objective is to understand the mechanical response of AC using FE modeling in ABAQUS. This is done at two different scales. For the small strain AC response studied the FE models are simple (linear elastic components), yet include important features such as flow-dependent and flow-independent processes (poroelasticity, viscoelasticity) at the macroscale and time-dependent behavior (poroelasticity of the EFM) and bilinear fibrils at the mesoscale.

FE Continuum Modeling of AC

At the macroscopic scale, the contact problem of indentation of AC is studied using a continuum model combined with nanoindentation experiments. There are major challenges to overcome in order to use PVE models that include both PE flow-dependent time dependency and VE flow-independent time dependency. For instance, there are too many parameters to fit, resulting in questions of uniqueness of the fit parameters. Additionaly, the time ranges of the PE and VE processes overlap in most experimental test conditions. The method to separate the PE and VE processes for better fit and uniqueness of parameters proposed by Huang *et al.* [73] involves tensile test of a thin strip of the tissue. This cannot be done for small tissue volumes such as mouse cartilage. These obstacles are overcome by using

two indenters - one small enough so that the characteristic gel diffusion time is negligibly small and the other sufficiently large to probe flow-dependent processes with the test conditions being used. A summary that includes the principal contributions of this part of the thesis is as follows:

- Indentation tests are performed on AC obtained from mouse knee joints with two different sized flat-ended conical indenters with flat-end tip diameters 15μm and 170μm. Stress relaxation tests are performed to study the time-dependent response.

- A FE model of the indentation of a PVE material with a rigid flat-ended conical indenter is developed. AC is modeled as a homogeneous isotropic PVE/VE layer bonded to a rigid and impermeable substrate (underlying bone) being indented by a rigid and impermeable indenter.

- A parametric study of permeability is performed for indentation with the two indenters using the FE model for a PE material. Results show that permeability does not affect the stress response predicted for the 15μm indenter. In contrast, there is a distinct change in the stress relaxation predicted for the 170μm indenter.

- An inverse algorithm program is implemented along with the FE model to extract the model parameters from the indentation experiments. The FE indentation model simulates the forward problem and the parameters are extracted using the SIMPLEX algorithm to maximize the coefficient of determination between the experimental and FE predicted data.

- A method for fitting parameters in a PVE model of AC in the mouse is presented. Indentation data from the smaller indenter is first used to fit the viscoelastic parameters, on the basis that for this tip size the PE response

is negligible. These parameters are then used to fit the data from a second indenter of much larger diameter for the PE parameters, using the viscoelastic parameters extracted from the data from the smaller indenter. The ability to separate the flow-independent and flow-dependent processes both experimentally and theoretically for small tissue volumes make the two indenter approach very useful.

Mesoscale Modeling of AC

At the mesoscale, the inhomogeneity of AC structure and composition cannot be neglected. For this purpose, a continuum model faces limitations and modeling of the micro-constituents becomes important. Most of the fibril-reinforced models for AC behavior in literature use some homogenization procedure and are therefore continuum models, except for the spring-based models in which fibrils are modeled as springs. The microstructural model of AC by Schwartz *et al.* [86] includes the fiber-matrix bonding. However, none of the fibril-reinforced models reviewed account for the IFLs. The IFLs in AC are not well characterized and are hypothesized to be the "glue" between the collagen fibrils. It is also thought that these IFLs get damaged at the onset of OA. It is difficult to evaluate IFLs experimentally, so theoretical models are a useful way to do this. In the final part of the thesis, the focus is to understand the role of IFLs seen in most collagenous tissues. A 3D model of AC meso-structure based on the major micro-constituents of AC at this scale – collagen fibrils, EFM and IFLs – is developed and studied. A summary that includes the principal contributions of this work is as follows:

- The collagen fibrils are unidirectional and exhibit characteristic bilinear rope-like behavior. This is achieved by modeling collagen fibrils as a superposition of two types of elements - a tension only truss element with a modulus equal to

the high tensile modulus (E_{f}^{+}) reported for collagen fibrils, and a beam element with a very low modulus (E_{f}^{-}) resulting in a very low bending modulus. The EFM is modeled as a linear elastic incompressible porous material saturated with the interstitial water. The intrinsic viscoelasticity of the EFM is neglected for simplicity.

- The IFLs are modeled as simple springs. The crosslink stiffness is obtained from molecular studies on decorin, a molecule that is believed to form crosslinks in AC via other PG molecules. For simplicity, the number of crosslinks in a typical element is kept to a minimum while retaining the stability of the structure. As far as we know, the mesomodel developed in this work is the first fibril-reinforced mesomodel of AC that includes IFLs.

- The prestress in the fibril network and the EFM due to swelling is included by allowing the model to equilibrate to the initial equilibrium pore pressure reported for osmotic swelling studies on human cartilage. This results in tension in the fibril network and compression in the EFM at equilibrium.

- Homogeneous boundary conditions are most appropriate for the study of AC mesomodel due to the inhomogeneity of the tissue. Simulated compression tests along the fibril direction are conducted for a parametric study of the model parameters as compression is most relevant to AC mechanics.

- Results show that the effective compressive modulus of the mesomodel is significantly higher in the presence of IFLs. This is due to prevention of early bending of fibrils due to the IFLs, thereby increasing their load carrying capacity. The presence of IFLs helps organize the fibrils into a network and imparts some stability to the network by preventing early fibril bending.

- The effective modulus in compression is sensitive to the crosslink geometry

used in the mesomodel. The in-plane crosslinks contribute the most to stabilizing the fibril network as they provide the most resistance to the EFM Poisson effect and preventing early bending in fibrils, resulting in a higher effective compressive modulus.

- The effective compressive modulus is sensitive to other model parameters and its variation with them is as intuitively expected. The presence of IFLs enhances the compressive modulus of the fibril network (E_{f}^{+}), consistent with earlier observations. A similar sensitivity to the EFM modulus and the fibril volume fraction is seen.

- The initial pore pressure and the permeability of the EFM do not have significant effect on the effective compressive modulus. Thus, one can expect that removing the initial pore pressure from the mesomodel will not produce any significant changes in the results of the parametric study.

Future Work and Outlook

The mesomodel of AC shows that with a best guess set of values chosen for the model parameters for AC shows that removing the crosslinks results in a 43% drop in the effective compressive modulus. Thus, at the mesoscale, the crosslinks seem to play a mechanical role of providing stability to the fibril network thereby increasing its load carrying capacity. How this translates over to the macroscopic tissue level remains to be answered.

Mesoscale models are developed with a long term goal of parsing information at the smaller scale to the macroscopic properties at the larger scale in order to relate observed macro behavior to the micro-constituents of the mesomodel. The mesomodel cannot be used as an RVE with periodic boundary conditions due to the inhomogeneity of AC. Even by increasing its size to include more spatial varitions,

the mesomodel still cannot be treated as an RVE. However, the mesomodel developed here can be used in conjunction with a macroscopic model, such as the PVE model of AC discussed in this thesis, in a multi-scale simulation (e.g., [141]) that can relate the mesoscale effective properties to the macroscopic mechanical response of the tissue. For this purpose, however, one needs to examine the model in not just compression, but also in other test geometries beyond compression.

The inhomogeneity of AC and the variation in its structure and composition at various depths needs to be represented as accurately as possible while simultaneously keeping computation costs at a minimum. In the context of this model, the fibril orientation and volume fraction are important variations along AC depth as discussed in Chapter 2. In this thesis, we have only looked at unidirectional fibrils that are vertical to the plane of loading. This is an appropriate model of the mesostructure observed in the deep zone of AC. With random orientation in the middle zone and fibrils parallel to the loading plane at the surface, the behavior is likely to be different in those zones. Such variations can be studied by parametric studies similar to what has been done here for compression in the Y direction. Identifying crosslink sites on the randomly oriented fibrils and determining which fibrils interact can be accomplished computationally. With unidirectional fibrils the FEA mesh is accomplished by having the fibrils share nodes with the EFM. This cannot be done easily with random fibril orientation and meshing of the FE model will be a major challenge. Using simultaneous Eulerian and Lagrangian descriptions, i.e., modeling the EFM as a fluid and the fibrils as solids, although not trivial, may help address this issue. However, the appropriateness of this approach needs to be examined carefully.

The constitutive behavior of the micro-constituents of the mesomodel can be changed to 'upgrade' the model to the non-linear regimes. This includes hyperelastic formulations for the fibril and EFM behavior. Also, time-dependent behavior in AC has been well characterized as being flow-dependent as well as flow-independent. In this study, we have neglected the flow-independent time dependency. We also see from the parametric study that both flow-dependent properties - initial pore pressure and permeability - did not have a significant effect on the effective modulus. However, at the macroscopic level, our PVE model of indentation, clearly shows that flow-dependent processes are significant, especially with the larger 170 μm indenter. This suggests that the flow-dependent processes in AC may be a macroscopic phenomenon. Or, it may be that our mesomodel is smaller than the scale at which flow-dependent processes influence the mechanical response. Thus, in a multi-scale simulation, flow-independent processes can be restricted to the microstructure while flow-dependent processes assigned to the macrostructure. However, a closer look at the effect of viscoelasticity at the mesoscale is needed before proceeding toward multi-scale mechanics.

Finally, the IFLs used in this model are linear springs. Non-linear springs or other methods to simulate molecular interactions in a mechanical way seem to be the next logical 'upgrade' to the crosslinks. Another way would be to introduce one more hierarchical level of molecular dynamics simulation for the crosslink mechanical behavior which can pass on information to the mesoscale and so on. However, this will come with sufficient computation expense and one needs to evaluate the cost-benefit in using such a model.

Part V

Bibliography

Bibliography

[1] Joseph A. Buckwalter, Thomas A. Einhorn, and Sheldon R. Simon, editors. *Orthopaedic basic science : biology and biomechanics of the musculoskeletal system.* American Academy of Orthopaedic Surgeons, Rosemont, IL, 2000.

[2] Van C. Mow and Rik Huiskes, editors. *Basic orthopaedic biomechanics and mechano-biology.* Lippincott Williams and Wilkins, Philadelphia, 2005.

[3] A. M. Ahmed and D. L. Burke. In-vitro measurement of static pressure distribution in synovial joints–part i: Tibial surface of the knee. *Journal of Biomechanical Engineering*, 105(3):216–225, August 1983.

[4] W. A. Hodge, R. S. Fijan, K. L. Carlson, R. G. Burgess, W. H. Harris, and R. W. Mann. Contact pressures in the human hip joint measured in vivo. *Proceedings of the National Academy of Sciences of the United States of America*, 83(9):2879–2883, May 1986.

[5] N. Y. Afoke, P. D. Byers, and W. C. Hutton. Contact pressures in the human hip joint. *The Journal of bone and joint surgery.British volume*, 69(4):536–541, August 1987.

[6] V. C. Mow and X. E. Guo. Mechano-electrochemical properties of articular cartilage: their inhomogeneities and anisotropies. *Annual Review of Biomedical Engineering*, 4:175–209, 2002.

[7] Evelyne M. Hasler, Walter Herzog, John Z. Wu, Werner Muller, and Urs Wyss. Articular cartilage biomechanics: Theoretical models, material properties, and biosynthetic response. *Critical Reviews in Biomedical Engineering*, 27(6):415 – 488, 1999.

[8] C. G. Armstrong, W. M. Lai, and V. C. Mow. An analysis of the unconfined compression of articular cartilage. *Journal of Biomechanical Engineering*, 106(2):165–173, May 1984.

[9] R. M. Schinagl, D. Gurskis, A. C. Chen, and R. L. Sah. Depth-dependent confined compression modulus of full-thickness bovine articular cartilage. *Journal of orthopaedic research : official publication of the Orthopaedic Research Society*, 15(4):499–506, July 1997.

[10] C. Y. Huang, A. Stankiewicz, G. A. Ateshian, and V. C. Mow. Anisotropy, inhomogeneity, and tension-compression nonlinearity of human glenohumeral cartilage in finite deformation. *Journal of Biomechanics*, 38(4):799–809, April 2005.

[11] Predrag M. Bursac, Toby W. Obitz, Solomon R. Eisenberg, and Dimitrije Stamenovic. Confined and unconfined stress relaxation of cartilage: appropriateness of a transversely isotropic analysis. *Journal of Biomechanics*, 32(10):1125–1130, 1999.

[12] J. S. Jurvelin, M. D. Buschmann, and E. B. Hunziker. Mechanical anisotropy of the human knee articular cartilage in compression. *Proceedings of the Institution of Mechanical Engineers.Part H, Journal of engineering in medicine*, 217(3):215–219, 2003.

[13] P. Kiviranta, J. Rieppo, R. K. Korhonen, P. Julkunen, J. Toyras, and J. S. Jurvelin. Collagen network primarily controls poisson's ratio of bovine articular cartilage in compression. *Journal of orthopaedic research : official publication of the Orthopaedic Research Society*, 24(4):690–699, April 2006.

[14] D. L. Bader, G. E. Kempson, A. J. Barrett, and W. Webb. The effects of leucocyte elastase on the mechanical properties of adult human articular cartilage in tension. *Biochimica et biophysica acta*, 677(1):103–108, Sep 18 1981.

[15] N. O. Chahine, C. C. Wang, C. T. Hung, and G. A. Ateshian. Anisotropic strain-dependent material properties of bovine articular cartilage in the transitional range from tension to compression. *Journal of Biomechanics*, 37(8):1251–1261, August 2004.

[16] M. Charlebois, M. D. McKee, and M. D. Buschmann. Nonlinear tensile properties of bovine articular cartilage and their variation with age and depth. *Journal of Biomechanical Engineering*, 126(2):129–137, April 2004.

[17] R. K. Korhonen, M. S. Laasanen, J. Toyras, J. Rieppo, J. Hirvonen, H. J. Helminen, and J. S. Jurvelin. Comparison of the equilibrium response of articular cartilage in unconfined compression, confined compression and indentation. *Journal of Biomechanics*, 35(7):903–909, July 2002.

[18] H. Jin and J. L. Lewis. Determination of poisson's ratio of articular cartilage by indentation using different-sized indenters. *Journal of Biomechanical Engineering*, 126(2):138–145, April 2004.

[19] Narendra K Simha, Hui Jin, Melanie L Hall, Sidharth Chiravarambath, and Jack L Lewis. Effect of indenter size on elastic modulus of cartilage measured by indentation. *Journal of Biomechanical Engineering*, 129(5):767–775, 2007.

[20] V. C. Mow, M. C. Gibbs, W. M. Lai, W. B. Zhu, and K. A. Athanasiou. Biphasic indentation of articular cartilage–ii. a numerical algorithm and an experimental study. *Journal of Biomechanics*, 22(8-9):853–861, 1989.

[21] K.A. Athanasiou, M.P. Rosenwasser, J.A. Buckwalter, T.I. Malinin, and V.C. Mow. Interspecies comparisons of in situ intrinsic mechanical properties of distal femoral cartilage. *Journal of Orthopaedic Research*, 9:330–340, 1991.

[22] N. Mukherjee and J.S. Wayne. Load sharing between solid and fluid phases in articular cartilage: I: Experimental determination of in situ mechanical conditions in a porcine knee. *Transactions of the ASME. Journal of Biomechanical Engineering*, 120(5):614 – 19, Oct 1998.

[23] Rami K Korhonen, Simo Saarakkala, Juha Töyräs, Mikko S Laasanen, Ilkka Kiviranta, and Jukka S Jurvelin. Experimental and numerical validation for the novel configuration of an arthroscopic indentation instrument. *Physics in Medicine and Biology*, 48(11):1565–1576, 2003.

[24] V. C. Mow, S. C. Kuei, W. M. Lai, and C. G. Armstrong. Biphasic creep and stress relaxation of articular cartilage in compression: Theory and experiments. *Journal of Biomechanical Engineering*, 102(1):73–84, February 1980.

[25] Spilker R.L, Jun-Kyo Suh, and Mow V.C. A finite element analysis of the indentation stress-relaxation response of linear biphasic articular cartilage. *Transactions of the ASME.Journal of Biomechanical Engineering*, 114(2):191–201, 1992.

[26] Jun-Kyo Suh and Shi Bai. Finite element formulation of biphasic poroviscoelastic model for articular cartilage. *Transactions of the ASME.Journal of Biomechanical Engineering*, 120(2):195–201, 1998.

[27] M. R. DiSilvestro, Q. Zhu, M. Wong, J. S. Jurvelin, and J. K. Suh. Biphasic poroviscoelastic simulation of the unconfined compression of articular cartilage: I–simultaneous prediction of reaction force and lateral displacement. *Journal of Biomechanical Engineering*, 123(2):191–197, April 2001.

[28] M. R. DiSilvestro, Q. Zhu, and J. K. Suh. Biphasic poroviscoelastic simulation of the unconfined compression of articular cartilage: Ii–effect of variable strain rates. *Journal of Biomechanical Engineering*, 123(2):198–200, April 2001.

[29] M. R. DiSilvestro and J. K. Suh. A cross-validation of the biphasic poroviscoelastic model of articular cartilage in unconfined compression, indentation, and confined compression. *Journal of Biomechanics*, 34(4):519–525, April 2001.

[30] W. Wilson, B. van Rietbergen, C. C. van Donkelaar, and R. Huiskes. Pathways of load-induced cartilage damage causing cartilage degeneration in the knee after meniscectomy. *Journal of Biomechanics*, 36(6):845–851, Jun 2003.

[31] F. Boschetti, G. Pennati, F. Gervaso, G. M. Peretti, and G. Dubini. Biomechanical properties of human articular cartilage under compressive loads. *Biorheology*, 41(3-4):159–166, 2004.

[32] W. Wilson, C. C. van Donkelaar, R. van Rietbergen, and R. Huiskes. The role of computational models in the search for the mechanical behavior and damage mechanisms of articular cartilage. *Medical engineering and physics*, 27(10):810–826, December 2005.

[33] Li Cao, Youn I, Guilak F, and Setton L.A. Compressive properties of mouse articular cartilage determined in a novel micro-indentation test method and biphasic finite element model. *Transactions of the ASME.Journal of Biomechanical Engineering*, 128(5):766–71, 2006.

[34] J.Z Wu, W Herzog, and M Epstein. Evaluation of the finite element software abaqus for biomechanical modelling of biphasic tissues. *Journal of Biomechanics*, 31(2):165 – 169, 1997.

[35] H.J. Mankin, V.C. Mow, J.A. Buckwalter, J.P. Iannotti, and A. Ratcliffe. *Orthopaedic Basic Science*. American Academy of Orthopaedic Surgeons, second edition, 2000. edited by J.A. Buckwalter, T.A. Einhorn and S.R. Simon, p443-470.

[36] Osteoarthritis Research Society. Osteoarthritis and cartilage. 1(1), January 1993. OARS, Official journal of: the Osteoarthritis Research Society.

[37] Roland W. Moskowitz, editor. *Osteoarthritis : diagnosis and medical/surgical management*. W.B. Saunders, Philadelphia, 2001.

[38] J. Dudhia. Aggrecan, aging and assembly in articular cartilage. *Cellular and Molecular Life Sciences*, 62:2241–2256, 2005. 10.1007/s00018-005-5217-x.

[39] M. A. R. Freeman, editor. *Adult articular cartilage*. Pitman Medical, Tunbridge Wells, Eng., 1979.

[40] M. Wong, P. Wuethrich, P. Eggli, and E. Hunziker. Zone-specific cell biosynthetic activity in mature bovine articular cartilage: a new method using confocal microscopic stereology and quantitative autoradiography. *Journal of orthopaedic research : official publication of the Orthopaedic Research Society*, 14(3):424–432, May 1996.

[41] M. Wong, P. Wuethrich, M. D. Buschmann, P. Eggli, and E. Hunziker. Chondrocyte biosynthesis correlates with local tissue strain in statically compressed adult articular cartilage. *Journal of orthopaedic research : official publication of the Orthopaedic Research Society*, 15(2):189–196, March 1997.

[42] E. B. Hunziker, M. Michel, and D. Studer. Ultrastructure of adult human articular cartilage matrix after cryotechnical processing. *Microscopy research and technique*, 37(4):271–284, May 15 1997.

[43] P. G. Bullough and A. Jagannath. The morphology of the calcification front in articular cartilage. its significance in joint function. *The Journal of bone and joint surgery.British volume*, 65(1):72–78, January 1983.

[44] P. L. Mente and J. L. Lewis. Elastic modulus of calcified cartilage is an order of magnitude less than that of subchondral bone. *Journal of orthopaedic research : official publication of the Orthopaedic Research Society*, 12(5):637–647, September 1994.

[45] J. P. Urban, S. Holm, A. Maroudas, and A. Nachemson. Nutrition of the intervertebral disc: effect of fluid flow on solute transport. *Clinical orthopaedics and related research*, (170)(170):296–302, October 1982.

[46] J. P. Urban, S. Smith, and J. C. Fairbank. Nutrition of the intervertebral disc. *Spine*, 29(23):2700–2709, Dec 1 2004.

[47] E. Wachtel, A. Maroudas, and R. Schneiderman. Age-related changes in collagen packing of human articular cartilage. *Biochimica et biophysica acta*, 1243(2):239–243, Feb 23 1995.

[48] M. A. Cremer, E. F. Rosloniec, and A. H. Kang. The cartilage collagens: a review of their structure, organization, and role in the pathogenesis of experimental arthritis in animals and in human rheumatic disease. *Journal of Molecular Medicine (Berlin, Germany)*, 76(3-4):275–288, March 1998.

[49] E. M. Hasler, W. Herzog, J. Z. Wu, W. Muller, and U. Wyss. Articular cartilage biomechanics: theoretical models, material properties, and biosynthetic response. *Critical Reviews in Biomedical Engineering*, 27(6):415–488, 1999.

[50] J. M. Clark. Variation of collagen fiber alignment in a joint surface: a scanning electron microscope study of the tibial plateau in dog, rabbit, and man. *Journal of orthopaedic research : official publication of the Orthopaedic Research Society*, 9(2):246–257, March 1991.

[51] S. L. Woo, W. H. Akeson, and G. F. Jemmott. Measurements of nonhomogeneous, directional mechanical properties of articular cartilage in tension. *Journal of Biomechanics*, 9(12):785–791, 1976.

[52] D. R. Eyre, S. Apon, J. J. Wu, L. H. Ericsson, and K. A. Walsh. Collagen type ix: evidence for covalent linkages to type ii collagen in cartilage. *FEBS letters*, 220(2):337–341, Aug 17 1987.

[53] Eyre. The collagens of articular cartilage. *Seminars in Arthritis and Rheumatism*, 21(3, Supplement 2):2 – 11, 1991.

[54] Bastian Budde, Katrin Blumbach, Joni Ylstalo, Frank Zaucke, Harald W. A. Ehlen, Raimund Wagener, Leena Ala-Kokko, Mats Paulsson, Peter Bruckner, and Susanne Grssel. Altered integration of matrilin-3 into cartilage extracellular matrix in the absence of collagen ix. *Molecular and Cellular Biology*, 25(23):10465–10478, December 1, 2005.

[55] David Eyre. Articular cartilage and changes in arthritis: Collagen of articular cartilage. *Arthritis Res*, 4(1):30–35, 2002.

[56] Philippa Parsons, Sophie J. Gilbert, Anne Vaughan-Thomas, David A. Sorrell, Rebecca Notman, Mark Bishop, Anthony J. Hayes, Deborah J. Mason, and Victor C. Duance. Type ix collagen interacts with fibronectin providing an important molecular bridge in articular cartilage. *Journal of Biological Chemistry*, 286(40):34986–34997, 2011.

[57] S. Akizuki, V. C. Mow, F. Muller, J. C. Pita, D. S. Howell, and D. H. Manicourt. Tensile properties of human knee joint cartilage: I. influence of ionic conditions, weight bearing, and fibrillation on the tensile modulus. *Journal of orthopaedic research : official publication of the Orthopaedic Research Society*, 4(4):379–392, 1986.

[58] W. Zhu, V. C. Mow, T. J. Koob, and D. R. Eyre. Viscoelastic shear properties of articular cartilage and the effects of glycosidase treatments. *Journal of orthopaedic research : official publication of the Orthopaedic Research Society*, 11(6):771–781, November 1993.

[59] R. C. Haut and R. W. Little. A constitutive equation for collagen fibers. *Journal of Biomechanics*, 5(5):423–430, September 1972.

[60] R. Sanjeevi, N. Somanathan, and D. Ramaswamy. A viscoelastic model for collagen fibres. *Journal of Biomechanics*, 15(3):181–183, 1982.

[61] W. C. Hayes and A. J. Bodine. Flow-independent viscoelastic properties of articular cartilage matrix. *Journal of Biomechanics*, 11(8-9):407–419, 1978.

[62] A. A. Spirt, A. F. Mak, and R. P. Wassell. Nonlinear viscoelastic properties of articular cartilage in shear. *Journal of orthopaedic research : official publication of the Orthopaedic Research Society*, 7(1):43–49, 1989.

[63] W. M. Lai, Van C. Mow, and V. Roth. Effects of nonlinear strain-dependent permeability and rate of compression on the stress behavior of articular cartilage. *Journal of Biomechanical Engineering, Transactions of the ASME*, 103(2):61–66, 1981.

[64] M. S. Laasanen, J. Toyras, R. K. Korhonen, J. Rieppo, S. Saarakkala, M. T. Nieminen, J. Hirvonen, and J. S. Jurvelin. Biomechanical properties of knee articular cartilage. *Biorheology*, 40(1-3):133–140, 2003.

[65] A. F. Mak, W. M. Lai, and V. C. Mow. Biphasic indentation of articular cartilage–i. theoretical analysis. *Journal of Biomechanics*, 20(7):703–714, 1987.

[66] G. A. Ateshian, W. H. Warden, J. J. Kim, R. P. Grelsamer, and V. C. Mow. Finite deformation biphasic material properties of bovine articular cartilage from confined compression experiments. *Journal of Biomechanics*, 30(11):1157–64, 11 1997.

[67] L. A. Setton, W. Zhu, and V. C. Mow. The biphasic poroviscoelastic behavior of articular cartilage: role of the surface zone in governing the compressive behavior. *Journal of Biomechanics*, 26(4-5):581–592, Apr-May 1993.

[68] B. Cohen, W. M. Lai, and V. C. Mow. Transversely isotropic biphasic model for unconfined compression of growth plate and chondroepiphysis. *Journal of Biomechanical Engineering, Transactions of the ASME*, 120(4):491–496, 1998.

[69] J. J. Garcia, N. J. Altiero, and R. C. Haut. Approach for the stress analysis of transversely isotropic biphasic cartilage under impact load. *Journal of Biomechanical Engineering, Transactions of the ASME*, 120(5):608–613, 1998.

[70] Peter S. Donzelli, Robert L. Spilker, Gerard A. Ateshian, and Van C. Mow. Contact analysis of biphasic transversely isotropic cartilage layers and correlations with tissue failure. *Journal of Biomechanics*, 32(10):1037–1047, 1999.

[71] J. K Suh and M. R. DiSilvestro. Biphasic poroviscoelastic behavior of hydrated biological soft tissue. *Journal of Applied Mechanics, Transactions ASME*, 66(2):528–535, 1999.

[72] M. A. Soltz and G. A. Ateshian. A conewise linear elasticity mixture model for the analysis of tension-compression nonlinearity in articular cartilage. *Journal of Biomechanical Engineering*, 122(6):576–586, December 2000.

[73] Chun-Yuh Huang, Mow V.C, and Ateshian G.A. The role of flow-independent viscoelasticity in the biphasic tensile and compressive responses of articular cartilage. *Transactions of the ASME.Journal of Biomechanical Engineering*, 123(5):410–17, 2001.

[74] J. J. Garcia and D. H. Cortes. A nonlinear biphasic viscohyperelastic model for articular cartilage. *Journal of Biomechanics*, 39(16):2991–2998, 2006.

[75] W. M. Lai, J. S. Hou, and V. C. Mow. A triphasic theory for the swelling and deformation behaviors of articular cartilage. *Journal of Biomechanical Engineering*, 113(3):245–258, August 1991.

[76] J. M. Huyghe and J. D. Janssen. Quadriphasic mechanics of swelling incompressible porous media. *International Journal of Engineering Science*, 35(8):793–802, 1997.

[77] W. Wilson, C. C. van Donkelaar, and J. M. Huyghe. A comparison between mechano-electrochemical and biphasic swelling theories for soft hydrated tissues. *Journal of Biomechanical Engineering*, 127(1):158–165, February 2005.

[78] S. R. Eisenberg and A. J. Grodzinsky. The kinetics of chemically induced nonequilibrium swelling of articular cartilage and corneal stroma. *Journal of Biomechanical Engineering*, 109(1):79–89, February 1987.

[79] A. Curnier, Qi-Chang He, and P. Zysset. Conewise linear elastic materials. *Journal of Elasticity*, 37(1):1–38, 1995.

[80] J. Soulhat, M. D. Buschmann, and A. Shirazi-Adl. A fibril-network-reinforced biphasic model of cartilage in unconfined compression. *Journal of Biomechanical Engineering*, 121(3):340–347, June 1999.

[81] L. P. Li, J. Soulhat, M. D. Buschmann, and A. Shirazi-Adl. Nonlinear analysis of cartilage in unconfined ramp compression using a fibril reinforced poroelastic model. *Clinical Biomechanics*, 14(9):673–682, 1999/11.

[82] L. P. Li, M. D. Buschmann, and A. Shirazi-Adl. Strain-rate dependent stiffness of articular cartilage in unconfined compression. *Journal of Biomechanical Engineering*, 125(2):161–168, April 2003.

[83] L. P. Li and W. Herzog. Strain-rate dependence of cartilage stiffness in unconfined compression: the role of fibril reinforcement versus tissue volume change in fluid pressurization. *Journal of Biomechanics*, 37(3):375–382, March 2004.

[84] T. Farquhar, P. R. Dawson, and P. A. Torzilli. A microstructural model for the anisotropic drained stiffness of articular cartilage. *Journal of Biomechanical Engineering*, 112(4):414–425, November 1990.

[85] H. K. Ault and A. H. Hoffman. A composite micromechanical model for connective tissues: Part i–theory. *Journal of Biomechanical Engineering*, 114(1):137–141, February 1992.

[86] M. H. Schwartz, P. H. Leo, and J. L. Lewis. A microstructural model for the elastic response of articular cartilage. *Journal of Biomechanics*, 27(7):865–873, July 1994.

[87] W. Wilson, C. C. van Donkelaar, B. van Rietbergen, K. Ito, and R. Huiskes. Stresses in the local collagen network of articular cartilage: a poroviscoelastic fibril-reinforced finite element study. *Journal of Biomechanics*, 37(3):357–366, March 2004.

[88] Salvatore Federico, Alfio Grillo, Guido La Rosa, Gaetano Giaquinta, and Walter Herzog. A transversely isotropic, transversely homogeneous microstructural-statistical model of articular cartilage. *Journal of Biomechanics*, 38(10):2008–2018, 2005/10.

[89] Jos Jaime Garca and Daniel Humberto Corts. A biphasic viscohyperelastic fibril-reinforced model for articular cartilage: Formulation and comparison with experimental data. *Journal of Biomechanics*, 40(8):1737–1744, 2007.

[90] W. Wilson, C. C. van Donkelaar, B. van Rietbergen, and R. Huiskes. A fibril-reinforced poroviscoelastic swelling model for articular cartilage. *Journal of Biomechanics*, 38(6):1195–1204, June 2005.

[91] W. Wilson, J. M. Huyghe, and C. C. van Donkelaar. A composition-based cartilage model for the assessment of compositional changes during cartilage damage and adaptation. *Osteoarthritis and cartilage / OARS, Osteoarthritis Research Society*, 14(6):554–560, June 2006.

[92] Salvatore Federico, Alfio Grillo, and Walter Herzog. A transversely isotropic composite with a statistical distribution of spheroidal inclusions: A geometrical approach to overall properties. *Journal of the Mechanics and Physics of Solids*, 52(10):2309–2327, 2004.

[93] A. F. Mak. The apparent viscoelastic behavior of articular cartilage–the contributions from the intrinsic matrix viscoelasticity and interstitial fluid flows. *Journal of Biomechanical Engineering*, 108(2):123–130, May 1986.

[94] M. R. DiSilvestro and J. K. Suh. Biphasic poroviscoelastic characteristics of proteoglycan-depleted articular cartilage: simulation of degeneration. *Annals of Biomedical Engineering*, 30(6):792–800, June 2002.

[95] M. J. Kaab, K. Ito, J. M. Clark, and H. P. Notzli. Deformation of articular cartilage collagen structure under static and cyclic loading. *Journal of orthopaedic research : official publication of the Orthopaedic Research Society*, 16(6):743–751, November 1998.

[96] M. J. Kaab, K. Ito, B. Rahn, J. M. Clark, and H. P. Notzli. Effect of mechanical load on articular cartilage collagen structure: a scanning electron-microscopic study. *Cells, tissues, organs*, 167(2-3):106–120, 2000.

[97] Sidharth Chiravarambath, Narendra K. Simha, Ravi Namani, and Jack L. Lewis. Poroviscoelastic cartilage properties in the mouse from indentation. *Journal of Biomechanical Engineering*, 131(1):011004, 2009.

[98] L. Xu, C. M. Flahiff, B. A. Waldman, D. Wu, B. R. Olsen, L. A. Setton, and Y. Li. Osteoarthritis-like changes and decreased mechanical function of articular cartilage in the joints of mice with the chondrodysplasia gene (cho). *Arthritis and Rheumatism*, 48(9):2509–2518, Sep 2003.

[99] E. I. Palmer and J. C. Lotz. The compressive creep properties of normal and degenerated murine intervertebral discs. *Journal of orthopaedic research : official publication of the Orthopaedic Research Society*, 22(1):164–169, Jan 2004.

[100] J. Zwerina, K. Redlich, K. Polzer, L. Joosten, G. Kroenke, J. Distler, A. Hess, N. Pundt, T. Pap, O. Hoffmann, J. Gasser, C. Scheinecker, J. S. Smolen, W. van den Berg, and G. Schett. Tnf-induced structural joint damage is mediated by il-1. *Proceedings of the National Academy of Sciences of the United States of America*, Jul 3 2007.

[101] Ravi Namani. *Inverse finite element methods for extracting elastic-poroviscoelastic properties of cartilage and other soft tissues from indentation.* PhD thesis, 2006. by Ravi Namani.; xiii, 147 leaves : ill. ; 28 cm; Thesis (Ph. D.)–University of Miami, 2006.; Includes bibliographical references (leaves 143-147); 690: Mechanical Engineering Dissertations.

[102] J. A. Nelder and R. Mead. Simplex method for function minimization. *Computer journal*, 7(4):308–313, 1965.

[103] W. C. Hayes, L. M. Keer, G. Herrmann, and L. F. Mockros. A mathematical analysis for indentation tests of articular cartilage. *J Biomech*, 5(5):541–51, 1972.

[104] R. M. Christensen. *Mechanics of composite materials.* Wiley, New York, 1979.

[105] Suresh G. Advani and Charles L. Tucker III. The use of tensors to describe and predict fiber orientation in short fiber composites. *Journal of Rheology*, 31(8):751–784, 1987.

[106] A. L. Clark, L. D. Barclay, J. R. Matyas, and W. Herzog. In situ chondrocyte deformation with physiological compression of the feline patellofemoral joint. *Journal of Biomechanics*, 36(4):553–568, 2003/4.

[107] S. Federico, W. Herzog, J. Z. Wu, and G. La Rosa. A method to estimate the elastic properties of the extracellular matrix of articular cartilage. *Journal of Biomechanics*, 37(3):401–404, Mar 2004.

[108] L. J. Walpole. Elastic behavior of composite materials: Theoretical foundations. *Advances in Applied Mechanics*, 21:169–242, 1981. Compilation and indexing terms, Copyright 2007 Elsevier Inc. All rights reserved.

[109] Ted Belytschko, W. K. Liu, and B. Moran. *Nonlinear finite elements for continua and structures*. John Wiley, Chichester ; New York, 2000.

[110] M. H. Holmes and V. C. Mow. The nonlinear characteristics of soft gels and hydrated connective tissues in ultrafiltration. *Journal of Biomechanics*, 23(11):1145–1156, 1990.

[111] Georges Limbert and John Middleton. A transversely isotropic viscohyperelastic material application to the modeling of biological soft connective tissues. *International Journal of Solids and Structures*, 41(15):4237–4260, 2004.

[112] R.K. Korhonen, M.S. Laasanen, J. Toyras, Lappalainen R., H.J. Helminen, and J.S. Jurvelin. Fibril reinforced poroelastic model predicts specifically mechanical behavior of normal, proteoglycan depleted and collagen degraded articular cartilage. *Journal of Biomechanics*, 36(9):1373–1379, 2003.

[113] W. Wilson, J. M. Huyghe, and C. C. van Donkelaar. Depth-dependent compressive equilibrium properties of articular cartilage explained by its composition. *Biomechanics and modeling in mechanobiology*, 6(1-2):43–53, January 2007.

[114] S. K Han, S. Federico, A. Grillo, G. Giaquinta, and W. Herzog. The mechanical behaviour of chondrocytes predicted with a micro-structural model of articular cartilage. *Biomechanics and Modeling in Mechanobiology*, 6(3):139–150, 2007.

[115] L. Bozec, G. van der Heijden, and M. Horton. Collagen fibrils: nanoscale ropes. *Biophysical Journal*, 92(1):70 – 5, 2007. collagen fibril structure;nanoscale ropes;atomic force microscopy;tendon collagen fibrils;elastic rod theory;tissue engineering;pathogenesis;diseases;bone;.

[116] Zhilei L. Shen, Mohammad Reza Dodge, Harold Kahn, Roberto Ballarini, and Steven J. Eppell. Stress-strain experiments on individual collagen fibrils. *Biophysical Journal*, 95(8):3956 – 3963, 2008.

[117] George D. Pins, Eric K. Huang, David L. Christiansen, and Frederick H. Silver. Effects of static axial strain on the tensile properties and failure mechanisms of self-assembled collagen fibers. *Journal of Applied Polymer Science*, 63(11):1429–1440, 1997.

[118] Frederick H. Silver, Gino Bradica, and Alfred Tria. Elastic energy storage in human articular cartilage: estimation of the elastic modulus for type ii collagen and changes associated with osteoarthritis. *Matrix Biology*, 21(2):129 – 137, 2002.

[119] Y.C. Fung. *Biomechanics: Mechanical Properties of Living Tissues.* Springer, 1993.

[120] Ian C. Clarke. Articular cartilage: A review and scanning electron microscope study: 1. the interterritorial fibrillar architecture. *J Bone Joint Surg Br*, 53-B(4):732–750, 1971.

[121] Jean Paul Revel and Elizabeth D. Hay. An autoradiographic and electron microscopic study of collagen synthesis in differentiating cartilage. *Cell and Tissue Research*, 61:110–144, 1963. 10.1007/BF00341524.

[122] D. V. Davies, C. H. Barnett, W. Cochrane, and A. J. Palfrey. Electron microscopy of articular cartilage in the young adult rabbit. *Annals of the Rheumatic Diseases*, 21(1):11 – 22, 1962.

[123] Helen Muir, Peter Bullough, and Alice Maroudas. The distribution of collagen in human articular cartilage with some of its physiological implications. *J Bone Joint Surg Br*, 52-B(3):554–563, 1970.

[124] C. H. Barnett, W. Cochrane, and A. J. Palfrey. Age changes in articular cartilage of rabbits. *Annals of the Rheumatic Diseases*, 22(6):389 – 400, 1961.

[125] J. G. McCall. Ultrastructure of human articular cartilage. *Journal of Anatomy*, 104(3):586 – 587, 1969.

[126] F.H. Silver, Y.P. Kato, M. Ohno, and A.J. Wasserman. Analysis of mammalian connective tissue: relationship between hierarchical structures and mechanical properties. *Journal of Long-Term Effects of Medical Implants*, 2:165–198, 1992. 10.1007/BF00341524.

[127] C.W. and McCutchen. The frictional properties of animal joints. *Wear*, 5(1):1 – 17, 1962.

[128] J.M. Zarek and J.A. Edwards. A note on the stress-structure relationship in articular cartilage. *Medical Electronics and Biological Engineering*, 3(4):449 – 450, 1965.

[129] L. Sokolof. Elasticity of aging cartilage. *Fed. Proc.*, 25(3):1089 – 95, 1966.

[130] Alice and Maroudas. Physicochemical properties of cartilage in the light of ion exchange theory. *Biophysical Journal*, 8(5):575 – 595, 1968.

[131] J. M. Mansour and V. C. Mow. The permeability of articular cartilage under compressive strain and at high pressures. *The Journal of Bone and Joint Surgery. American Volume*, 58(4):509–16, 1976.

[132] W. M. Lai and V. C. Mow. Drag-induced compression of articular cartilage during a permeation experiment. *Biorheology*, 17(1-2):111–23, 1980.

[133] Xuhui Liu, Ming-Long Yeh, Jack L. Lewis, and Zong-Ping Luo. Direct measurement of the rupture force of single pair of decorin interactions. *Biochemical and Biophysical Research Communications*, 338(3):1342 – 1345, 2005.

[134] A.G. Ogston. *Chemistry and Molecular Biology of the Intercellular Matrix*, volume 3 of *The Biological Functions of the Glycosaminoglycans*. Academic Press, London, 1970.

[135] Peter J. Basser, Rosa Schneiderman, Ruud A. Bank, Ellen Wachtel, and Alice Maroudas. Mechanical properties of the collagen network in human articular cartilage as measured by osmotic stress technique. *Archives of Biochemistry and Biophysics*, 351(2):207 – 219, 1998.

[136] S. Loehnert. *Computational Homogenization of Microheterogeneous Materials at Finite Strains Including Damage*. PhD thesis, 2004.

[137] M. Oda and A.A. Iwashita. *Mechanics of Granular Materials*. Brookfield, Rotterdam, 1999.

[138] O. van der Sluis, P.J.G. Schreurs, W.A.M. Brekelmans, and H.E.H. Meijer. Overall behaviour of heterogeneous elastoviscoplastic materials: effect of microstructural modelling. *Mechanics of Materials*, 32(8):449 – 462, 2000.

[139] J. Aboudi. *Mechanics of Composite Materials, A Unified Micromechanical Approach*. Elsevier Science Publishers, Amsterdam, 1991.

[140] A. Redaelli, S. Vesentini, M. Soncini, P. Vena, S. Mantero, and F.M. Montevecchi. Possible role of decorin glycosaminoglycans in fibril to fibril force transfer in relative mature tendonsa computational study from molecular to microstructural level. *Journal of Biomechanics*, 36(10):1555–1569, 2003.

[141] Triantafyllos Stylianopoulos and Victor H. Barocas. Volume-averaging theory for the study of the mechanics of collagen networks. *Computer Methods in Applied Mechanics and Engineering*, 196(3132):2981 – 2990, 2007.